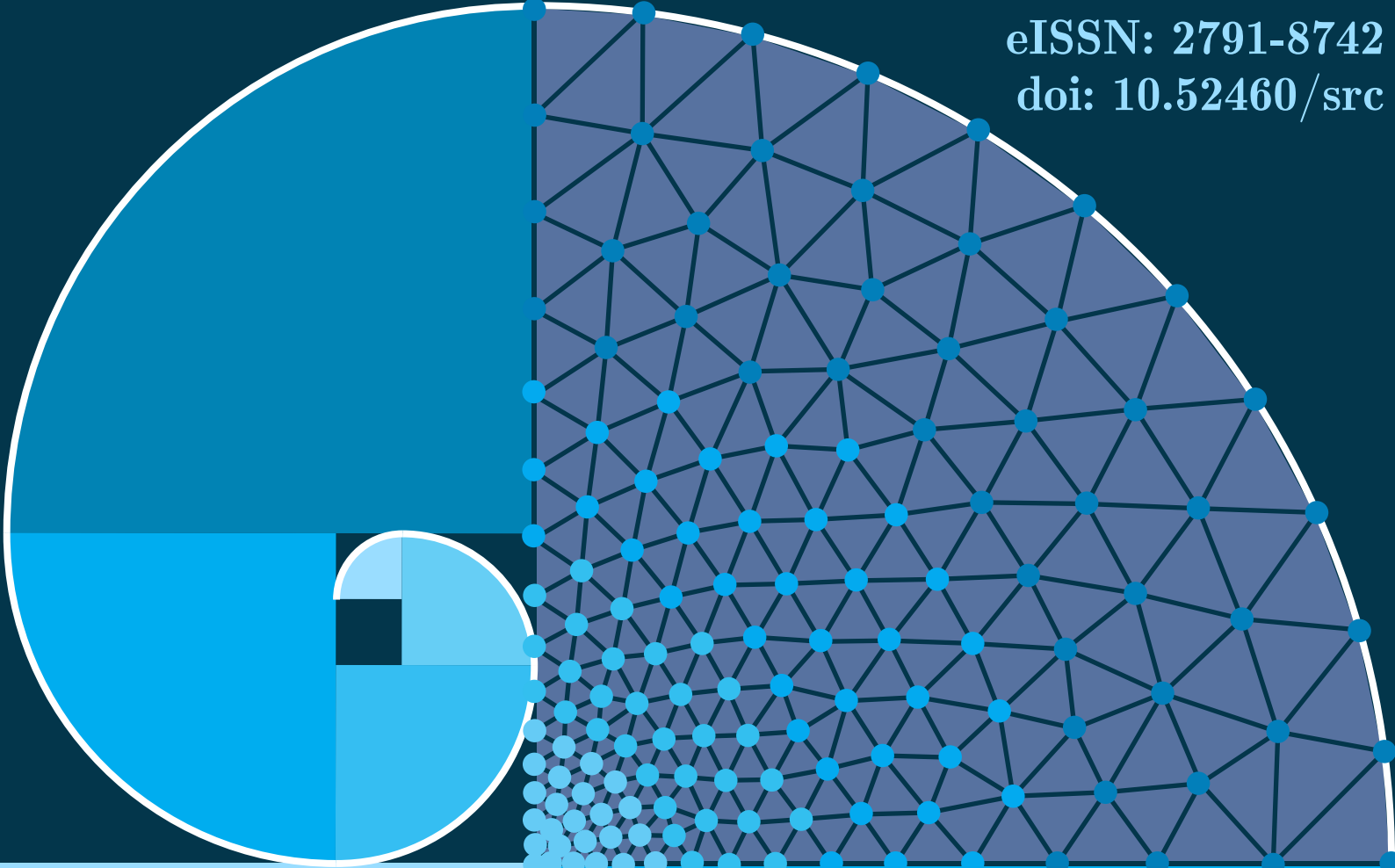
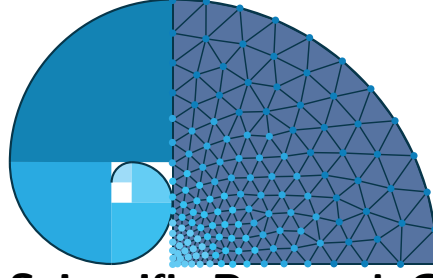


eISSN: 2791-8742
doi: 10.52460/src



**Scientific
Research
Communications**

**Volume 4
Issue 2
July 2024**



Scientific Research Communications

Volume 4, Issue 2, 2024

Editorial

Editor-in-Chief

Mehmet ÇEVİK

Associate Editors

Ahmet AYKAÇ

Aydın AKAN

Ayşe KALAYCI ÖNAÇ

Faruk ÖZGER

Fatih Erdoğan SEVİLGEN

Gökçen BOMBAR

Sedat YALÇINKAYA

Sercan ACARER

Umut CEYHAN

Office

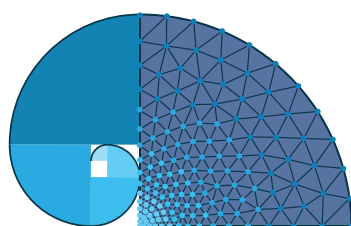
Furkan EMREM

Zehra BÜYÜKER

Publisher

Prof. Dr. Mehmet ÇEVİK

İzmir International Guest Students Association



Scientific Research Communications

Volume 4, Issue 2, 2024

Contents

Research Articles

Agricultural Supply Chains: Challenges and Opportunities for Agribusiness in Afgoye, Lower Shabelle, Somalia, pp.61-72

I. I. Ali and A. H. Ahmed

Utilization of Short Span Web-Tapered Beams Using Flexible Nodal Bracing, pp.73-85

F. Kömürçü and O. Toğay

Heat and Mass Transfer Model of Horizontal Tubular Absorbers for LiBr/H₂O Absorption Refrigeration, pp.86-110

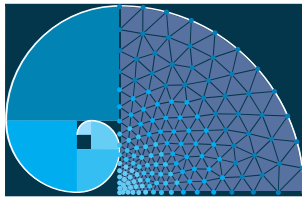
N. Kayansayan and S. Acarer

Finite Element Analysis of Delamination Initiation in Wind Turbine Blade Spar Caps: Role of Compression, Strain Energy, and Principal Stresses, pp.111-131

F. Özmen and R. Karakuzu

Isolation and Characterization of a (Surfactin-Like Molecule) Produced by Bacillus subtilis: Antagonistic Impact on Root-Knot Nematodes, pp.132-149

P. Niazi



Agricultural Supply Chains: Challenges and Opportunities for Agribusiness in Afgoye, Lower Shabelle, Somalia

Ibrahim Isse Ali^{1,*}  Ali Hussein Ahmed² 

¹ Department of Plant Protection, Faculty of Agriculture, Selçuk University, Konya, Türkiye

² Department of Agribusiness Management, Faculty of Agriculture, Zamzam University, Mogadishu, Somalia

* Corresponding author: ibraisse252@gmail.com

Received: 13.12.2023

Accepted: 25.07.2024

Abstract

Somalia's largely agrarian economy relies heavily on agriculture. The agricultural sector faces significant challenges in agricultural supply chains, which can hinder its development and growth. Lack of infrastructure, insecurity, and poor linkage to the market are some of those challenges. This study investigates the agricultural supply chains in Afgoye, Lower Shabelle, Somalia, a region with unique challenges and opportunities for agribusiness. It also discusses the importance of technology in improving supply chain efficiency and the role that government and other stakeholders can play in supporting agribusinesses. Additionally, the paper examines the potential impact of improved agricultural supply chains on the Somali economy and provides valuable insights for policymakers, investors, and development practitioners seeking to support and promote agribusiness. The methodology used in this study involved survey questions. The survey questions utilized for this study were distributed through key stakeholders in Somalia's agricultural supply chains, including farmers, wholesalers, retailers, and processors. SPSS (version 20) is used to analyze the data collected from participants. According to the results, 57.5% of the respondents emphasized that investing in the agricultural sector is necessary and may improve the standard of life of the population. The technology can enhance Somalia's agricultural supply chain through access to information as well as market access and e-commerce, as indicated by 47.5% and 35%, respectively. Ultimately, this paper highlights the importance of addressing the challenges facing agricultural supply chains in Somalia and unlocking the opportunities that exist for agribusinesses to contribute to the country's economic development.

Keywords: Supply chain, agribusiness, Somalia, challenges, opportunities

1. Introduction

According to the definition of agribusiness in the Oxford Dictionary, agribusiness is the practice of agriculture conducted strictly on commercial principles, involving an organization engaged in agribusiness, and encompassing a group of industries dealing with agricultural produce and services required for farming. A supply chain consists of participants that produce and deliver products (including goods and services) from its earliest suppliers to its ultimate customers (Sjah and Zainuri, 2020). Agriculture dominates the key to broad-based economic growth, poverty reduction, and food security in Sub-Saharan Africa

(Jayne et al., 2010; Schaffnit-Chatterjee, 2014; Ssozi et al., 2019). This sector is an important contributor to the Somali economy, providing employment opportunities and generating income for many small-scale farmers. Salam Development Center (2020) concluded, in its July 2020 report on Somalia's agriculture and livestock, that agriculture (including livestock) is the backbone of the Somali economy. It contributes over 90% of the country's total exports, constitutes 70% of its GDP, and employs over 80% of its population (Heritage Institute., 2020; SOMINVEST, 2022). However, the sector faces significant challenges when it comes to agricultural supply chains, which reduce its growth and development.

The agricultural supply chain in the country has been weak since the collapse of the military government that dominated agricultural services including infrastructures of production since there (Mohamed et al., 2015). Most parts of Somalia regions have low supply chains. Floods or crises cause this. Additionally, merchants have purchased re-stocks to meet any expected increase in commodity demand. After the collapse of the government, agricultural exports were few because of the collapsed institutions in the agricultural sector, but most of the farm holders produce mainly cereals and fruits for household consumption where the surplus units are transported to the urban markets for cash exchanges (Ali, 2022; Gavin et al., 2019; Hastings et al., 2022). The sector also has been severely impacted by years of conflict, droughts, and poor infrastructure (Kullane et al., 2022; Said and Ibrahim, 2023). Despite these challenges, there have been efforts to revive and modernize the agricultural sector in Somalia through the promotion of agribusiness (FAO and Bank, 2018). This involves integrating agricultural production with value-added processing and marketing to create a more competitive and profitable industry. Overall, the development of agribusiness in Somalia has the potential to create employment opportunities, increase incomes, and contribute to food security. However, significant investment is needed in infrastructure, research and development, and market access to realize this potential. The rangelands in Somalia's north and center receive low rainfall and contain few permanent springs. Thus, one of the primary causes of conflict between agro-pastoralists and nomadic pastoralists has always been water. The conflict for land and water resources between pastoralists and settled farmers has been one of the main causes of the nearly three-decade-long civil war, even in the fertile southern Somali regions blessed with more frequent rains and river water (FAO and Bank, 2018). Ongoing conflicts and instability in Somalia have affected agricultural production and the ability of farmers to access markets. This has also resulted in the displacement of many people, which has negatively impacted agricultural productivity. Low access to finance for the farmers, climate change, limited technical expertise, and poor market access are also the challenges faced by agricultural supply chains in Somalia, which hinder the growth and development of agribusinesses in the country (Ahmed et al., 2023). This paper conducted an in-depth investigation of the challenges and opportunities for agribusiness in Somalia. We examined the challenges by gathering information from survey responses of individuals residing in Afgoye, lower Shabelle, Somalia. This research aims to explore the challenges faced by the agricultural supply chain and how they can be overcome to enhance their operations, contribute to economic growth, improve food security, and uplift rural communities in Somalia.

2. Challenges and Opportunities in Somalia's Agricultural Sector

2.1. Constraints of the agricultural supply chain in Somalia

Since the recurrence of droughts and floods, associated with climate change, has become a regular occurrence in the country, farming and agricultural production have declined (Pape and Wollburg, 2019; Said et al., 2023; Said and Hassan, 2024). Additionally, Somali people have

lacked opportunities and resources related to precious farming and never had before. The labor force and farm equipment are the biggest challenges that farmers face. Hand tools like hoes and old-version tractors are the only equipment that farmers use (Abdi-Soojeede, 2018). Somalia was in a civil war for years. This resulted in the mass destruction of infrastructure, and service areas as well as the availability of some resources to enhance production. Nevertheless, the knowledge and information on up-to-date farming practices are very short as well as there is a misuse of information about inputs, not only among farmers but also among traders and suppliers (FAO et al., 2014). The land tenure system in the country is also another challenging factor that the agricultural sector in the country is suffering. Farmers may not have been able to get these essential inputs since more and more vendors demand upfront cash payment (Ali et al., 2024; Heritage Institute., 2020). Farmers that were struggling financially were unable to obtain. Crop loss or damage during the growing season (locust, fall armyworm, dry spells, disasters other than plant disease): Lower Shabelle, Togdheer, Sanaag, and Bakool had a relatively greater proportion of households reporting this as a challenge than other regions. Dry spells and an early cessation of the Gu rainy season also illustrated crop losses and declined income from agriculture (NET, 2022).

2.2. Opportunities in Agribusiness in Somalia

According to the Sominvest of the Ministry of Planning in the Somali Federal government, Legislation has been established by the agricultural regulatory agency known as SARIS. This legislation promotes agrarian trade in the international market. The institution's tasks are implementing the Somali Agrochemical Policy; the Seeds and Varieties Act; the Plant Protection and Quarantine Law; the National Fertilizer Policy; and the National Pesticide Policy. With the challenges of climate change on agriculture, the Federal government established a greenfield program that focuses on climate change adaptation and effect mitigation (SOMINVEST, 2022). Considering the significance of this sector, the Somali government is implementing transformational farming to modernize traditional farming practices that back holds agricultural production in the country. The ministry is also improving business-enabling environment and climate mitigation regulatory and cropping processing substitutes.

Investment opportunities in agriculture in the country are widely bare. Somalia has large and fertile land that suits for farming throughout the year. Drought recurrence and accumulated obstacles have caused a lack of investment and an absence of interest in foreign and local investment. Since the challenges are going to end, the agribusiness industry is a crude opportunity that everyone can cultivate and take advantage of it. To create a suitable investment environment for agriculture, key factors include research & development of agricultural inputs, inspection & certification of their quality, potential creation of private or public insurance systems, efficient agri-input distribution, local manufacturing of affordable farm equipment, establishment of regional supply chains, and private seed certification techniques. Farmers may be another factor that can ensure foreign and local investment.

3. Problem Statement

The agricultural sector in Somalia faces numerous challenges and opportunities within its supply chains, posing significant obstacles for agribusinesses operating in the country. These challenges stem from a combination of factors, including political instability, limited infrastructure, climate change, and inadequate access to markets and financing. As a result, the agribusiness sector struggles to achieve its full potential, hindering economic growth, food security, and rural development in Somalia. One major challenge in agricultural supply chains

in Somalia is the lack of reliable infrastructure. Insufficient road networks, storage facilities, and transportation systems make it difficult to move agricultural produce from rural areas to markets, leading to high post-harvest losses and increased costs. This not only affects the profitability of agribusinesses but also limits the availability of food in local and regional markets. Political instability and insecurity also pose significant challenges to agricultural supply chains in Somalia. Frequent conflicts and the presence of armed groups disrupt farming activities, making it difficult for agribusinesses to operate safely and consistently. This instability further hampers investments in agriculture, discouraging both domestic and foreign investors from engaging in agribusiness activities.

Climate change is another pressing issue affecting agricultural supply chains in Somalia. Changing weather patterns, including irregular rainfall, droughts, and floods, impact crop production and livestock rearing (Said et al., 2023). Farmers and agribusinesses face challenges in adapting to these changing conditions, resulting in decreased productivity, increased vulnerability, and reduced incomes. Furthermore, limited access to markets and financial services constrains the growth and profitability of agribusinesses in Somalia.

Many farmers and agribusinesses struggle to find reliable buyers and obtain fair prices for their products. Additionally, the lack of access to affordable credit and financial services limits their ability to invest in modern farming techniques, machinery, and inputs, hindering productivity and expansion.

Addressing these challenges presents significant opportunities for agribusinesses in Somalia. By improving infrastructure, such as roads, storage facilities, and transportation systems, the efficiency of agricultural supply chains can be enhanced, reducing post-harvest losses, and improving market access. Promoting stability and security in the country will attract domestic and foreign investments, fostering the growth of agribusinesses and the overall agricultural sector. Additionally, implementing climate-smart agriculture practices and providing farmers with relevant information and resources can help them adapt to climate change and build resilience.

In conclusion, the challenges faced by agricultural supply chains in Somalia, including inadequate infrastructure, political instability, climate change, and limited market access and financing, hinder the growth and development of agribusinesses in the country. However, addressing these challenges presents significant opportunities for agribusinesses to enhance their operations, contribute to economic growth, improve food security, and uplift rural communities in Somalia.

4. Material and Method

4.1. Study Area

Afgoye is a town in the Lower Shabelle region of Somalia, situated about 30 kilometers (18 miles) west of Mogadishu, the capital of Somalia (see Figure 1). It lies at an altitude of 83 meters (272 feet) with a latitude of 2° 13'N and 45° 15'E. The study area's climate is semi-arid which is well known for both the Shebelle River, which flows through the town's center, and its alluvial soil (Muchiri, 2007).

4.2. Research Methodology

The methodology used in this study involved survey questions. The survey questions utilized for this study were distributed and collected through key stakeholders in Somalia's agricultural supply chains, including farmers, wholesalers, retailers, and processors in the

Afgoye district of lower Shabelle Region, Somalia in 2023. The total of questionnaires distributed for the study constituted Demographic Information and 10 other questions in which all participants were asked similarly. These questions provided valuable insights into the challenges and opportunities facing agribusinesses in the country and helped to inform the recommendations provided in the paper.

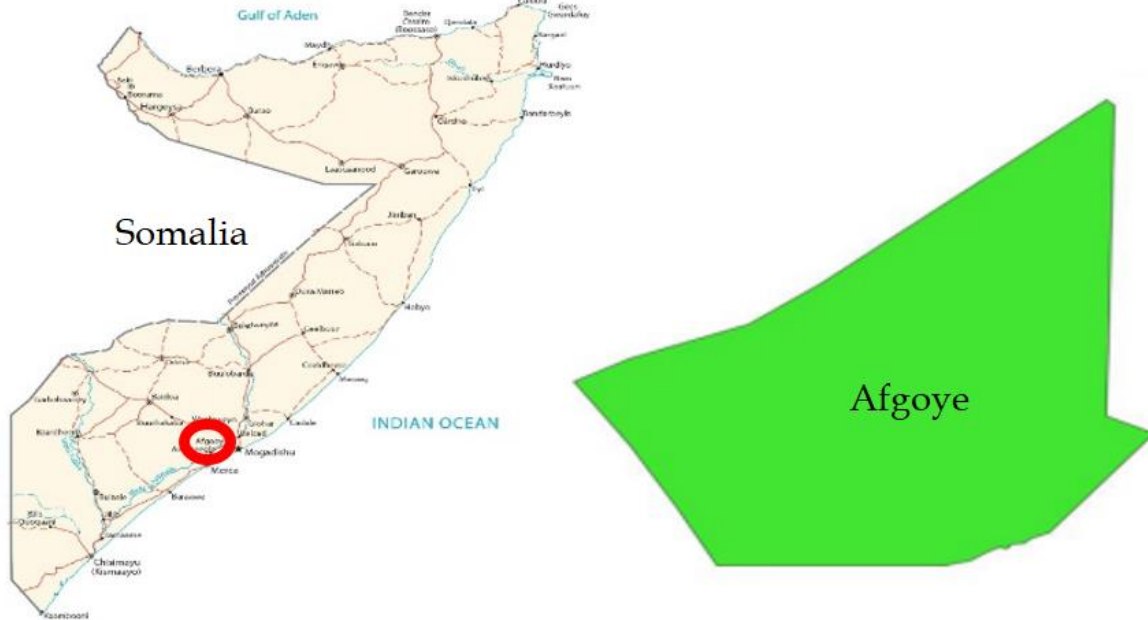


Figure 1. Study area

The target of the research population was 100 people. The sample size of 80 respondents was selected by using Slovene's formula given in Eq. (1).

$$n = \frac{N}{1 + N(e)^2}, \quad (1)$$

where, N is the estimated target population, n is the required sample size, and e is the margin error, also known as the level of significance, which is commonly set at 0.05 or 5%. Given that $N = 100$ for this investigation, the sample size was determined as follows:

$$n = \frac{100}{1 + 100(0.05)^2} = 80.$$

The obtained data from surveys were statistically evaluated using Statistical Package for Social Sciences (SPSS version 20) software to generate descriptive statistics, conduct correlation analysis, and explore patterns or trends.

5. Results and Discussion

Figure 2 outlines the demographic characteristics of the respondents. Within the sample size of 80 respondents, 51 (63.7%) of the respondents were males, while 29 (36.3%) of the respondents were females. Additionally, the study showed that respondents 34 (42.5%) and 19 (23.8%) were non-formal, and in secondary education respectively, while 14 (17.5%) were in graduate education, and 13 (16.3%) were in primary education. About the marital status of the respondents, the study found that most of the respondents, 43 (53.8%), were married. On the other hand, 29 (36.3%) were single and 8 (10.0%) were divorced. This highlights that the percentage of married respondents is high. According to the age distribution of respondents, 23 (28.7%) were aged 31-40, 19 (23.8%) were aged 20-30, 18 (22.5%) were aged 41-50, 16 (20.0%) were aged 51-60, and 4 (5.0%) were above 60 years old.

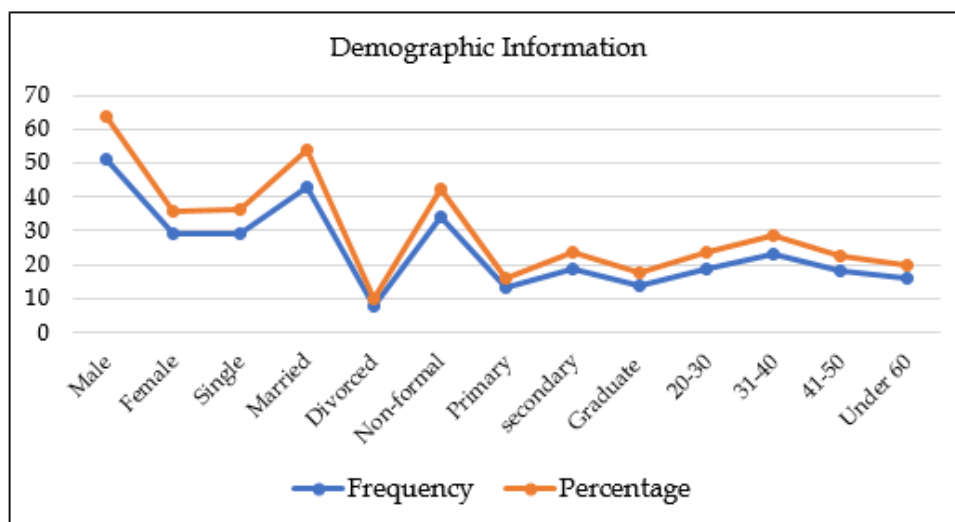


Figure 2. Demographic information of the respondents

In the study, 75% of the respondents were farm owners, while 25% of the respondents were farm employees which indicates that farm owners are a larger number than farm employees. Additionally, years of experience in agribusiness and some related jobs were among the survey questions and 65% of the research participants suggested that they had 1-2 years of experience in agribusiness and related agricultural enterprises, while 17.5% of them had experience in 3-5 years of experience in agribusiness, and the remaining in more than 6 years of agribusiness as shown in Table 1.

Table 1. Work experience of the respondents

Variables	n	%
Do you have a farm or work?		
Yes	60	75.0
No	20	25.0
Total	80	100.0
Experience in agribusiness and some related jobs		
1-2 years	52	65.0
3-5 years	14	17.5
More than 6 years	14	17.5
Total	80	100.0

Table 2 presents the current state of agricultural supply chains in the country has lots of concerns related to lack of infrastructure, and insecurity. 45% of the research participants stated that agricultural supply chains in the country are poor, 35% of the participants had an idea of the moderate state of agricultural supply chains, and 20% of the study respondents answered the very poor state of the agricultural supply chain. Previous studies have declared that the agricultural supply chain faces various challenges, and the agribusiness sector in Somalia is in a very poor state (Ali, 2022; Waris, 2018). Some of the main challenges that agribusinesses face in agricultural supply chains in Somalia are apparent, including poor market linkage, insecurity, lack of infrastructure, and others (Gaal and Afrah, 2017; Gardner and El-Bushra, 2017; Little, 1996; Mifsud, 2007). In this study, 42.5% of the respondents highlighted that the lack of infrastructure is the major challenge facing Somali agribusinesses. Furthermore, 30% identified poor market linkage as a significant hurdle. Lastly, 27.5% concluded that insecurity, one of the most detrimental factors impeding numerous developmental projects in the country, is an obstacle faced by agribusinesses in Somalia.

Table 2. Current state and technological impacts related to agribusiness in Somalia

Variables	n	%
The current state of agricultural supply chains		
Very poor	16	20.0
Poor	36	45.0
Moderate	28	35.0
Total	80	100.0
Major challenges that Somali agribusinesses face		
Insecurity	22	27.5
Lack of infrastructure	34	42.5
Poor linkage to the market	24	30.0
Total	80	100.0
How does technology enhance Somali agricultural supply chains?		
Access to information	38	47.5
Market access and e-commerce	28	35.0
Data-driven decision-making	14	17.5
Total	80	100.0
Opportunities agribusinesses could take advantage of in Somalia's agricultural supply chain		
Yes	72	90.0
No	8	10.0
Total	80	100.0

In the contemporary global landscape, technology dominates virtually every sector and profoundly influences the lives of the population (Papa, 2017; Singh, 2014). Somalia, as a developing country, is increasingly adopting and integrating modern technology across various sectors (Hilowle, 2024). The research reveals that access to information and communication are significant factors contributing to the improvement of the agricultural supply chain in the country, as indicated by 47.5% of the survey participants. Market access and e-commerce are very vital to agribusiness, and technology continues to advance day by day. The respondents of the study pointed out that access to the market and digitalization of commerce can take part a key role in the improvement of agribusiness, with 35% of them expressing this view. Additionally, 17.5% of respondents emphasized that data-driven decision-making can enhance the agricultural supply chain and agribusiness. Regarding the potential impact on the country's economy, the outlook for agribusiness is positive. A substantial 90% of respondents believe that if developed, agribusiness can significantly contribute to the country's economic growth. The remaining respondents (10%) expressed uncertainty, suggesting a lack of awareness regarding the potential economic contributions of agribusiness.

Investment, technical and support services are the primary need for Somali farmers. According to Abdullahi and Arisoy (2022), traditional practices and inadequate technical and support services from the government and other institutions are the reasons why Somali farmers fail to produce sufficient products for the entire country (Abdullahi and Arisoy, 2022). 57.5% of the research participants responded that investing in the agricultural sector is necessary and may improve the standard of living and the development of the country. Additionally, 25% of them stated that a secure environment is the most critical factor in agriculture and agribusiness in Somalia. Finally, 17.5% of the research participants believe that promoting access to markets is the key requirement for farmers and should be addressed promptly. Government and policymakers should play in improving agricultural supply chains in Somalia.

The private sector is another influencing factor that can have an impact on improving the economy of the country and the standard of living for the people (Fuglie, 2016). In Table 3, the study shows that 37.5% of the respondents answered that knowledge sharing and capacity building can improve the agricultural supply chain. Additionally, 32.5% of them indicated that public-private partnerships (PPPs) contribute to this point, and value chain development and market linkages are considered important, as stated by 22.5% of the respondents. Finally, 7.5% of the respondents mentioned that dialogues and policies could be beneficial for improving the agricultural supply chain. 37.5% of the participants concluded that the most important steps that can improve agribusiness in the agricultural supply chain in the country are collaborating with stakeholders and facilitating market access, while 25% of them stated that technology and innovation are the most important steps that could improve agribusiness.

Table 3. Government, private sector, and improvement strategies in Somalia's agricultural supply chain (ASC)

Variables	n	%
What is your opinion on the government and policymakers' roles in improving Somalia's ASC?		
Creating a secure environment	20	25.0
Investing agricultural sector	46	57.5
Promoting market access	14	17.5
Total	80	100.0
How can the private sector collaborate with the government in enhancing Somalia's ASC?		
Policy advocacy and dialogue	6	7.5
Public-private partnerships (PPPs)	26	32.5
Market linkages and value chain development	18	22.5
Knowledge sharing and capacity building	30	37.5
Total	80	100.0
For improved performance in Somali ASC, which is most crucial?		
Stakeholder collaboration	30	37.5
Market linkage facilitation	30	37.5
Technology and innovation adoption	20	25.0
Total	80	100.0
How can support be provided to Somali farmers for improvement in ASC?		
Supporting their farming system	34	42.5
Infrastructural development	16	20.0
Introducing technology-based farming	22	27.5
Incentivizing small-scale farmers	8	10.0
Total	80	100.0

Somali farmers are in a low-income state, and they need support similar to that provided by the Chinese and US governments to smallholder farmers, including strong extension services, subsidies, a solid manufacturing sector, and infrastructure development that prioritizes the smallholder sector (Carlisle et al., 2019; Sims and Kienzle, 2016). This survey found that supporting farmers' farming system is the most important factor that can improve their participation in agribusiness and the agricultural supply chain, with 42.5% of them agreeing. Introducing technology-based farming is crucial for the farmers, as 27.5% of them responded. Infrastructural development and incentivizing small-scale farmers are two important points that can be developed to contribute to agribusiness, at 20% and 10% respectively.

Table 4. Pearson's correlation of agricultural supply chains

	Technology improvement	Role of government and policymakers
Pearson's Correlation	0.315**	0.315**
Sig.(2-tailed)	0.004	0.004

According to Table 4, there is a highly significant correlation between technology improvement and the role of the government and policy makers for agricultural supply chains ($r=0.315^{**}$, $P=0.004$).

6. Conclusions

The survey conducted in the Afgoye district of the lower Shabelle region, Somalia, highlighted significant challenges facing the agricultural supply chain and agribusiness, including security issues, inadequate infrastructure, and limited access to markets. The research underscores the urgent need for financial support in farming, with over half (57.5%) identifying it as crucial for enhancing living standards. Despite the hurdles faced, Somalia's agriculture sector has significant growth potential, offering opportunities for agribusinesses to play central roles in the distribution process. However, realizing these opportunities depends on addressing major challenges, including weak infrastructure, limited funding sources, and a fragmented market. Additionally, the study highlights the importance of collaborative efforts among stakeholders to establish a more reliable and effective agricultural supply chain system. Investment in infrastructure, improved access to financing, and the implementation of policies encouraging collaboration and coordination are identified as essential steps.

The agricultural sector in Somalia has the potential to become an important driver of economic growth and development with the appropriate strategic approach and coordinated efforts. This change would be extremely beneficial to the nation's general prosperity in addition to opening doors for agribusinesses to succeed. We recommend focusing on research, development, reproduction, and processing of agricultural inputs, along with inspection and certification of agricultural input quality. Establishing private or public insurance systems could further enhance the investment environment. Strengthening local manufacturing of agri-inputs, ensuring the supply of affordable farm equipment, and creating regional supply chains are crucial techniques. Additionally, private certification of seeds and farmer involvement can encourage both foreign and local investment. Finally, strong market linkages among producers, processors, and markets are emphasized to enhance coordination and reduce sector fragmentation. It is crucial to establish and enforce quality standards to ensure Somali products meet global market demands and enhance their reputation. These steps are essential for fostering sustainable growth and competitiveness in Somalia's agricultural sector.

Author Statement

Both authors contributed substantially to the research design, searching literature review, data collection, data analysis, write-up, and editing of the manuscript. All authors reviewed the results and approved the final version of the manuscript.

Conflict of Interest

The authors declare no conflict of interest.

References

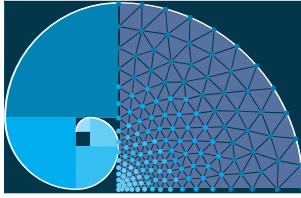
- Abdi-Soojeede, M. I. (2018). Crop production challenges faced by farmers in Somalia: A case study of Afgoye District farmers. *Agricultural Sciences*, 9(8), 1032-1046. <https://doi.org/10.4236/as.2018.98071>
- Abdullahi, A. A., & Arisoy, H. (2022). Agricultural structure in Somalia. *Eurasian Journal of Agricultural Economics (EJAE)*, 2(1), 1-14.

- Ahmed, A. M., Gele, A. O. M., & Ali, A. M. (2023). Logistics solutions, supply chains, climate change, and sustainable development in Somalia. *International Journal of Sustainable Development & Planning*, 18(11). <https://doi.org/10.18280/ijstdp.181116>
- Ali, A. O. (2022). Challenges facing agribusiness sector in Lower Shabelle Region, Somalia. *East African Journal of Business and Economics*, 5(1). <https://doi.org/10.37284/eajbe.5.1.659>
- Ali, I. I., Ahmed, I. A., Kheire, A. M., Abdi, A. W. M., Hassan, I. A., Ibrahim, I. A., Mohamed, I. A., Ali, I. M., Abdullahi, O. O., & Abdullahi, Y. M. (2024). Comparative study of the effects of organic and inorganic fertilizers on the growth and yield of onion (*Allium cepa* L.) in Somalia. <https://doi.org/10.5281/zenodo.10730324>
- Carlisle, L., De Wit, M. M., DeLonge, M. S., Calo, A., Getz, C., Ory, J., Munden-Dixon, K., Galt, R., Melone, B., & Knox, R. (2019). Securing the future of US agriculture: The case for investing in new entry sustainable farmers. *Elementa: Science of the Anthropocene*, 7, 17. <https://doi.org/10.1525/elementa.356>
- FAO, & Bank, W. (2018). Rebuilding resilient and sustainable agriculture in Somalia.
- FAO, CTA, & IFAD. (2014). Youth and agriculture: Key challenges and concrete solutions. Retrieved from <https://openknowledge.fao.org/server/api/core/bitstreams/408708f0-82dc-418e-b92b-e2d7ec0cd2e6/content>.
- Fuglie, K. (2016). The growing role of the private sector in agricultural research and development worldwide. *Global Food Security*, 10, 29-38. <https://doi.org/10.1016/j.gfs.2016.07.005>
- Gaal, H. O., & Afrah, N. (2017). Lack of infrastructure: The impact on economic development as a case of Benadir region and Hir-shabelle, Somalia. *Developing Country Studies*, 7(1).
- Gardner, J., & El-Bushra, J. (2017). Somalia: A state of male power, insecurity and inequality. In *Nairobi: Rift Valley Institute (Briefing Paper)*.
- Gavin, R., Haji, H., & Porter, P. (2019). The relative contributions of cereal production, imports, and aid to Somali food security. *African Journal of Food, Agriculture, Nutrition and Development*, 19(3), 14587-14601. <https://doi.org/10.18697/ajfand.86.18025>
- Heritage Institute. (2020). *Somalia's agriculture and livestock sectors: A baseline study and a human capital development strategy*.
- Hastings, J. V., Phillips, S. G., Ubilava, D., & Vasnev, A. (2022). Price transmission in conflict-affected states: Evidence from cereal markets of Somalia. *Journal of African Economies*, 31(3), 272-291. <https://doi.org/10.1093/jae/ejab012>
- Hilowle, I. F. (2024). The impact of technology on economic development in Somalia. *Multidisciplinary Journal of Horseed International University (MJHIU)*, 2(1), 152-170. <https://doi.org/10.59336/tp5y6803>
- Jayne, T. S., Mather, D., & Mghenyi, E. (2010). Principal challenges confronting smallholder agriculture in sub-Saharan Africa. *World Development*, 38(10), 1384-1398. <https://doi.org/10.1016/j.worlddev.2010.06.002>
- Kullane, M. A., Abdi-Soojeede, M. I., & Farah, A. M. (2022). Impacts of charcoal production on environment and species preference in Yaqshid District Mogadishu, Somalia. *Journal of Agriculture and Ecology Research International*, 65-74. <https://doi.org/10.9734/jaeri/2022/v23i530238>

- Little, P. D. (1996). Conflictive trade, contested identity: The effects of export markets on pastoralists of southern Somalia. *African Studies Review*, 39(1), 25-53.
- Mifsud, M. (2007). Civil and food insecurity in Somalia: An analysis. *Africa: Rivista Trimestrale di Studi e Documentazione dell'Istituto Italiano per l'Africa e l'Oriente*, 62(3), 439-442.
- Mohamed, M. M., Isak, N. N., & Ali, A. Y. S. (2015). The contribution of crops and livestock production on Somali export: Regression analysis using time series data. *Journal of Economics and Sustainable Development*, 6(7).
- Muchiri. (2007). Climate of Somalia. *Technical Report No W-01, FAO-SWALIM, Nairobi, Kenya*. https://www.faoswalim.org/resources/site_files/W01%20Climate%20of%20Somalia_0.pdf
- NET, F. (2022). Somalia food security outlook, June 2021 to January 2022. From reliefweb.int website: <https://reliefweb.int/report/somalia/somalia-food-security-outlook-june-2021-january-2022>.
- Papa, S. F. (2017). Use of blockchain technology in agribusiness: Transparency and monitoring in agricultural trade. *2017 International Conference on Management Science and Management Innovation (MSMI 2017)*.
- Pape, U. J., & Wollburg, P. R. (2019). Impact of drought on poverty in Somalia. *World Bank Policy Research Working Paper* (8698).
- Said, M., Adan, A. B., & Hussein, A. B. (2023). Analysis of climate change impacts on food security in Somalia. *International Journal of Media and Networks*, 1(1), 101-107.
- Said, M., & Ibrahim, M. M. (2023). A comprehensive overview of challenges and prospects in large-scale rice production among farmers in Jawhar, Middle Shabelle, Somalia. *Biomedical Journal of Scientific & Technical Research*, 52(5), 44155-44163. <https://doi.org/10.26717/BJSTR.2023.52.008321>
- Said, M. A., & Hassan, A. (2024). Advanced assessment of socioeconomic impacts resulting from flooding: A case study of Beledweyne, Hiran, Somalia. *Journal of Earth & Environmental Waste Management*, 2(2), 1-9.
- Schaffnit-Chatterjee, C. (2014). Agricultural value chains in Sub-Saharan Africa. *Deutsche Bank Research*.
- Sims, B., & Kienzle, J. (2016). Making mechanization accessible to smallholder farmers in sub-Saharan Africa. *Environments*, 3(2), 11. <https://doi.org/10.3390/environments3020011>
- Singh, B. (2014). Technology based entrepreneurship in agriculture role of agribusiness incubators. *International Journal of Management and International Business Studies*, 4(3), 249-254.
- Sjah, T., & Zainuri, Z. (2020). Agricultural supply chain and food security. © Springer Nature Switzerland AG 2020, W. Leal Filho et al. (eds.), *Zero Hunger, Encyclopedia of the UN Sustainable Development Goals*. https://doi.org/10.1007/978-3-319-69626-3_82-1
- SOMINVEST. (2022). Agribusiness opportunities in Somalia's food production sector.
- Ssozi, J., Asongu, S., & Amavilah, V. H. (2019). The effectiveness of development aid for agriculture in Sub-Saharan Africa. *Journal of Economic Studies*, 46(2), 284-305. <https://doi.org/10.1108/JES-11-2017-0324>

Waris, H. F. (2018). Supply chain management and organizational performance of manufacturing companies in Mogadishu-Somalia [Kampala International University, College of Economics and Management].

Somalia National Development Plan 2020 to 2024 (2020). <https://www.salaamcenter.org/wp-content/uploads/2023/09/SDC-PROFILE-Updated-2023.pdf>



Utilization of Short Span Web-Tapered Beams Using Flexible Nodal Bracing

Fatma K m rc ¹  Oğuzhan Toğay^{1,*} 

¹ İzmir Katip Çelebi University, Faculty of Engineering and Architecture, Department of Civil Engineering

* Corresponding author: oguzhan.togay@ikc.edu.tr

Received: 14.06.2024

Accepted: 30.07.2024

Abstract

The use of steel structures with varying cross-sectional dimensions along their length is common, with nodal braces playing a critical role in enhancing their load-carrying capacity and stability. These braces distribute loads within the structure and improve resistance to lateral forces. Current design guidelines, such as American Institute of Steel Construction (AISC) Design Guide 25 and AISC 360-22, offer a general framework for elements with fixed brace conditions and prismatic cross-section. This study aims to be a pioneering investigation into the variation of brace force values in short-span and compact web-tapered beams under a single loading condition. The article seeks to comprehensively examine the requirements and limits of brace force in short-span web-tapered compact beams. To achieve this goal, parametric finite element analyses are utilized to explore how brace force changes concerning beam geometry and material properties under a single loading condition. The beam used was considered as doubly symmetric and divided into 100 nodes and supported by a nodal brace at the middle node. The beam is 2540 mm (100 in) long, its depth tapering from 1066.8 mm (42 in) to 924.6 mm (36.4 in) over its span and unbraced length is 1270 mm (50 in). In terms of finite element analysis, the software utilized significantly influences the accuracy and reliability of results, particularly in scenarios involving inelastic nonlinear analysis. In this study, the ABAQUS software was employed specifically to conduct parametric finite element analyses, considering the complexities of inelastic material behavior. Maximum Brace Force value that has been found in the simulation studies has been found as 2.15%. Consequently, the findings of this research are intended to contribute to the development of a new design method for determining the requirements and limits of brace force in short-span, determining required brace stiffness and variable cross-sectional dimension compact beams, to contribute to the safe and economical design of such beams, and to provide engineers with ideas to consider and data to use in their designs.

Keywords: Web-tapered beam; brace; brace force; compact beam; finite element method

1. Introduction

In structural engineering, the design and analysis of steel beams are critical for ensuring safety and efficiency in construction. Steel structures offer significant advantages over other types of structures due to the flexibility of variable cross-section elements and the ability to produce welded sections. One such structural member is the web-tapered section steel members. These

web-tapered sections can be enhanced by the addition of nodal bracing at the mid-section to increase load-bearing capacity and stability. This study focuses on short-span web-tapered compact welded I-section beams that are supported by a flexible nodal brace at the midspan of its top flange. This study was designed in a limited scope to examine the performance of short span beams in the initial phase of the research. It is planned to expand the scope and examine other beam types in future studies.

Miller (2003) highlighted the lack of design equations for web-tapered I-section beams, emphasizing the need for further research in this area, particularly in the inelastic range using nonlinear finite element analysis. Also, the author mentioned that behavior of web-tapered I-shaped beams at the ultimate stage may be determined by a number of variables, including the flange width, flange thickness, web thickness, unbraced length, tapering angle, etc., according to the results of the current parametric research. The author also showed in his study that the plate slenderness ratios in the American Institute of Steel Construction (AISC) 360-22 (2022) Load and Resistance Factor Design (LRFD) Table B4.1 are inadequate for compact beam behavior in adequately braced web-tapered I-shaped beams in order to provide accurate estimates for the elastic buckling resistance. Soltani et al. (2019) examined the lateral buckling of three comprehensive I-beam examples. These included simply supported doubly symmetric I-sections and axially varied materials in both homogeneous and inhomogeneous tapered beams, utilizing a new finite element approach. Soltani and Asgarian (2020) developed a finite element model to assess the lateral-torsional stability of axially functionally graded beams featuring tapered bi-symmetric I-sections under a range of boundary conditions. Asgarian et al. (2013) developed a theoretical and numerical model based on the power series method for beams with arbitrary cross-sections and boundary conditions. Lateral buckling loads were determined by solving the eigenvalue problem of the algebraic system derived from this model. The study compared these results with finite element solutions obtained through established numerical or analytical methods, such as Ansys software, and concluded that the proposed method is effective for analyzing the stability of both tapered beams and beams with constant cross-sections. Mercuri et al. (2020) highlighted that the use of approximate methods becomes necessary due to the complexity of analytical solutions for tapered sections. It is noted that commercial software often fails to accurately account for the features of non-prismatic beams, resulting in inconsistent structural analyses, erroneous stress distribution estimations, and rough predictions of the structural element's strength. In the study, the stiffness matrix was analytically defined for both homogeneous prismatic and tapered beams, and the resulting finite element outcomes were compared with the results obtained from SAP2000 for the same beams. Toğay (2024) examined the inelastic nonlinear buckling analysis with stiffness reduction factors used in web-tapered I sections, compared this analysis with finite element analysis and found a 98.6% agreement. This study emphasized the consistency of inelastic nonlinear buckling analysis especially in fixed-supported web-tapered I sections and the usability of inelastic nonlinear buckling analysis in this field.

Foster and Gardner (2013) used a geometrically and materially non-linear finite element model to conduct a series of experiments on simply supported beams with variations in restraint spacing and stiffness. Authors found that at the minimum required stiffness, restraint forces reached their peak values, but increasing the stiffness beyond this point caused the forces to reduce rapidly and ensured that full capacity of the restrained member was reached. Tankova et al. (2018) tested two full-scale numerical models including all relevant parameters such as geometric and material defects under varying bending moments with experiments on web-tapered steel elements, and summarized the results obtained from each experiment and formed the basis for further studies.

Wang & Nethercot (1990) performed a parametric study addressing bracing requirements for unrestrained beams. For single-bracing systems, authors recommend 1% of axial force in a flange at failure as the bracing-strength requirement. For multiple-bracing systems, a total value of 2% is suggested, with a maximum of 1% for each brace, especially for beams with high slenderness. Lay and Galambos (1966) and Mohammadi et al. (2016) both addressed the design and bracing requirements for steel beams. Lay and Galambos (1966) emphasized the importance of axial strength, axial stiffness, and bending strength in the design of bracing for inelastic steel beams. Mohammadi et al. (2016) studied the brace stiffness requirement additional to the elastic lateral torsional buckling of monosymmetric I-beams under pure bending condition. Both studies provide valuable insights into the factors that need to be considered in the design and bracing of steel beams. Bishop (2013) created a method for calculating inelastic eigenvalue buckling to identify the optimal bracing stiffness needed in general frame systems for metal buildings. He also offered guidelines for the necessary design stiffness and strength of brace components using this calculation tool.

AISC Design Guide 25 (2022) provides comprehensive information on the adequacy of fixed bracing for elements, detailing the critical points to consider in inelastic nonlinear analyses. The guide elaborates on the fixed bracing requirements and calculation methods for symmetrical linearly tapered elements through various examples, and it offers safe calculations for braced points at different unbraced lengths. AISC Design Guide 25 also recommends using computer-aided analysis methods to determine the accuracy and effectiveness of bracing systems. Wijaya et al. (2019) found that AISC Design Guide 25 calculates the critical moment accurately for long beams but not accurately for short beams.

The application of flexible nodal bracing is a common technique to enhance the stability of beams in their transverse direction. The AISC 360-22 (2022) Specification provides simplified design equations for various bracing situations, including "relative" and "nodal" lateral bracing of columns and beams, and "nodal" and "continuous" torsional bracing of beams. According to the AISC guidelines, the brace force demand should typically be within a certain percentage to ensure adequate performance. The inelastic finite element nonlinear analysis used in this study, in light of the operations performed with the finite element method in finite element program, revealed that the brace force demand can increase up to 2.15% instead of the 2% for compact members typically predicted by the AISC. This observed increase should be taken into account in terms of brace stability.

To achieve this result, the compactness of the beam sections was first determined by performing compactness equations mentioned at AISC Appendix 6 Table B4.1b. These calculations allow the identification of the thickness range necessary for the beam to be considered compact. Subsequently, parametric finite element analysis was then used using the selected compact range for flange thickness and web thickness. Considering the complexity of inelastic and nonlinear material behavior, ABAQUS software (Dassault Systèmes / Simulia, 2020) was employed for the finite element analyses. Load proportion factor and node displacement values were obtained from the analyses according to various stiffness values. These parameters were then used to calculate the percentage brace force demand.

The findings of this study may have important implications for the design of mentioned web tapered steel beams; a method may be provided to increase brace force demand to 2.5%. This article aims to detail the methodology, analysis, and results, providing insights into the practical applications of flexible brace in beam design.

2. Methodology

In this study, a short span welded web-tapered steel beam with a total length of 2540 mm (100in) was used. The 3-d view of beam used is given in Figure 1(a). The material used was ASTM A992 Grade 50 or a similar high-strength structural steel grade. For this steel grade, the modulus of elasticity (E) was taken as 200,000 MPa (29,000 ksi), the yield strength (F_y) as 379.21 MPa (55 ksi), and the tensile strength (F_u) as 547 MPa (79.31 ksi). A flexible nodal brace with variable stiffness was placed at the midpoint of the beam's top flange, dividing the length of the beam in half as shown in Figure 1(b). The height of the beam between top and bottom flanges varies uniformly tapered from 1066.8 mm (42 in) at one end to 924.6 mm (36.4in) at the other end as shown in Figure 1(b). At the point where the brace is located, the web height is 996 mm (39.205 in), and the unbraced length was set to 1270 mm (50in). The flange width is 228.6 mm (9 in).

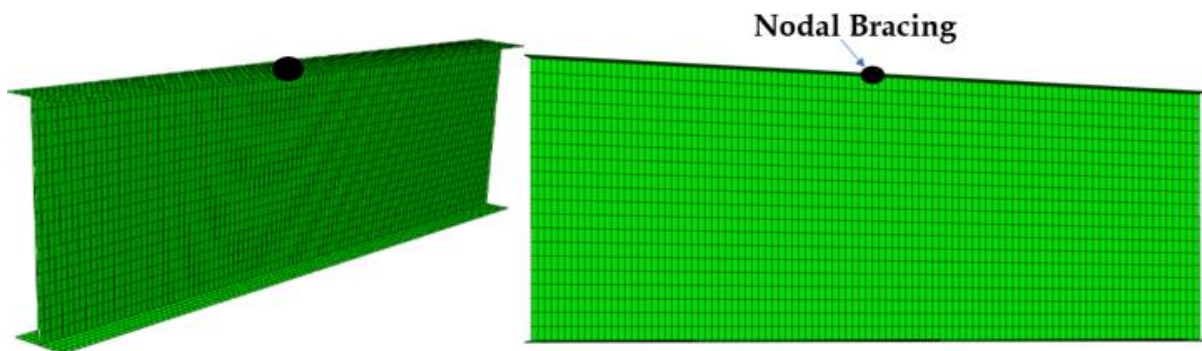


Figure 1. Finite element model of web tapered beam (a) 3-d view and (b) X-Y axis view

The inelastic nonlinear analysis of the beam under an applied moment at the left end was performed as shown in Figure 2(a). The loading condition is described by a moment diagram that forms a right-angled triangle, with the maximum moment at the left end, decreasing towards the right, as shown in Figure 2(b). The inelastic nonlinear analysis of the beam performed within the compact web thickness and flange thickness ranges. First, the compact range for web and flange thickness were calculated according to AISC 360-22 Table B4.1b “Width-to-thickness ratios: Compression elements members subject to flexure”. The flange used in this study corresponds to Case 11 of Table B4.1b “flanges of doubly and singly symmetric I-shaped built-up sections” in the table, and the web section corresponds to Case 15 of Table B4.1b “webs of doubly-symmetric I-shaped sections and channels”.

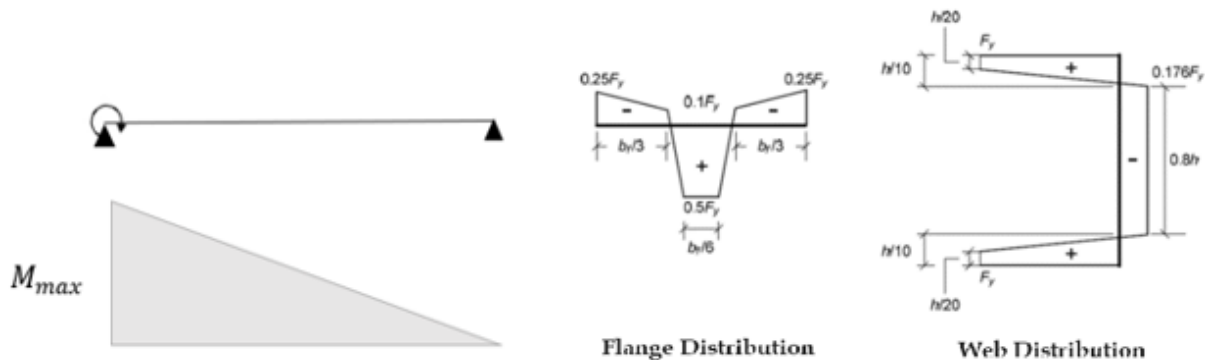


Figure 2. (a) Applied moment illustration, (b) Moment diagram of the beam and (c) Best-Fit Prawl Pattern residual stress (Adapted from Jeong et al. 2016)

For flanges of doubly and singly symmetric I-shaped built-up sections:

$$\frac{b}{t} \leq 0.38 \sqrt{\frac{E}{F_y}} = \lambda_p \quad (1)$$

$$\frac{b}{t} \leq 0.95 \sqrt{\frac{k_c E}{F_L}} = \lambda_r \quad (2)$$

In the formulas (1) and (2), b corresponds to half of the width of the flange, and t is the thickness of the flange. E means the modulus of elasticity of steel, which is 200,000 MPa (29,000 ksi). F_y means the specified minimum yield stress, which is 379.21 MPa (55 ksi). As given in AISC 360-22 Table B4.1b $k_c = \frac{4}{\sqrt{h/t_w}}$ but shall not be taken less than 0.35 nor greater than 0.76 for calculation purposes, h is the distance between flanges. Similarly, as mentioned in same table, $F_L = 0.7F_y$ for major axis bending of compact and noncompact web built-up I-shaped members with $S_{xt}/S_{xc} \geq 0.7$.

For webs of doubly-symmetric I-shaped sections and channels:

$$\frac{h}{t_w} \leq 3.76 \sqrt{\frac{E}{F_y}} = \lambda_p \quad (3)$$

$$\frac{h}{t_w} \leq 0.38 \sqrt{\frac{E}{F_y}} = \lambda_r \quad (4)$$

In the formulas (3) and (4), h corresponds to the distance between flanges, and t_w is the thickness of the web section. Again, E means the modulus of elasticity of steel, which is 200,000 MPa (29,000 ksi) and F_y means the specified minimum yield stress, which is 379.21 MPa (55 ksi).

The findings were tabulated in Table 1. Web thicknesses greater than 11.43 mm (0.45 in) and flange thicknesses greater than 13.97 mm (0.55 in) were found to be compact. To obtain results, flange thicknesses between 13.97 mm (0.55 in) and 25.4 mm (1 in) and web thickness ranges between 11.43 mm (0.45 in) and 19.05 mm (0.75 in) were selected within the compact range. Subsequently, for each thickness within this range, inelastic nonlinear analysis was performed using the finite element method by the ABAQUS software (Dassault Systèmes / Simulia, 2020). Since the number of cases is high, Python code written to automate the results and speed up the processes was utilized.

Finite element models of tapered beam cross-sections, with the top flange height tapering from one end to the other, were developed using ABAQUS. The test elements were modeled using a four-node shell element (S4R) for all section components. For all scenarios, the deeper side of the web was exposed to a bending moment. Using Type 1 spring elements in ABAQUS, a single brace was applied at the midspan of the tapered beam, at the top flange height, and connected to the flange-web intersection. The brace stiffness was gradually increased from 0.25 kip/in to 1500 kip/in to reflect the minimum and maximum capacities achievable with a fixed brace. In the study conducted by Lokhande (2014) using Advanced Finite Element Analysis for the strength evaluation of doubly symmetric I-section beams and column-beams, four-node S4R shell elements were used to model the flanges and web of the element while using ABAQUS software.

The shell finite element analysis models integrated residual stresses by employing an existing residual stress pattern (Pattern I). Best-fit Prawel pattern that shown in Figure 2(c) applied in this research. This pattern, valued for its self-equilibrating properties within each component, has been previously utilized by Jeong et al. (2016) for welded cross section.

These imperfection patterns are generated using the geometric imperfection tolerances specified in AWS (2010) and AISC Code of Standard Practice (COSP) (2022). To obtain flange tilt and web out-of-flatness patterns, inelastic eigenvalue buckling analysis is conducted on members with out-of-plane displacements restrained at the top and bottom flange-web juncture points, under uniform axial compression as shown in Figure 3(a). This analysis yields buckling modes, which are then used to isolate and scale the flange tilt and web out-of-flatness patterns to half the tolerance values as has been previously utilized and mentioned by Toğay et al. (2018). Besides the previously discussed imperfections, a flange sweep is introduced at the web-flange juncture points in the Critical Segment (CS). A sinusoidal flange sweep is applied specifically to the top flange, which experiences flexural compression. Conversely, the bottom flange, which is under flexural tension, remains without any sweep, as illustrated in Figure 3(b).

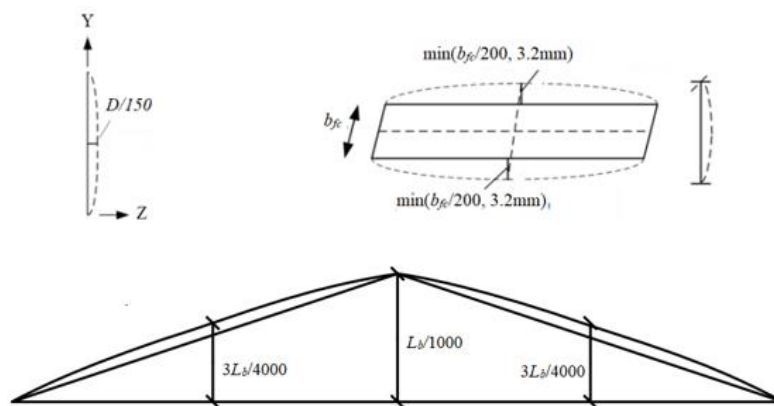


Figure 3. (a) Web out-of-flatness and flange tilt imperfections, and (b) applied imperfections (the AWS/AISC COSP Flange Sweep Tolerance). (Adapted from Toğay and White, 2018)

As a result of these analyses, nodal displacement and load proportionality factor were obtained for a series of stiffness values ranging from 350.25 kN/m (2 kip/in) to 262,690.2 kN/m (1500 kip/in). With these results, compression force at midsection of top flange and brace force were calculated. Then, the brace force was divided by the compression force at midsection of top flange to obtain a percentage value called “brace force demand” for each thickness combination.

Following these calculations, the required brace stiffness was determined according to the procedures outlined in both the AISC 360-22 specification and its commentary. Specifically, it was calculated using the formulas given below under Appendix 6 “Stability Bracing for Beams” Nodal Bracing heading and Commentary Appendix 6 “Stability Bracing for Beams” Lateral bracing heading

Nodal Bracing according to Specification Appendix 6 is;

$$\beta = \frac{10 \times M_r \times C_d}{L_{br} \times h_o \times \Phi} \tag{5}$$

$$P_{rb} = \frac{0.02 \times M_r \times C_d}{h_o} \tag{6}$$



Figure 4. Required flexural strength M_r representation for calculation from moment diagram

$$M_r = \frac{P_{applied} \times h_1 \times (LPF)_{max}}{2} \tag{7}$$

Lateral bracing according to Commentary Appendix 6 is;

$$\beta = \frac{2 \times N_i \times C_t \times P_f \times C_d}{L_{br} \times \Phi} \tag{8}$$

$$P_f = \frac{M_r}{h_o} \tag{9}$$

In the formulas (5), (6), (7), (8), and (9), M_r is required flexural strength using LRFD load combinations at brace point and found from moment diagram shown as Figure 4. C_d is 1 for single curvature bending case, C_t constant is 1 for centroidal loading case. h_o is section height distance between flange centroids in brace point, h_1 is height distance between flange centroids of left side of the beam, and L_{br} is unbraced length and all shown in Figure 5. Φ taken as 1 for performing nominal analysis, P_f is beam compressive flange force, P_{rb} required strength, $P_{applied}$ is applied load and $(LPF)_{max}$ is maximum load proportionality factor found from inelastic nonlinear analysis. For nodal bracing N_i is $= 4 - \frac{2}{n}$ and n is number of braces. Dimensions are illustrated in Figure 5(a) for the side view of the beam and in Figure 5(b) for the front view.

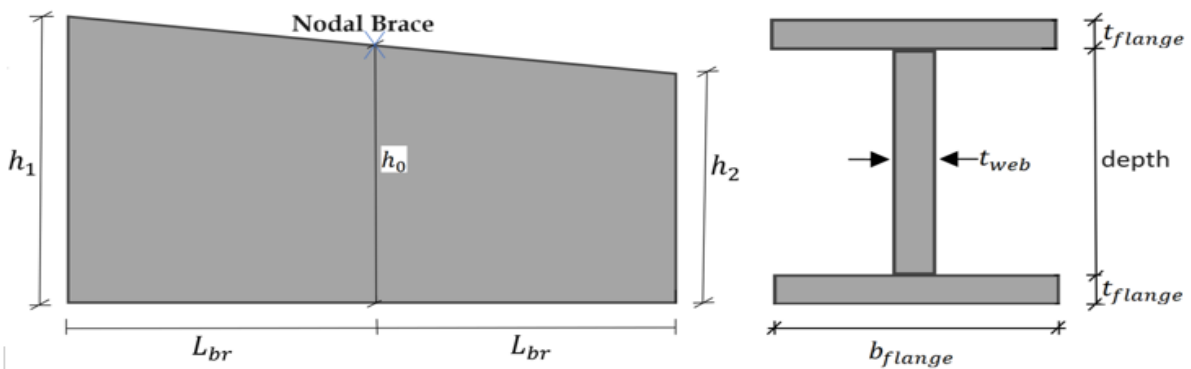


Figure 5. Bracing placement (a) and dimension illustration (b) of section

3. Results

In this section, selected compact thickness ranges are presented for the inelastic nonlinear analysis, which were determined based on the formulas provided in the previous section. The

dimension for flange thickness were chosen to be between 13.97 mm (0.55 in) and 25.4 mm (1 in) as they fall within the compact range. Similarly, the dimension for web thickness were chosen to be between 11.43 mm (0.45 in) and 19.05 mm (0.75 in). The cases studied in the analysis are shown in Table 1.

Table 1. Compact web and flange thickness range

Web thickness (mm)	11.43	12.7	13.97	15.24	16.51	17.78	19.05			
Flange thickness (mm)	13.97	15.24	16.51	17.78	19.05	20.32	21.59	22.86	24.13	25.4

The inelastic nonlinear analysis was performed for each of these thickness combinations using the finite element method with the ABAQUS software. For each flange thickness-web thickness combination, 21 different stiffness values were analyzed individually. The brace force and the compression force at the midsection of the top flange were obtained in all thickness combinations. The required brace force demand was calculated as the ratio of these two forces as mentioned in previous section for all cases. A total of 1470 analyses were conducted, and the results for the required brace force demand for each combination are shown in Table 2.

Table 2. Required brace force percentage demand for sections

%		Flange Thickness (mm)									
		13.97	15.24	16.51	17.78	19.05	20.32	21.59	22.86	24.13	25.4
Web Thickness (mm)	11.43	2.15	2.03	1.98	1.92	1.26	1.85	1.25	1.77	1.74	1.73
	12.7	2.02	1.88	1.83	1.7	1.76	1.75	1.73	1.45	1.31	1.69
	13.97	1.84	1.79	1.73	1.66	1.68	1.73	1.75	1.68	1.77	1.73
	15.24	1.84	1.68	1.69	1.68	1.73	1.65	1.73	1.69	1.77	1.77
	16.51	1.73	1.73	1.79	1.76	1.62	1.64	1.8	1.73	1.67	1.82
	17.78	1.83	1.79	1.75	2.12	1.66	1.8	1.69	1.81	1.75	1.86
	19.05	1.95	1.89	1.52	1.81	1.7	1.57	1.61	1.82	1.77	1.71

To demonstrate, for a specific case with a flange thickness of 25 mm (1 in) and a web thickness of 20 mm (0.75 in), the required brace force demand and brace stiffness values are presented below in Figure 6. The brace stiffness value for Equation (8) is 668 kN/m (41.04 kip/in) and Equation (5) 1670 kN/m (103 kip/in), brace force demand for this case was found as 1.5% and 1.57% respectively.

To illustrate the results for all cases a graph was derived. These graphs represent the results from the ABAQUS analyses conducted for 21 different stiffness values. Same analyses were performed for each case, and the resulting graphs for a specific case shown below. The generated graph demonstrates the relationship between brace stiffness values and the corresponding brace force demand percentage for cases.

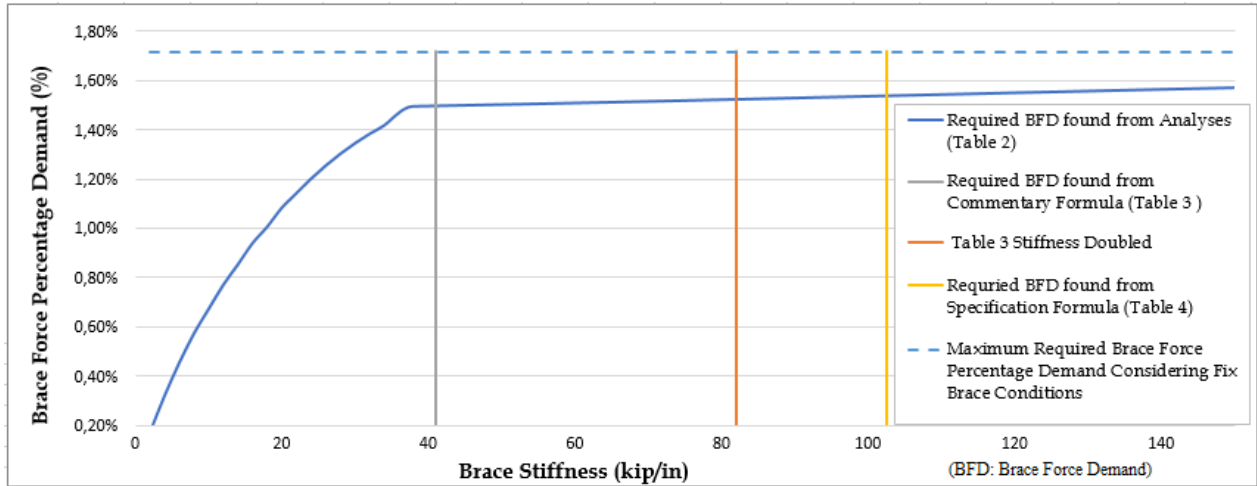


Figure 6. Graph of brace force demand values with respect to stiffness values for example case

As a result of 1470 analyses, brace stiffness values were found for each thickness combination based on the formulas given in previous section. Each of the values shown in Table 3 are the required brace force demand in percentage with respect to beam section brace stiffness values found as a result of the formulas in the AISC commentary mentioned in the methodology.

Table 3. Required brace force percentage demand with respect to brace stiffness values found from Equation (8)

		Flange Thickness (mm)									
		13.97	15.24	16.51	17.78	19.05	20.32	21.59	22.86	24.13	25.4
Web Thickness (mm)	11.43	1.98	1.81	1.75	1.69	1.14	1.47	1.1	1.39	1.33	1.34
	12.7	1.87	1.7	1.64	1.56	1.56	1.41	1.34	1.33	1.04	1.34
	13.97	1.74	1.67	1.55	1.56	1.46	1.41	1.41	1.32	1.32	1.3
	15.24	1.7	1.56	1.61	1.55	1.5	1.45	1.41	1.38	1.38	1.34
	16.51	1.65	1.61	1.7	1.61	1.6	1.53	1.53	1.42	1.41	1.41
	17.78	1.75	1.73	1.67	1.55	1.61	1.6	1.56	1.48	1.5	1.47
	19.05	1.88	1.83	1.52	1.79	1.63	1.59	1.54	1.5	1.4	1.5

Correspondingly, the values shown in Table 4 are the required brace force demand in percentage with respect to beam section brace stiffness values found as a result of the formulas in AISC specification Appendix 6 mentioned in the methodology.

Table 4. Required brace force percentage demand with respect to brace stiffness values found from Equation (5)

%	Flange Thickness (mm)									
	13.97	15.24	16.51	17.78	19.05	20.32	21.59	22.86	24.13	25.4
11.43	2.12	2	1.99	1.8	1.21	1.64	1.19	1.52	1.41	1.48
12.7	2	1.88	1.84	1.66	1.6	1.58	1.44	1.41	1.17	1.44
13.97	1.81	1.8	1.75	1.67	1.58	1.56	1.57	1.42	1.41	1.38
15.24	1.81	1.64	1.69	1.67	1.62	1.57	1.55	1.43	1.42	1.44
16.51	1.7	1.72	1.75	1.71	1.61	1.6	1.6	1.58	1.46	1.44
17.78	1.8	1.79	1.73	1.73	1.64	1.7	1.6	1.56	1.54	1.57
19.05	1.95	1.84	1.47	1.8	1.69	1.57	1.55	1.56	1.48	1.57

In order to interpret the conducted studies, the brace force demand values obtained from the analysis results initially and presented in Table 2 were compared with the brace force demand values found from brace stiffness values calculated subsequently as mentioned above and shown in Table 3 and Table 4, with the comparison results shown in Table 5. The purpose of this comparison was to observe whether the demands found based on the brace stiffness could meet the values obtained from the section analysis. As a result of this comparison, if the value obtained from the analysis results was greater than the value found based on the brace stiffness, it was shown in the table as red; otherwise, it was shown as light green. In the table, each cell with the intersection of flange thickness-web thickness is divided by 2. While the left part of the divided cells shows the result of comparing Table 2 and Table 3, the right part shows the result of comparing Table 2 and Table 4.

Table 5. Evaluation of Table 2 data in comparison with Table 3 and Table 4 values

Table 3	Table 4	Flange Thickness (mm)																			
		13.97	15.24	16.51	17.78	19.05	20.32	21.59	22.86	24.13	25.4										
Web Thickness (mm)	11.43	Red	Red	Red	Green	Red	Red	Red	Red	Red	Red	Red	Red	Red	Red	Red	Red	Red	Red	Red	Red
	12.7	Red	Red	Green	Red	Green	Red	Red	Red	Red	Red	Red	Red	Red	Red	Red	Red	Red	Red	Red	Red
	13.97	Red	Red	Red	Red	Red	Red	Red	Red	Red	Red	Red	Red	Red	Red	Red	Red	Red	Red	Red	Red
	15.24	Red	Green	Red	Green	Red	Red	Red	Green	Green	Red	Red	Red	Red	Red	Red	Red	Red	Red	Red	Red
	16.51	Green	Green	Green	Green	Green	Green	Green	Green	Green	Green	Green	Green	Green	Green	Green	Green	Green	Green	Green	Green
	17.78	Green	Green	Green	Green	Green	Green	Green	Green	Green	Green	Green	Green	Green	Green	Green	Green	Green	Green	Green	Green
	19.05	Green	Green	Green	Green	Green	Green	Green	Green	Green	Green	Green	Green	Green	Green	Green	Green	Green	Green	Green	Green

Note: Flange thicknesses are divided into two, the box on the left is colored according to the comparison of Table 2 with Table 3, and the box on the right side is colored according to the comparison of Table 2 with Table 4.

Based on Table 5 findings, it is observed that as compactness increases in the web elements, the values for maximum brace force percentage demand in Table 2 appear sufficient. Conversely, as compactness decreases for web members, it is found that the brace force percentage demand values corresponding to brace stiffness in Tables 3 and 4 exceed those in Table 2.

Furthermore, while increasing flange thickness does not show a discernible effect, increasing web thickness appears to render the maximum brace force percentage demand values in Table 2 sufficient. These findings illustrate the sensitivity of brace force demands to compactness and the geometric characteristics of structural elements as analyzed in the study.

4. Conclusions

This study has conducted a comprehensive inelastic nonlinear analysis to investigate the brace force demands for various combinations of flange and web thicknesses using the finite element method with ABAQUS software. The findings of this research highlight several key insights into the relationship between brace stiffness values and the corresponding brace force demands.

The analyses revealed that the compactness of web elements significantly impacts the maximum brace force percentage demand. Specifically, as the compactness of web elements increases, the brace force demands derived from the analysis are found to be adequate. Conversely, for less compact web elements, the brace force demands based on the calculated brace stiffness values exceed those obtained from the section analysis.

Additionally, while variations in flange thickness did not demonstrate a significant effect on the brace force demands, an increase in web thickness contributed to achieving sufficient brace force percentage demands. This indicated a notable sensitivity of brace force demands to the compactness and geometric characteristics of the structural elements under consideration.

The results suggest that, for optimal design, attention must be given to the compactness of web elements to ensure that the brace force demands can be met effectively.

Overall, this study contributes to a deeper understanding of the factors influencing brace force demands and provides valuable insights for the design and assessment of structural elements subjected to inelastic nonlinear behavior. Future research could expand on these findings by exploring additional geometric configurations and material properties to further refine the predictive models for brace force demands in structural engineering applications.

Author Statement

The authors confirm contribution to the paper as follows: F. Kömürçü: analysis and interpretation of results, data collection, draft manuscript preparation; O. Toğay: analysis and interpretation of results, draft revision. All authors reviewed the results and approved the final version of the manuscript.

Conflict of Interest

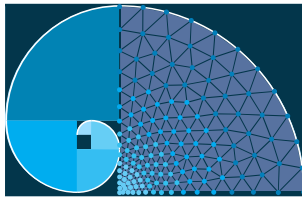
The authors declare no conflict of interest.

References

- AISC (2016). *Specification for Structural Steel Buildings*, ANSI/AISC 360-22, American Institute of Steel Construction, Chicago, IL.
- AISC (2022). *Specification for Structural Steel Buildings*, ANSI/AISC 360-22, American Institute of Steel Construction, Chicago, IL.

- AISC (2022). *ANSI/AISC 303-22: COSP-Code of standard practice for steel buildings and bridges*, American Institute of Steel Construction.
- AWS (2010). *Structural Welding Code-Steel*, AWS D1.1: D1.1M, (22nd ed.), prepared by AWS Committee on Structural Welding.
- Asgarian, B., Soltani, M., & Mohri, F. (2013). Lateral-torsional buckling of tapered thin-walled beams with arbitrary cross-sections. *Thin-Walled Structures*, 62, 96-108. <https://doi.org/10.1016/j.tws.2012.06.007>
- Bishop, C. D. (2013). *Flange bracing requirements for metal building systems* (Doctoral dissertation, Georgia Institute of Technology). Georgia Institute of Technology.
- Dassault Systèmes / Simulia. (2020). *ABAQUS/Standard user's manual version 6.20*. Hibbit, Karlsson & Sorensen Inc.
- Foster, A. S. J., & Gardner, L. (2013). Ultimate behaviour of steel beams with discrete lateral restraints. *Thin-Walled Structures*, 72, 88-101. <https://doi.org/10.1016/j.tws.2013.06.009>
- Jeong, W. Y., Toğay, O., Lokhande, A. M., & White, D. W. (2016). An introspective assessment of buckling and second-order load-deflection analysis based design calculations. In *Proceedings of the Annual Stability Conference*. Structural Stability Research Council. Orlando, FL.
- Lay, M. G., & Galambos, T. V. (1966). Bracing requirements for inelastic steel beams. *Journal of the Structural Division*, 92(2), 53-68. <https://doi.org/10.1061/JSDEAG.0001421>
- Lokhande, A. M. (2014). *Evaluation of steel I-section beam and beam-column bracing requirements by test simulation* (Master's thesis, Georgia Institute of Technology). Georgia Institute of Technology.
- Mercuri, V., Balduzzi, G., Asprone, D., & Auricchio, F. (2020). Structural analysis of non-prismatic beams: Critical issues, accurate stress recovery, and analytical definition of the Finite Element (FE) stiffness matrix. *Engineering Structures*, 213, 110252. <https://doi.org/10.1016/j.engstruct.2020.110252>
- Miller, B. S. (2003). *Behavior of web-tapered built-up I-shaped beams* (Master's thesis). University of Pittsburgh.
- Mohammadi, E., Hosseini, S. S., & Rohanimanesh, M. S. (2016). Elastic lateral-torsional buckling strength and torsional bracing stiffness requirement for monosymmetric I-beams. *Thin-Walled Structures*, 104, 116-125. <https://doi.org/10.1016/j.tws.2016.03.009>
- Soltani, M., Asgarian, B., & Mohri, F. (2019). Improved finite element model for lateral stability analysis of axially functionally graded nonprismatic I-beams. *International Journal of Structural Stability and Dynamics*, 19(09). <https://doi.org/10.1142/S0219455419501086>
- Soltani, M., & Asgarian, B. (2020). Exact stiffness matrices for lateral-torsional buckling of doubly symmetric tapered beams with axially varying material properties. *Iranian Journal of Science and Technology, Transactions of Civil Engineering*. <https://doi.org/10.1007/s40996-020-00402-z>
- Tankova, T., Martins, J. P., Simões da Silva, L., & Marques, L. (2018). Experimental lateral-torsional buckling behaviour of web tapered I-section steel beams. *Engineering Structures*, 168(4), 168-184. <https://doi.org/10.1016/j.engstruct.2018.04.084>

- Toğay, O. (2018). *Advanced Design Evaluation Of Planar Steel Frames Composed Of General Nonprismatic I-Section Members*. Doctoral Dissertation, School of Civil and Environmental Engineering, Georgia Institute of Technology, Atlanta, GA, 273pp.
- Toğay, O. (2024). Application of inelastic nonlinear buckling analysis with stiffness reduction factors to web tapered I sections. *Scientific Research Communications*, 4(1). <https://doi.org/10.52460/src.2024.003>
- Toğay, O., & White, D. W. (2018, April 10-13). Toward the recognition of unaccounted for flange local buckling and tension flange yielding resistances in the ANSI/AISC 360 specification. In *Proceedings of the Annual Stability Conference* Structural Stability Research Council. Baltimore, Maryland.
- Wang, Y. C., & Nethercot, D. A. (1990). Bracing requirements for laterally unrestrained beams. *Journal of Constructional Steel Research*, 17(4), 305-315. [https://doi.org/10.1016/0143-974X\(90\)90078-U](https://doi.org/10.1016/0143-974X(90)90078-U)
- White, D. W., Jeong, W. Y., & Slein, R. (2021). *AISC Design Guide 25: Frame design using nonprismatic members*. American Institute of Steel Construction.
- Wijaya, P. K., Swan, C. L., & Noor, G. S. (2019). An analysis of elastic and inelastic lateral torsional buckling of web-tapered I beams using the finite element method. *MATEC Web of Conferences*.



Heat and Mass Transfer Model of Horizontal Tubular Absorbers for LiBr/H₂O Absorption Refrigeration

Nuri Kayansayan^{1,*}  Sercan Acarer² 

¹ Dokuz Eylül University (retired), Faculty of Engineering, Department of Mechanical Engineering, İzmir

² İzmir Kâtip Çelebi University, Faculty of Engineering and Architecture, Department of Mechanical Engineering, İzmir

* Corresponding author: sercan.acarer@ikcu.edu.tr

Received: 11.02.2024

Accepted: 13.07.2024

Abstract

This study delves into the absorption efficiency of a horizontal absorber using a LiBr-H₂O solution. We developed a computationally fast and accurate two-dimensional model, which we validated against experimental data. The analysis focuses on key operational parameters such as solution inlet temperature, mass flow rate, and cooling water inlet temperature, revealing their intricate interplay and impact on absorption performance. Our findings highlight the substantial influence of cooling water temperature, showing a significant boost in absorption efficiency as the cooling water temperature decreases. Additionally, we explore the effects of solution mass flow rate, uncovering the delicate balance between increased heat transfer resistance and initial absorption efficiency at near the impingement region. This comprehensive study provides valuable insights into the dynamics of absorption systems, offering pathways to optimize design and operational strategies for enhanced performance.

Keywords: LiBr-H₂O solution; absorption refrigeration; heat and mass transfer, absorber

1. Introduction

Absorption cooling systems use heat as a driving force and are an alternative to conventional gas compression cooling systems. These systems, known for over a century, have gained popularity due to environmental concerns and rising conventional energy costs. They are especially competitive when a cheap heat source like geothermal or solar energy is available (Tsai and Perez-Blanco, 1998).

An absorption cooling cycle uses a working pair, consisting of a refrigerant and an absorbent. Common pairs are LiBr/water and ammonia/water. Ammonia is advantageous due to its lower evaporation temperature, while LiBr's nonvolatility and high vapor affinity offer better absorption performance. However, LiBr's limited solubility can cause crystallization at lower temperatures (Florides et al., 2003).

Absorption refrigerators produce compression effects by absorbing and desorbing refrigerants, rather than compressing gas. Vapors are absorbed at low pressure and desorbed at high pressure using a heat source. Performance can be enhanced through a double-effect absorption cycle, increasing system efficiency (Qu, 2008).

The major components of an absorption cycle are the evaporator, condenser, generator, absorber, and heat exchanger, along with solution and water pumps, and an air purge system. Figure 1 and Figure 2 present the schematic and pressure-temperature diagram of a single-stage absorption cycle, respectively.

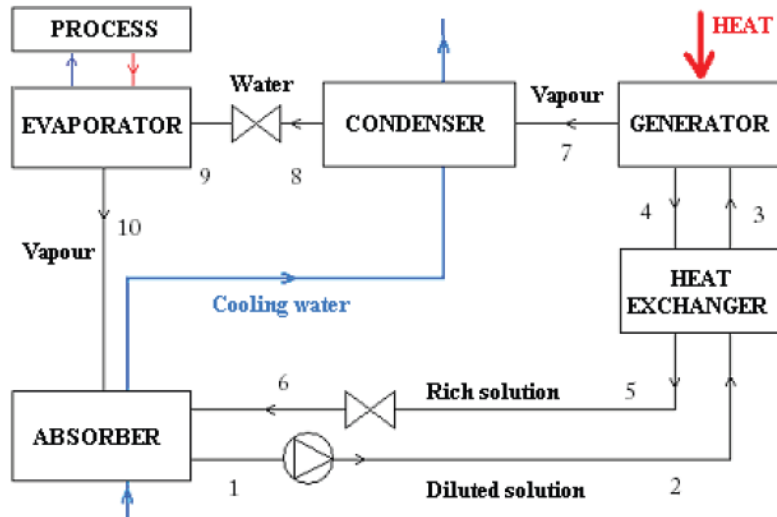


Figure 1. The schematic of a single-stage absorption cycle

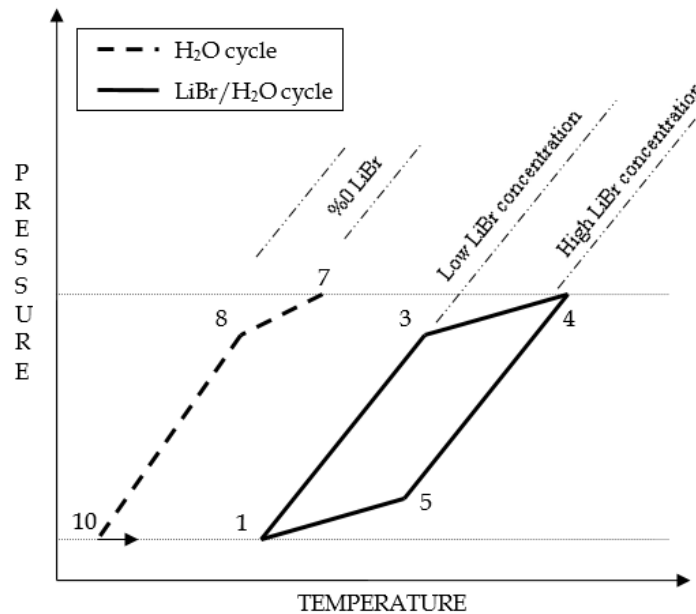


Figure 2. The pressure-temperature diagram of a single-stage absorption cycle

In the absorber, concentrated solution from the generator absorbs vapor, diluting the solution. Despite being central to the system, the absorber is often the least efficient component, making absorption rates a key performance measure (Raisul Islam et al., 2006).

Analytical studies have laid the groundwork for understanding the combined heat and mass transfer processes. Initial efforts, like those by Grigor'eva and Nakoryakov (1977), approached the problem by assuming a steady, smooth laminar film flow on an isothermal surface, simplifying the complex reality. Despite their comprehensive nature, these solutions demanded numerous assumptions, limiting their applicability.

As the limitations of analytical models became evident, particularly their reliance on oversimplified assumptions, the focus shifted towards numerical solutions. These models,

while rooted in the foundational principles laid out by their analytical counterparts, offer a more nuanced and flexible framework, capable of accommodating the irregularities and complexities inherent in real-world scenarios. Description of the problem will be introduced for absorption on a vertical plate, which is the simplest geometry for an absorber, where LiBr/H₂O solution film flows down a vertical cooled plate while the refrigerant supplied from the evaporator is absorbed at the film surface (Figure 3).

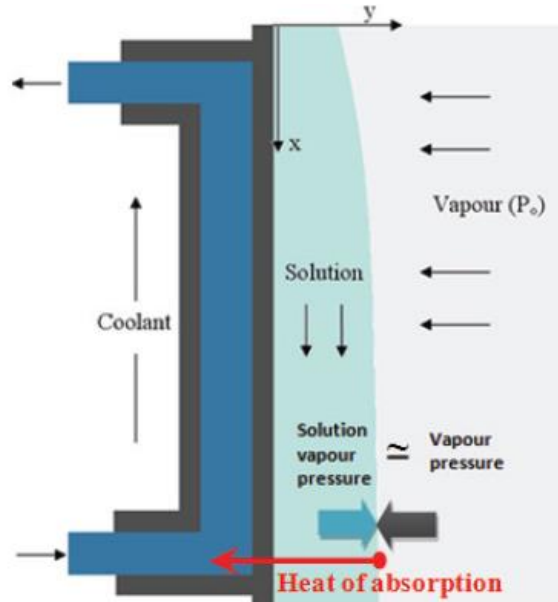


Figure 3. Absorber modeling problem shown on a simple vertical plate case

Andberg and Vliet (1983) and Andberg (1986) pioneered detailed numerical analysis by presenting a comprehensive numerical model, moving beyond the constraints of earlier analytical models. This evolution continued with subsequent studies, each progressively refining the model by integrating factors like film thickness variation, hydrodynamic characteristics, and more realistic boundary conditions.

Since then, many numerous studies have focused on heat and mass transfer modeling within absorbers (Wen et al., 2021; Asfand et al., 2015). These models often employ computational fluid dynamics (CFD) techniques to simulate the complex transport phenomena involved in the absorption process, including fluid mechanics of large droplets (Hosseinnia et al., 2016).

Empirical modeling techniques, known for their capacity to encompass transient behaviors and offer swift predictions for absorbers, have also become increasingly favored, as indicated by Castro et al. (2020). Optimization studies have aimed to improve the efficiency and performance of absorption cooling systems by varying parameters like absorber geometry, heat exchanger design and fluid properties (Sui et al., 2022a, Mortazavi et al., 2015). Numerical simulations coupled with optimization algorithms, such as genetic algorithms, have been employed to find optimal configurations (Sui et al., 2022b).

Numerical models are often validated against experimental data or higher order models to ensure their accuracy (Arroiabe et al., 2022). Researchers have presented case studies involving various absorber designs, operating conditions, and working fluid combinations (Asfand et al., 2016).

As numerical modeling tools continue to advance, the future of absorber modeling in absorption cooling systems may involve the incorporation of artificial intelligence and machine learning techniques for predictive modeling (Alcântara et al., 2023).

The present paper elaborates on the Lithium Bromide (LiBr) and water (H₂O) solution which is dispersed from the top of the horizontal tubes, cascading down a vertically arranged set of tubes. Concurrently, vapor is continuously supplied from an evaporator under vacuum conditions. This flow format manifests as a falling film over the tubes and intermittently as unsteady droplets or elongated strands between tubes. The system is designed such that as the solution absorbs vapor, heat of absorption is generated. This heat must be dissipated into the surroundings via a cooling medium like water or air. Although there are more sophisticated models that include more intricate hydrodynamic models, this study focuses on creating a relatively straightforward and quick predictive model. This model is specifically designed for applications with low Reynolds numbers, where the surface waviness is minimal, and the tube is completely wetted.

2. Numerical Modeling

A solution of LiBr/H₂O is dispersed over the top of the horizontal tubes, cascading down several vertically arranged horizontal tubes is considered. This occurs while a continuous stream of vapor from the evaporator is introduced under a vacuum. The liquid forms a descending film on the tubes, with intermittent droplets or extended trails bridging the tubes. The absorption of vapor by the solution triggers the production of absorption heat, which needs to be dispersed into the surrounding air or water.

In modeling the absorber, a two-dimensional slice of the film flow is segmented into distinct, non-overlapping Eulerian control volumes. The film's thickness changes along the flow direction, necessitating the creation of a body-fitted mesh (Figure 4).

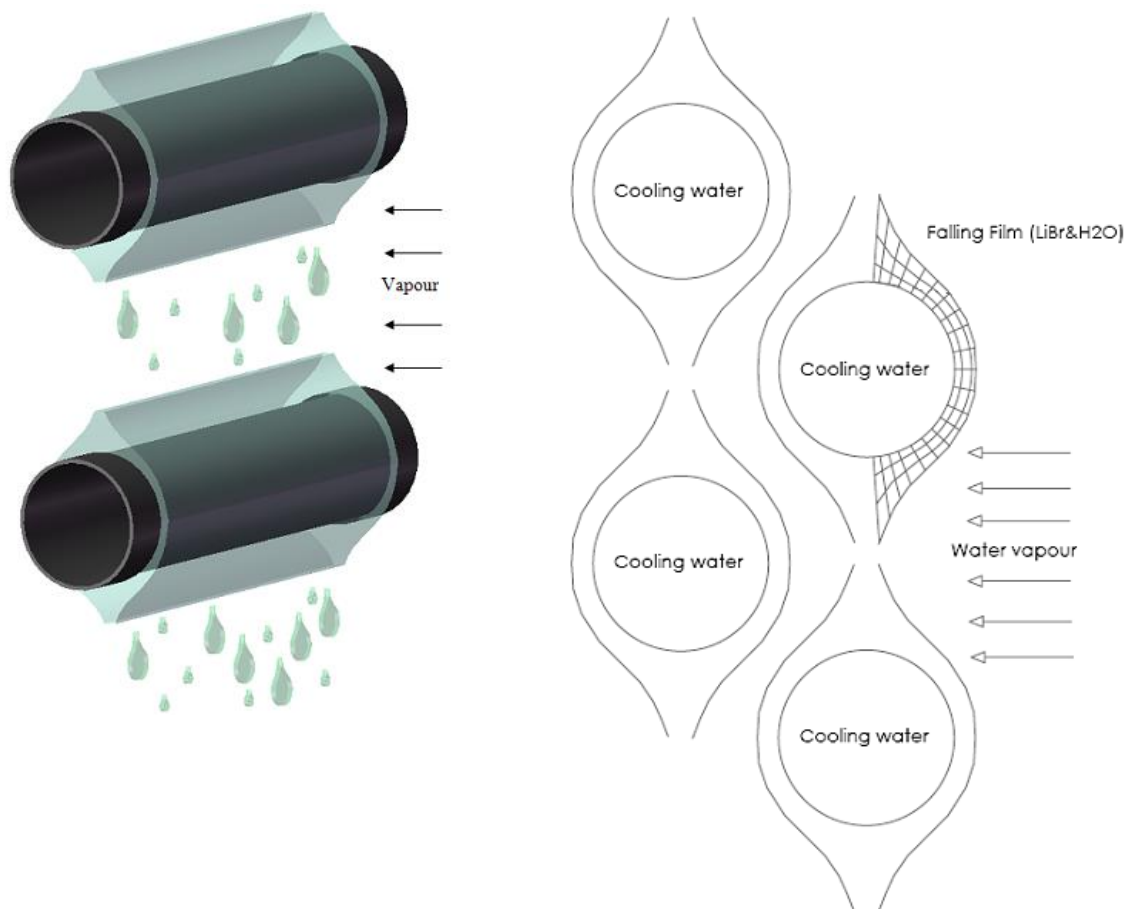


Figure 4. Horizontal absorber modeling

A coordinate transformation reconfigures the physical domain into a rectangular shape to streamline programming. The basic definition for the coordinate system and velocity components is shown in Figure 5.

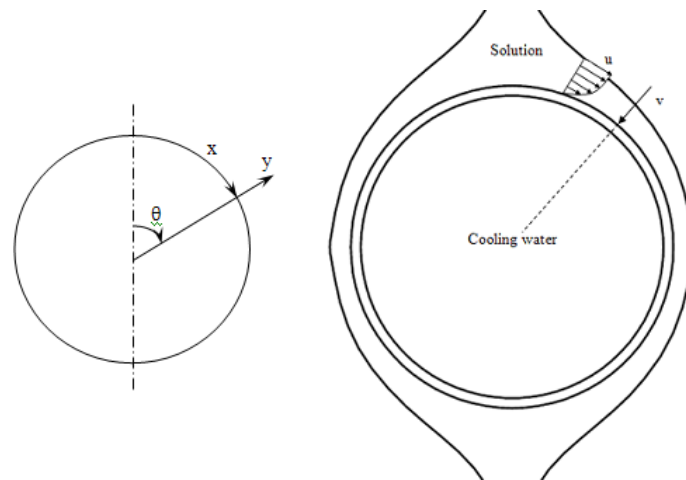


Figure 5. The coordinate system and velocity definitions

The model's characteristics include:

- Local variations in physical properties with temperature and concentration, though these variations are disregarded within each differential control volume.
- An increase in mass flow rate due to vapor absorption into the liquid film, leading to a change in film thickness across successive tubes.

The modeling is based on the following assumptions:

- The solution uniformly coats the tube.
- A balance in vapor pressure is maintained at the interface between the vapor and the solution.
- The flow is consistently laminar and smooth.
- Heat transfer is primarily in the solution, not the vapor phase, meaning all interface-generated heat is absorbed by the solution.
- The vapor exerts no shear stress on the film flow.
- Diffusion along the flow direction is considered insignificant.

The velocity profile of the film can be determined using the Navier-Stokes Equations. Given that the film's thickness is significantly smaller than the radius of the tube, it's practical to apply a Cartesian coordinate system for the film flow. In this scenario, viscous forces are the primary concern, allowing the neglect of inertial forces. It's also presumed that the pressure within the film remains uniform and that gravity serves as the primary force driving the flow.

Under these conditions, the steady-state Navier-Stokes Equation, oriented along the flow direction (as indicated by the x-axis in Figure 5), simplifies considerably:

$$\mu_s \frac{\partial^2 u}{\partial y^2} = -\rho_s g \sin \theta \tag{1}$$

Operating under the assumption that the vapor imparts no shear stress on the film, the velocity profile along the flow direction (represented by 'u' in Figure 5) can be deduced as follows:

$$u(x, y) = \frac{\rho_s g \delta^2}{2\mu_s} \sin \theta \left(2 \frac{y}{\delta} - \left(\frac{y}{\delta} \right)^2 \right) \tag{2}$$

The velocity profile across the transverse direction (represented by 'v' in Figure 5) can be established based on the principle of continuity:

$$v(x, y) = -\frac{\rho_s g}{2\mu_s} y^2 \left[\frac{d\delta}{dx} \sin \theta + \frac{1}{r_o} \left(\delta - \frac{y}{3} \right) \cos \theta \right] \quad (3)$$

Local film thickness can be derived from u-velocity for a known solution mass flow rate:

$$\delta(\theta) = \left(\frac{3\mu_s \Gamma_s}{\rho_s^2 g \sin \theta} \right)^{1/3} \quad (4)$$

Where Γ_s is the solution mass flow rate per length and side of tube ($\Gamma_s = \dot{m}_s / 2L$) and ρ_s denotes solution density.

The steady-state energy balance for a differential control volume can be articulated using Cartesian coordinates, given that the usual measurements of film thickness are quite minor relative to the tube's diameter:

$$\frac{\partial(uT)}{\partial x} + \frac{\partial(vT)}{\partial y} = \alpha_s \frac{\partial^2 T}{\partial y^2} \quad (5)$$

The steady-state species balance for a differential control volume can be articulated in a similar manner as:

$$\frac{\partial(uC)}{\partial x} + \frac{\partial(vC)}{\partial y} = D \frac{\partial^2 C}{\partial y^2} \quad (6)$$

The flow rate of the solution film is significantly less than the cooling water's flow rate. As a result, the heat capacity of the cooling water is much greater than the solution's heat capacity. The combination of this, and the relatively brief length of the tube, results in the cooling water experiencing a much smaller increase in temperature compared to the solution. It can be concluded from a previous investigation (Papaefthimiou et al. 2006) that the temperature increase of the cooling water is linear in the axial direction of the tube. Hence cooling water temperature can be calculated at the half length of each tube, and this will represent the mean cooling water temperature for the tube. Heat transfer coefficient in the cooling water side is calculated from $Nu_b = 0.023 Re_b^{0.8} Pr_b^{0.4} (\mu_b / \mu_w)^{0.262}$ correlation which is valid for incompressible turbulent flow flowing inside a pipe (Kakaç and Liu, 1998).

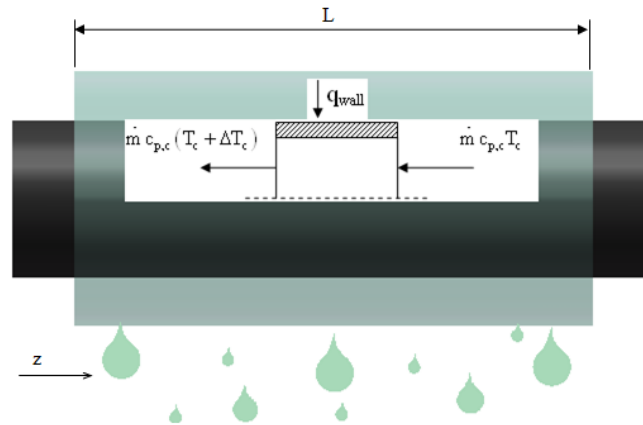


Figure 6. A one-dimensional differential control volume pertaining to the flow of cooling water within the tube

Cooling water temperature gradient expression for the cooling water can be derived from the one-dimensional energy balance shown in Figure 6 for the cooling arrangement presented in Figure 7:

$$\frac{dT_c}{dz} = \frac{(2\pi r_o) q_{\text{wall-average}}}{m_c c_{p,c}} \tag{7}$$

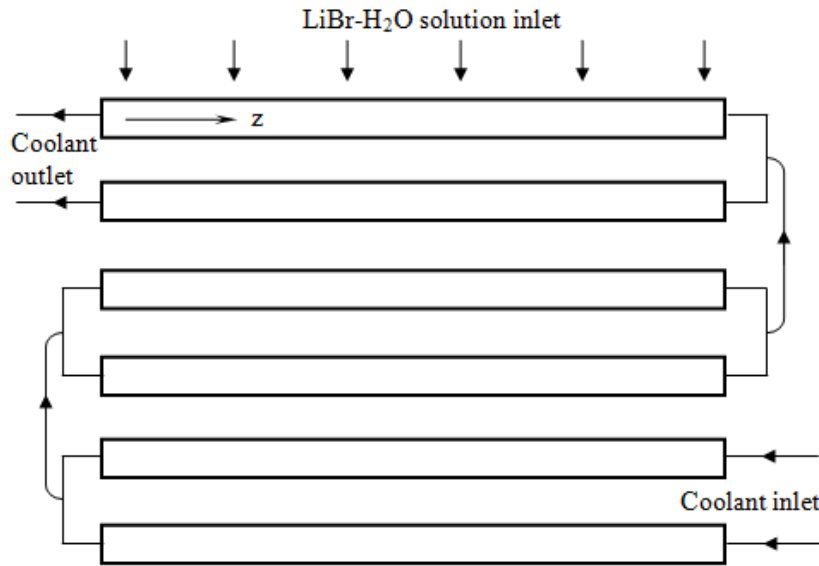


Figure 7. Tubes and the cooling water arrangement

Because the problem is a steady spatial marching problem, the calculation procedure must start from solution inlet, hence the boundary conditions at the inlet are categorized under “initial conditions”. Initial conditions for the LiBr-H₂O solution at the inlet (Figure 8) are:

$$\left. \begin{matrix} x = x_{in} \\ 0 \leq y \leq \delta(x) \end{matrix} \right\} \begin{matrix} T = T_{in} \\ C = C_{in} \end{matrix} \tag{8}$$

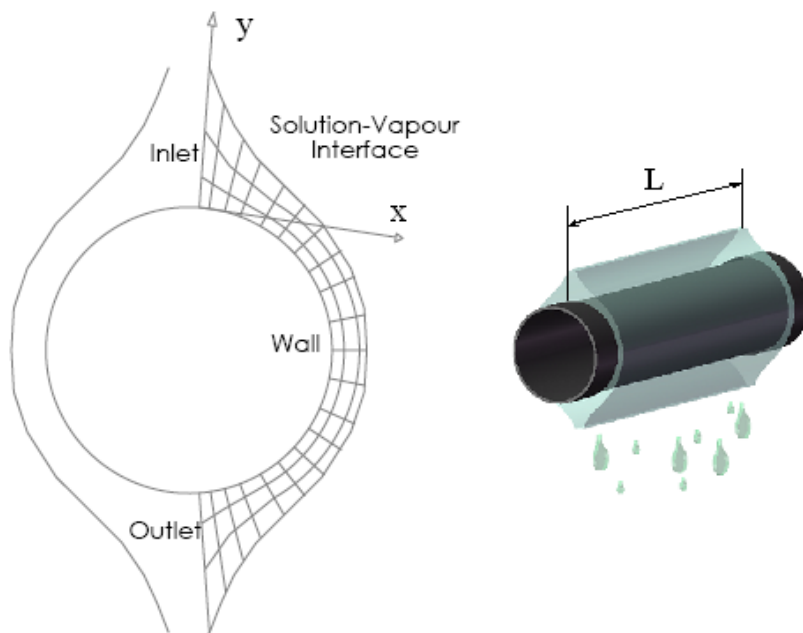


Figure 8. Edges of the physical area (left) and illustration of the tube's length (right)

The boundary conditions for the LiBr-H₂O solution are as follows:

At the tube surface:

$$\left. \begin{array}{l} y = 0 \\ x_{in} \leq x \leq x_{out} \end{array} \right\} \begin{array}{l} U(T - T_c) = k_s \frac{\partial T}{\partial y} \\ \frac{\partial C}{\partial y} = 0 \end{array} \quad (9)$$

U is the overall heat transfer coefficient calculated at the outer surface of the tube.

At the solution-vapour interface:

$$\left. \begin{array}{l} y = \delta(x) \\ x_{in} \leq x \leq x_{out} \end{array} \right\}$$

Mass flux is calculated from Fick's first law:

$$\dot{m}_{H_2O} = -\rho_s D \frac{1}{C_{if}} \frac{\partial C}{\partial y} \quad (10)$$

Vapour pressure equilibrium condition function is:

$$T_{if} = f(p, C_{if}) \quad (11)$$

Heat generation at the interface can be expressed as the product of mass absorption rate and heat of absorption per unit mass flow rate:

$$q_{if} = h_{abs} \dot{m}_{H_2O} \quad (12)$$

And heat of absorption is transferred into the solution:

$$q_{if} = -k_s \frac{\partial T}{\partial y} \quad (13)$$

At the exit, the temperature and concentration gradients along the flow direction are established as zero.

2.1. Coordinate Transformation

Because the film thickness changes with the circumferential (x) position (see Figure 5), a coordinate transformation process is needed in order to convert the complex domain into a non-dimensional square domain (see Figure 9), hence derivatives are normalized. This generally increases complexity of the governing equations, however simplifies the code considerably. Hence, we are considering the following non-dimensional variables:

$$X = \frac{\theta}{\pi} = \frac{x}{\pi r_o} \quad (14)$$

$$Y = \frac{y}{\delta(x)} \quad (15)$$

$$Z = \frac{z}{L} \tag{16}$$

Since Nusselt's solution results in an infinite film thickness at the top and bottom of the tube, the value of Y becomes unbounded at these extreme points. Therefore, to avoid this issue, areas near X=0 and X=1 are excluded from the domain of the solution.

By substituting Eqs. 14-16 into governing equations; Film thickness expression (Eq. 4) becomes:

$$\delta(\theta) = \left(\frac{3\mu_s \Gamma_s}{\rho_s^2 g \sin(\pi X)} \right)^{1/3} \tag{17}$$

Where Γ_s is the solution mass flow rate per length and side of tube ($\Gamma_s = \dot{m}_s / 2L$) and ρ_s denotes solution density.

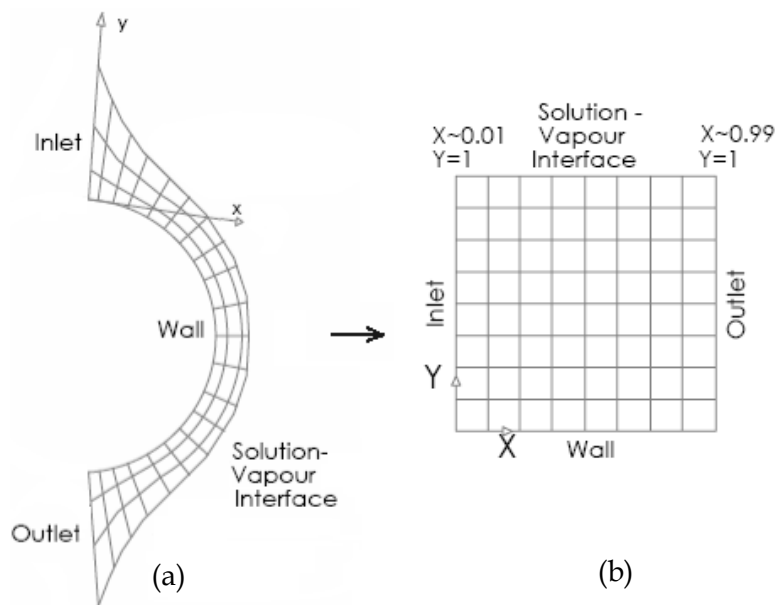


Figure 9. a) The area used for computation, b) The adjusted area designated for computation
The velocity profiles (Eqs.2,3) become:

$$u(X, Y) = \frac{\rho_s g \delta^2}{2\mu_s} \sin(\pi X) (2Y - Y^2) \tag{18}$$

$$v(X, Y) = -\frac{\rho_s g}{2\mu_s} Y^2 \delta^2 \frac{1}{r_0} \left[\frac{1}{\pi} \frac{d\delta}{dX} \sin(\pi X) + \delta \left(1 - \frac{Y}{3} \right) \cos(\pi X) \right] \tag{19}$$

The solution Reynolds, Prandtl and Schmidt numbers are defined as (respectively):

$$Re_s = \frac{4\Gamma_s}{\mu_s} \tag{20}$$

$$Pr_s = \frac{\mu_s c_{ps}}{k_s} \tag{21}$$

$$Sc_s = \frac{\mu_s}{\rho_s D} \tag{22}$$

Then, energy equation (Eq.5) becomes:

$$\frac{\partial T}{\partial X} - \left[\frac{v}{u} \frac{\pi r_0}{\delta} - \frac{Y}{\delta} \frac{d\delta}{dX} \right] \frac{\partial T}{\partial Y} - \left[\frac{8}{3} \frac{1}{Pr_s} \frac{\pi r_0}{\delta_{90}} \frac{\sin(\pi X)^{1/3}}{Re_s (2Y - Y^2)} \right] \frac{\partial^2 T}{\partial Y^2} = 0 \tag{23}$$

Species transport equation (Eq.6) becomes:

$$\frac{\partial C}{\partial X} - \left[\frac{v}{u} \frac{\pi r_0}{\delta} - \frac{Y}{\delta} \frac{d\delta}{dX} \right] \frac{\partial C}{\partial Y} - \left[\frac{8}{3} \frac{1}{Sc_s} \frac{\pi r_0}{\delta_{90}} \frac{\sin(\pi X)^{1/3}}{Re_s (2Y - Y^2)} \right] \frac{\partial^2 C}{\partial Y^2} = 0 \tag{24}$$

In Eq.23 and 24, δ_{90} is the film thickness at the middle of the tube ($X=0.5$).

The boundary conditions of the transformed governing equations (Equations 23 and 24) are deduced from the boundary conditions of the original governing equations in the following manner:

At the inlet (see Figure 9):

$$\left. \begin{aligned} X = X_{in} \\ 0 \leq Y \leq 1 \end{aligned} \right\} \begin{aligned} T &= T_{in} \\ C &= C_{in} \end{aligned} \tag{25}$$

At the tube wall:

$$\left. \begin{aligned} Y = 0 \\ X_{in} \leq X \leq X_{out} \end{aligned} \right\} \begin{aligned} T_{wall} &= T_c + \left(\frac{k_s}{\delta_{mean} U} \right) \frac{\partial T}{\partial Y} \\ \frac{\partial C}{\partial Y} &= 0 \end{aligned} \tag{26}$$

The term $k_s / (\delta_{mean} U)$, is named as "CW".

At the solution-vapor interface:

$$\left. \begin{aligned} Y = 1 \\ X_{in} \leq X \leq X_{out} \end{aligned} \right\}$$

Heat of absorption is transferred into the solution:

$$\frac{\partial T}{\partial Y} = - \frac{\rho_s Dh_{abs}}{k_s} \frac{1}{C_{if}} \frac{\partial C}{\partial Y} \tag{27}$$

Vapor pressure equilibrium condition:

$$T_{if} = f(p, C_{if}) \tag{28}$$

At the outlet, gradients of temperature and concentration with respect to X are set to zero.

2.2. Deriving the Discretization Equations

The discretization equations are obtained using the control volume method. By assuming constant values of Y , $\delta(X)$, u , and v within a control volume, the transformed governing equations (Equations 23 and 24) are each integrated over a control volume:

$$\frac{\Delta Y}{\Delta X} (T_e - T_w) - \left[\frac{v \pi r_o}{u \delta} - \frac{Y}{\delta} \frac{d\delta}{dX} \right] (T_n - T_s) - \left[\frac{8}{3} \frac{1}{Pr_s} \frac{\pi r_o}{\delta} \frac{\sin(\pi X)^{1/3}}{Re_s (2Y - Y^2)} \right] \frac{\partial T}{\partial Y} \Big|_s = 0 \tag{29}$$

$$\frac{\Delta Y}{\Delta X} (C_e - C_w) - \left[\frac{v \pi r_o}{u \delta} - \frac{Y}{\delta} \frac{d\delta}{dX} \right] (C_n - C_s) - \left[\frac{8}{3} \frac{1}{Sc_s} \frac{\pi r_o}{\delta} \frac{\sin(\pi X)^{1/3}}{Re_s (2Y - Y^2)} \right] \frac{\partial C}{\partial Y} \Big|_s = 0 \tag{30}$$

Definitions of w , e , n , s , W , E , N and S points are illustrated in Figure 10.

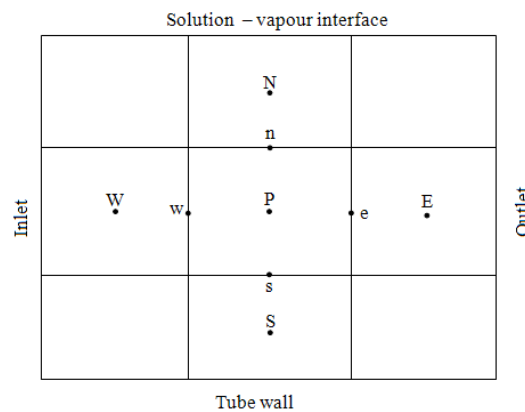


Figure 10. Illustrative diagram depicting the layout of the grid, along with explanations for the positions of the west, east, south, and north nodes, as well as the control surfaces

Cooling water energy balance becomes:

$$\frac{dT_c}{dZ} = - \left(\frac{(2\pi r_o) L k_s}{m_c c_{p,c} \delta_{mean}} \right) \frac{\partial T}{\partial Y} \Big|_{mean} \tag{31}$$

2.3. The Solution Method

In the transverse (y) direction, where the velocity is minimal and diffusion dominates, the upwind scheme is unsuitable, so the central differencing scheme is employed instead. In contrast, the downstream direction utilizes the upwind scheme (Patankar, 1980). The derivatives in Equations 29 and 30 for the inner nodes are calculated using the central difference formulation.

While the inlet temperature of the cooling water is known for the final tube in a counter-flow setup, the calculation begins with the first tube, necessitating an initial estimation of the outlet temperature of the cooling water. To accurately trace the decrease in cooling water temperature, it's crucial to solve a series of two-dimensional sections in sequence, adding a three-dimensional element to the solution. However, to manage the computational load, the

process is simplified by selecting only three axial positions, based on the premise of a linear reduction in cooling water temperature. Temperatures of the cooling water are recorded at the midpoint and end of each tube, respecting the counter-flow heat exchanger pattern where cooling water enters at the tube's end. The temperature at the tube's midpoint is taken as the average for that tube, while the temperature at the end is used as the exit temperature for the next tube in the sequence. A flowchart detailing the steps of this algorithm is shown in Figure 11.

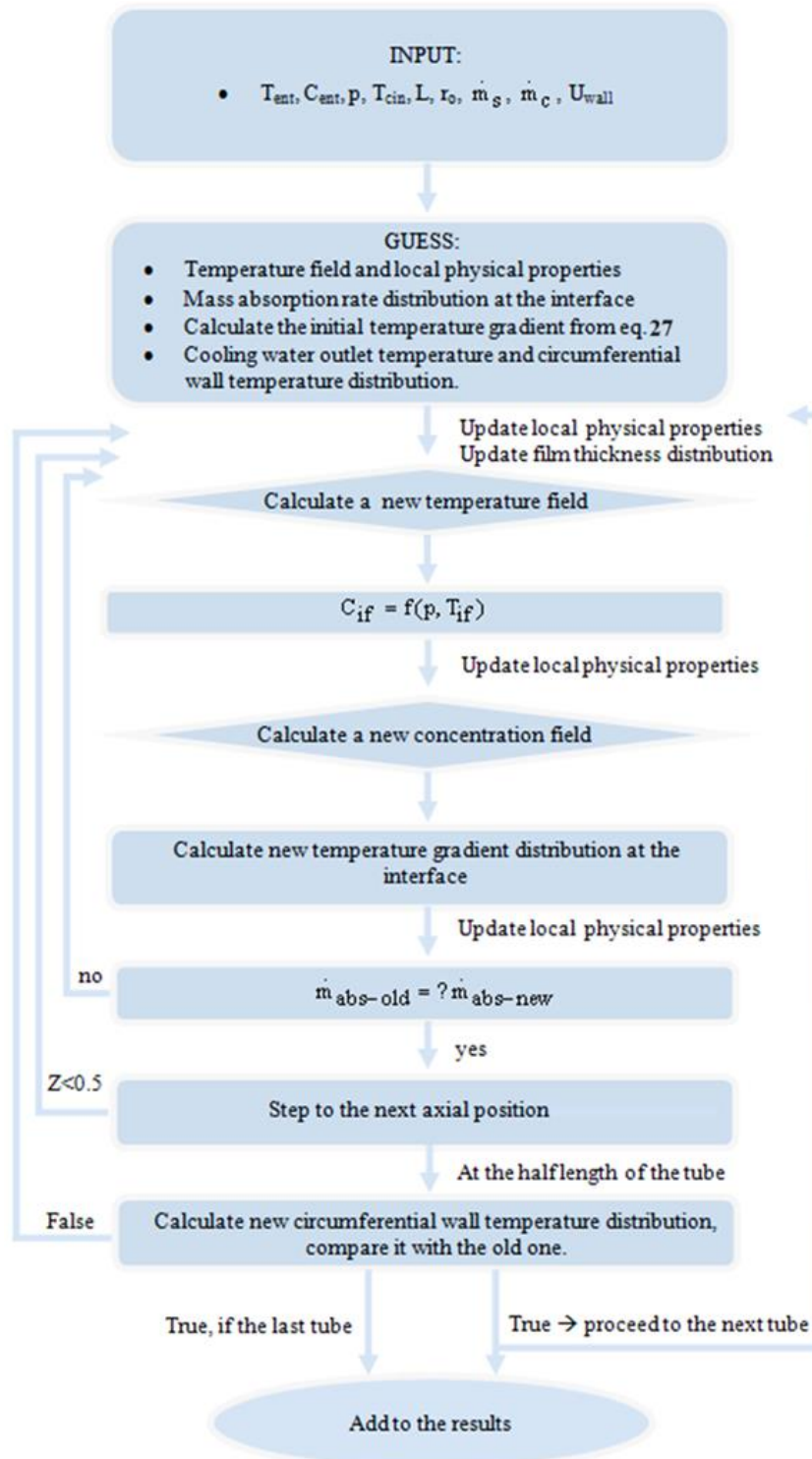


Figure 11. Diagram illustrating the sequence of steps in the algorithm for the horizontal absorber model

3. Results

This section outlines the findings obtained under various scenarios, including changes in vapor pressure, temperatures at the inlet and concentrations of the solution, cooling water's inlet temperature, mass flow rates, and the configuration of the tubes. These findings are compared with experimental data from prior studies to establish the limits of the current model's validity.

The distribution and average of vapor absorption flux are identified as the primary indicators of performance. Considering that the thickness of the film is affected by the film's Reynolds number and certain material characteristics, the patterns of mass (and thermal) flux are relevant to any system that matches the dimensionless figures inputted into the software.

The report includes charts showing how heat flux is distributed on the film's surface and along the wall. These factors are vital as mass transfer is closely associated with thermal transfer. Fundamentally, mass transfer can only proceed if the heat produced during absorption is efficiently transferred from the interface to the cooling water.

The physical properties of LiBr-H₂O are compiled from multiple sources. Curve fits of experimental data for properties such as density, heat capacity, dynamic viscosity, and thermal conductivity are sourced from Kwang (1992):

$$\rho_s = 1000 \times ((0.7086 + 1.691 \times C) - 0.0005 \times T) \quad [\text{kg} / \text{m}^3] \quad (32)$$

$$c_{ps} = 1000 \times 19.458 \times T^{0.05} \times (100 \times C)^{-0.609} \quad [\text{J} / \text{kgK}] \quad (33)$$

$$k_s = 1.163 \times (0.4945 + 0.002052 \times T - 0.000015 \times T^2 - 0.31 \times C) \quad [\text{W} / \text{m}^2\text{K}] \quad (34)$$

$$\mu_s = (1 + 0.686602333 \times e^{(0.107 \times 100 \times C)} \times T^{-1.238}) / 1000 \quad [\text{Ns} / \text{m}^2] \quad (35)$$

The curve fitting for the heat of absorption, originally formulated by Andberg (1986), has been revised to conform with the more accurate data presented by Papaefthimiou et al. (2006):

$$h_{abs} = 2.5124 \times 10^6 - (283.3 + 1177 \times T) + 20152 \times (1660.47 * C^7 - 2550 \times C^8 + 1410.1 \times C^9) \quad [\text{J/kgK}] \quad (36)$$

The surface pressure equilibrium function ($C_{if} = f(p, T_{if})$), as sourced from Raisul Islam et al. (2006), is adopted and linearized:

$$C_{if} = (4.8688 \times 10^{-3} \times p^{-0.188}) T_{if} + 0.37794 \quad (37)$$

Diffusivity is assumed to be constant:

$$D = 1.52 \times 10^{-9} \quad [\text{m}^2 / \text{s}] \quad (38)$$

The local interfacial mass flux may be obtained by the expression:

$$\dot{m}(X) = \rho D \frac{1}{C} \left. \frac{\partial C}{\partial X} \right|_{Y=1} \quad [\text{kg} / \text{m}^2\text{s}] \quad (39)$$

Where $\delta(X) = (0.75 \text{ Re } v_s^2 / g / \sin(\pi X))^{1/3}$ is the film thickness evaluated at the local bulk conditions at any circumferential position. It is important to note that it exclusively relies on

the local Reynolds number, temperature, and concentration (therefore, impacting the solution's viscosity and density). Consequently, the distribution of mass flux can be assessed for the partially nondimensional system, as previously mentioned.

Overall interfacial mass flux can be evaluated by directly averaging local mass fluxes:

$$\dot{m}_{\text{mean}} = \frac{\sum_{X_{\text{in}}}^{X_{\text{out}}} \dot{m}(X)}{n} \tag{40}$$

Where n is the number of cells in the downstream (x) direction.

Bulk temperature (T_b) and concentration (C_b) may be calculated as follows:

$$T_b = \frac{\sum_{\text{tube wall}}^{\text{filmsurface}} uT}{u_{\text{mean}}} \tag{41}$$

$$C_b = \frac{\sum_{\text{tube wall}}^{\text{filmsurface}} uC}{u_{\text{mean}}} \tag{42}$$

Where 'u' is the velocity component in the downstream direction.

3.1. Experimental Validation

The model's accuracy was validated using the experimental data from Seol and Lee (2005). As indicated in Figure 12, the model shows a good match for sheet flow drainage conditions.

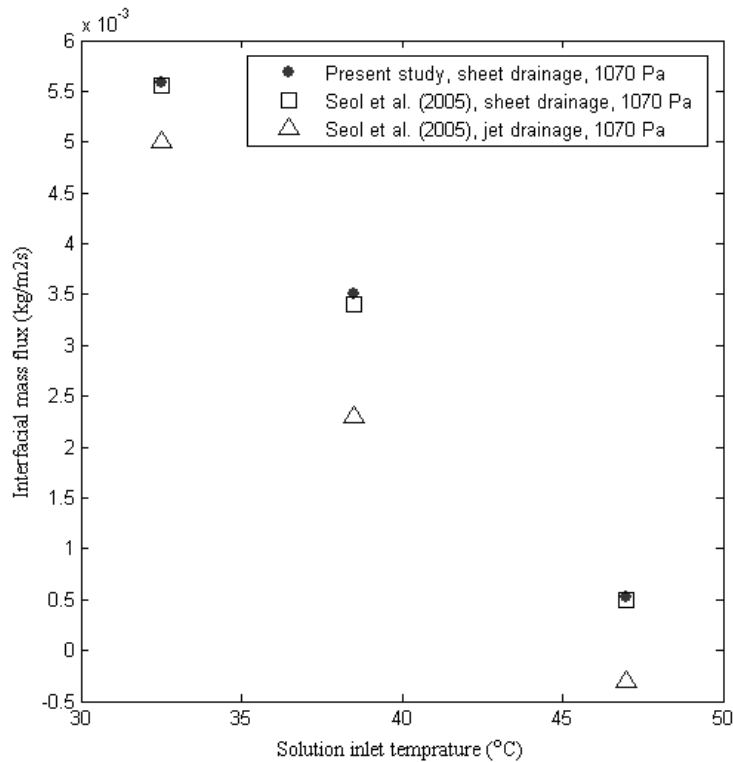


Figure 12. Variation of average mass flux with solution inlet temperature, comparing the present horizontal absorber model with experimental data of Seol and Lee (2005)

Typically, the solution drips in unsteady droplets or jets between tubes, but by placing a thin plate just beneath a tube, sheet drainage is deliberately formed. This arrangement ensures a uniform film flow on the tube surface, thereby enhancing performance at the specified mass flow rate. However, the current model falls short in predicting outcomes for jet drainage, as this form of drainage leads to time-dependent and unevenly distributed flow on the tube surface. Accurately modeling these effects would require a more complex, time-dependent, three-dimensional hydrodynamic model. Nonetheless, because performance improves with sheet drainage, the inability to model jet drainage is not always a significant drawback.

3.2. Parameter Space Being Investigated

The structural design of the horizontal absorber in question involves a solitary copper tube with external and internal diameters measuring 19.05 mm and 16.6 mm respectively, and a length of 0.5 m. The LiBr/H₂O mixture is introduced at the top of the tube, flowing downward as a sheet. This sheet flow assumption is deemed realistic for the inner tubes (excluding the topmost tube) and can be achieved by installing a slim vertical plate just beneath the tube being tested, as suggested by Seol and Lee (2005). Typically, the solution cascades down in an irregular pattern of jet flows and droplets between the tubes.

A summary of the operational parameters is provided in Table 1, and the dimensionless inputs used in the developed code are detailed in Table 2.

Table 1. Physical parameters which satisfy the dimensionless inputs

	High solution inlet temperature	Low solution inlet temperature
T_{si}	46 °C	31 °C
C_{si}		0.6 (wt LiBr)
m_{si}		0.00724 kg/s
$\delta_{90i} = f(m_{si})$	0.15 mm	0.175 mm
p		1250 Pa
r_o		9.525 mm
r_i		8.3 mm
L		0.5 m
T_{ci}		30 °C
m_c		0.43 kg/s

Table 2. Program inputs at the inlet conditions

	High solution inlet temperature	Low solution inlet temperature
T_{si}	46 °C	31 °C
C_{si}		0.6 (wt LiBr)
p		1250 Pa
Re_s	6.186	4.137
Pr_s	21.13	32.146
Sc_s	1812.68	2699
$\mu r_o / \delta_{90i}$	195.415	171.38

3.3. Results for High Temperature Solution Inlet

Figure 13 and Figure 14 shows the temperature and concentration, respectively. The initial rise of temperature and subsequent cooling is evident from Figure 13. Figure 14 shows how vapor is absorbed and diffused and convected into the domain. Since the temperature profile is initially uniform (in the transverse direction) near the impingement point at the top (may be

called as the “inlet”), the absorption heat generated at the film's surface does not being transferred to the cooling water (See the flat profile in Figure 15), which restricts absorption efficiency. Yet, the tube wall is significantly cooler than the bulk of the solution, and the heat from absorption at the interface marginally raises the surface temperature. Consequently, just past the top impingement point (at $X=0.002$ and $X=0.01$), very high temperature gradients appear at the wall and film surface. The high temperature on the wall is responsible for rapid temperature drop at this position. On the interface, the high temperature gradient does not cause streamwise temperature drop since heat of absorption increases the surface temperature.

The corresponding concentration profile is shown in Figure 16. As the temperature profile evolves in the streamwise (X) direction, enabling heat transfer from the film's surface to the cooling water (Y direction), the absorption rate markedly increases. As vapor is absorbed in substantial amounts, the vapor concentration both at the surface and overall begins to rise, which reduces the absorption driving force (see Figure 14). The intense temperature gradients near the impingement point (“inlet” or “the top of the tube”) result from substantial concentration gradients at the film surface (see $X=0.002$ and $X=0.01$), leading to extremely high absorption rates at the entrance (observe $X<0.01$). Consequently, the heat released from absorption prevents the drop of surface temperature. Near the impingement point, concentration gradients are high due to the elevated LiBr concentration near the surface, thus enhancing the absorption driving force.

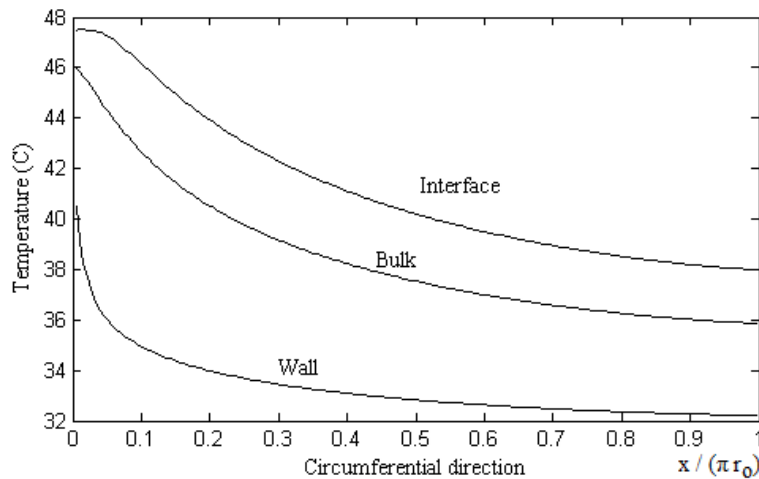


Figure 13. Variation of surface, wall and bulk temperature with distance around the tube, high temperature inlet (see Figure 9 for the definition of the domain)

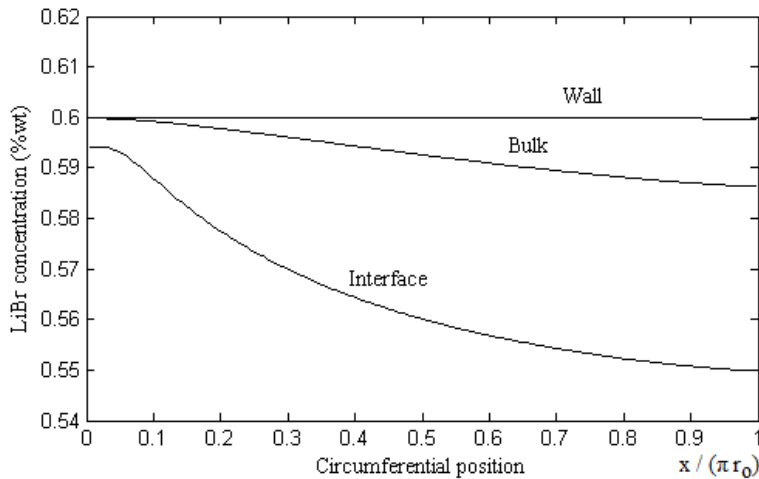


Figure 14. Variation of surface, wall and bulk LiBr concentration with distance around the tube, high temperature inlet (see Figure 9 for the definition of the domain)

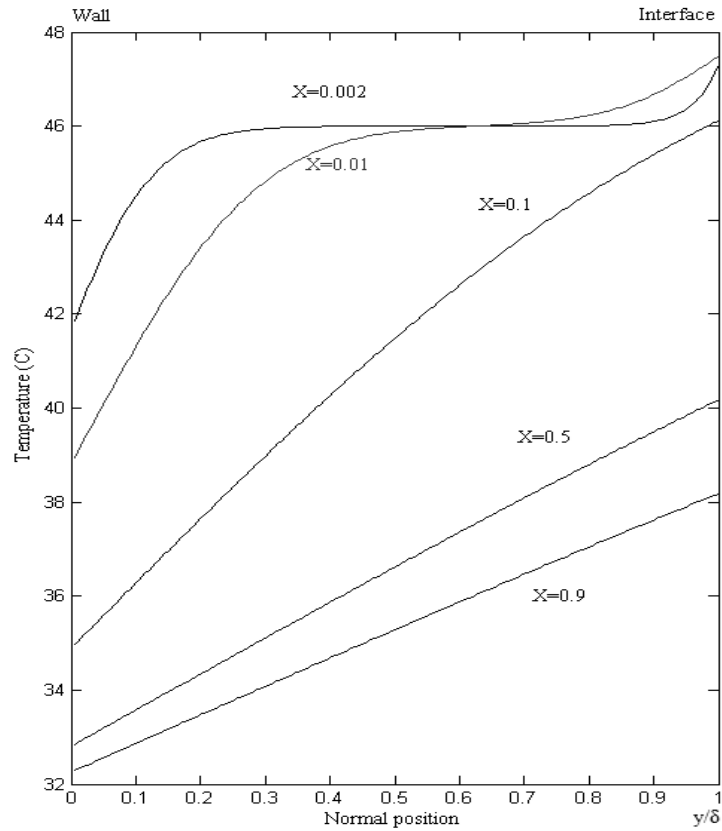


Figure 15. Cross stream temperature profiles at selected downstream positions, high temperature inlet (see Figure 9 for the definition of the domain)

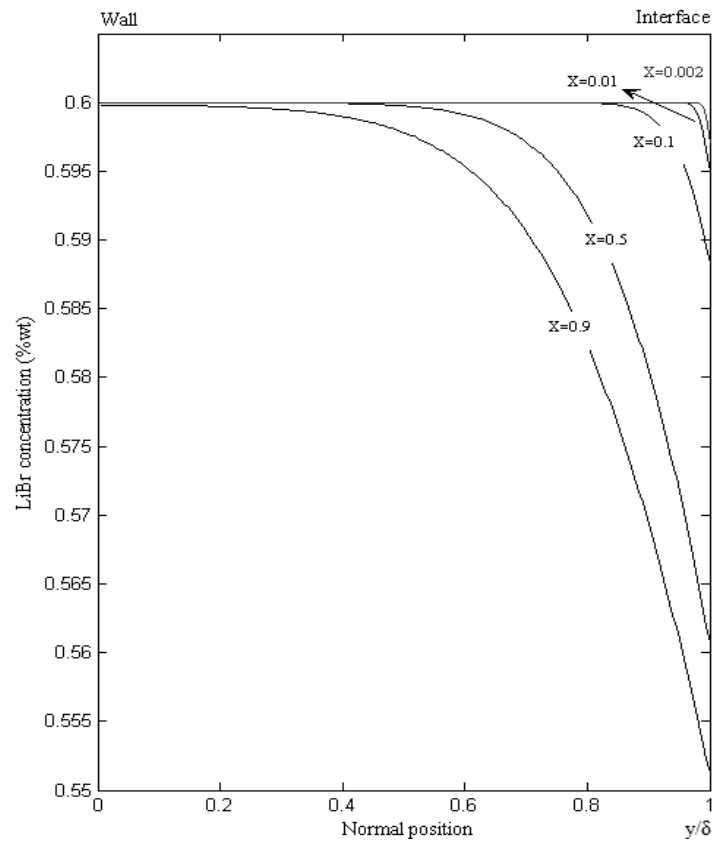


Figure 16. Cross stream LiBr concentration profiles at selected downstream positions, high temperature inlet (see Figure 9 for the definition of the domain)

Following the tube's 40% circumference ($X > 0.4$, Figure 9) (refer to Figure 17), absorption rates begin to decrease gradually. This is mostly attributed to increased film thickness. Similarly, as the solution progresses towards the tube's end, the film thickens, which in turn heightens resistance to both heat and mass transfer (illustrated in Figure 18). Another reason is that since the vapor is absorbed in substantial amounts, the vapor concentration both at the surface and overall begins to rise, which reduces the absorption driving force (see Figure 14).

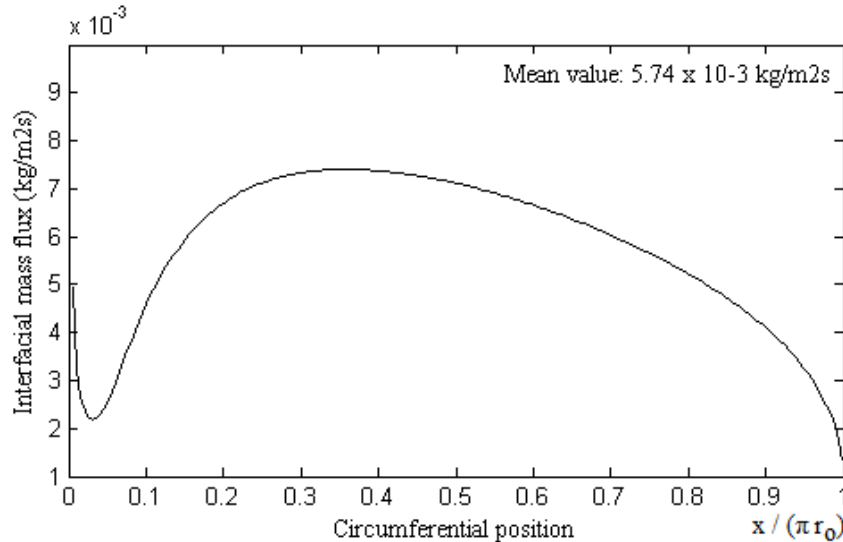


Figure 17. Variation of interface vapour absorption flux with distance around the tube, high temperature inlet (see Figure 9 for the definition of the domain)

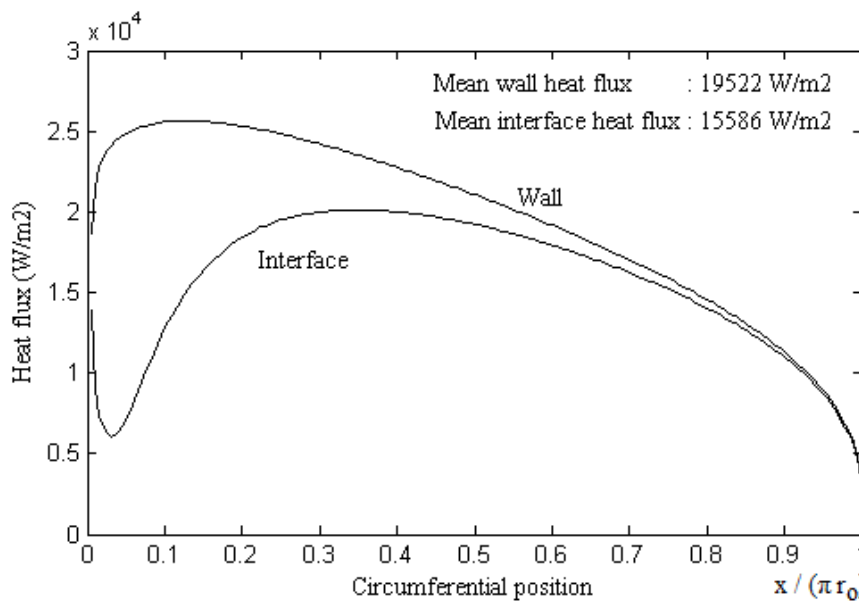


Figure 18. Variation of surface and wall heat flux with distance around the tube, high temperature inlet (see Figure 9 for the definition of the domain)

3.4. Results for Low Temperature Solution Inlet

Due to the notably low temperature at the inlet, there is a significant absorption activity aimed at equalizing the solution's vapor pressure with the absorber pressure. This leads to an increase in both bulk and surface temperatures, as depicted in Figure 19 until $X \sim 0.2$ (see Figure 9 for the definitions). After that circumferential position, interface, bulk and wall temperatures gradually reduces as a result of increased cooling.

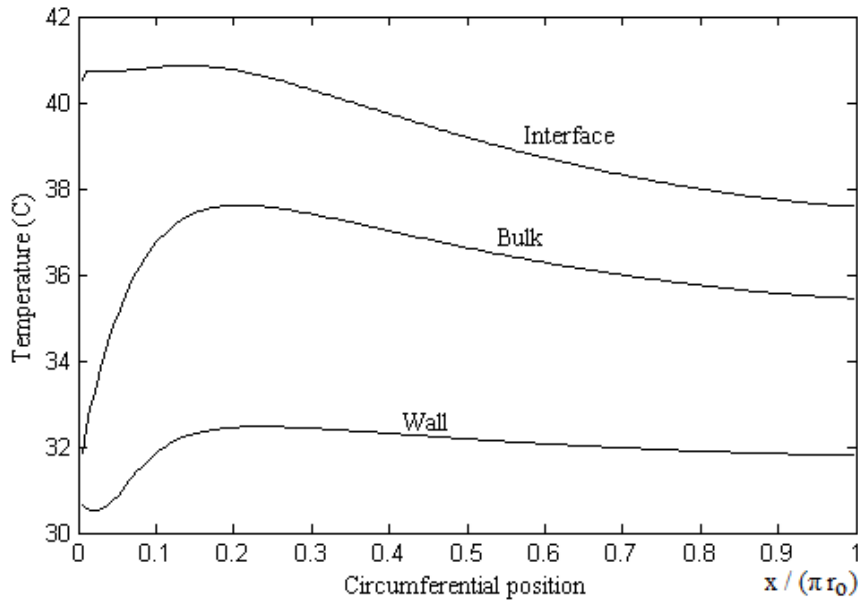


Figure 19. Variation of surface, wall and bulk temperature with distance around the tube, low temperature inlet (see Figure 9 for the definition of the domain)

However, since the temperature profile remains uniform in the transverse direction at the inlet, as shown in Figure 21, the absorption heat does not transfer to the cooling water. Figure 20 illustrates the variation of surface, wall, and bulk LiBr concentration with distance around the tube. In Figure 22, a more detailed presentation of this data in the transverse direction showcases the precise distribution of LiBr concentration, with convection and diffusion of the vapor smoothly captured.

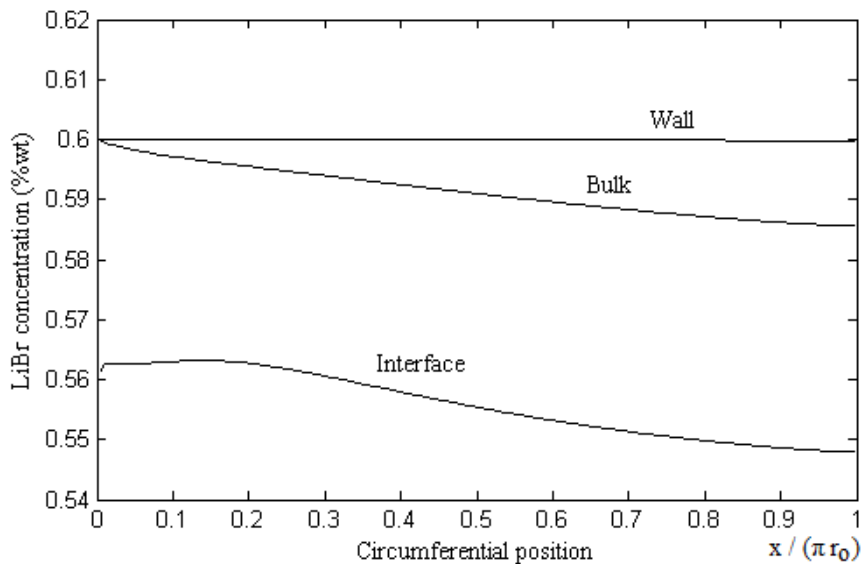


Figure 20. Variation of surface, wall and bulk LiBr concentration with distance around the tube, low temperature inlet (see Figure 9 for the definition of the domain)

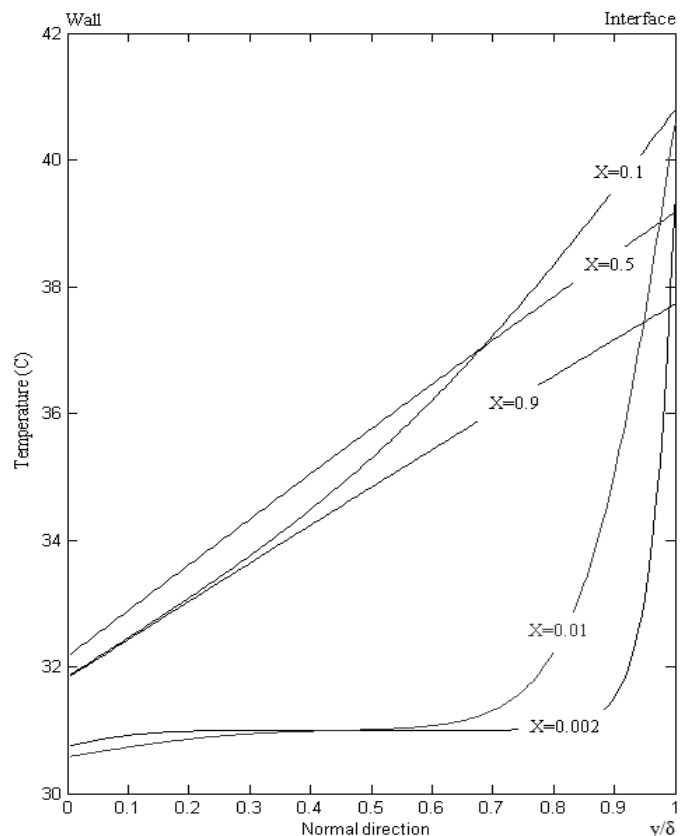


Figure 21. Cross stream temperature profiles at selected downstream positions, low temperature inlet (see Figure 9 for the definition of the domain)

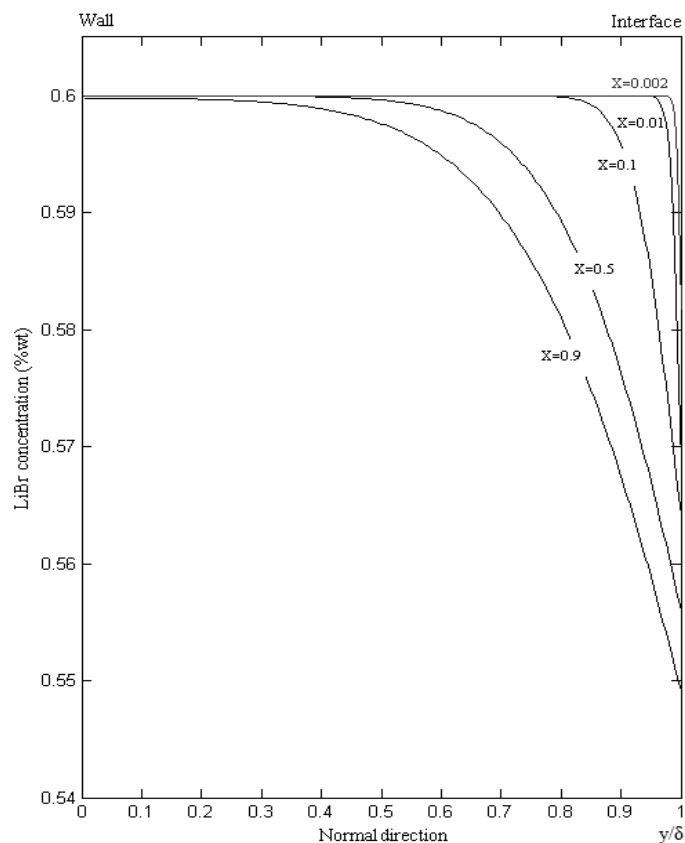


Figure 22. Cross stream LiBr concentration profiles at selected downstream positions, low temperature inlet (see Figure 9 for the definition of the domain)

The corresponding interface vapor absorption flux with distance around the tube is displayed in Figure 23. The rapid increase in the bulk temperature of the solution, as illustrated in Figures 19 and 21, leads to a significant decline in absorption efficiency as the solution travels around the tube, as seen in Figure 24. However, as the temperature profile evolves, allowing heat transfer from the film's surface to the cooling water (Figure 24), this decrease in absorption efficiency diminishes. Nevertheless, with the increase in surface vapor concentration, the driving force for absorption diminishes gradually, resulting in a gradual decrease in absorption rates as the solution circulates around the tube.

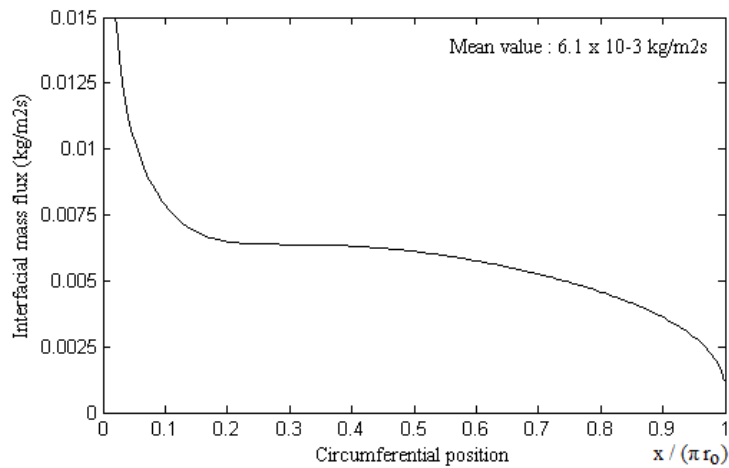


Figure 23. Variation of the interface vapour absorption flux with distance around the tube, low temperature inlet (see Figure 9 for the definition of the domain)

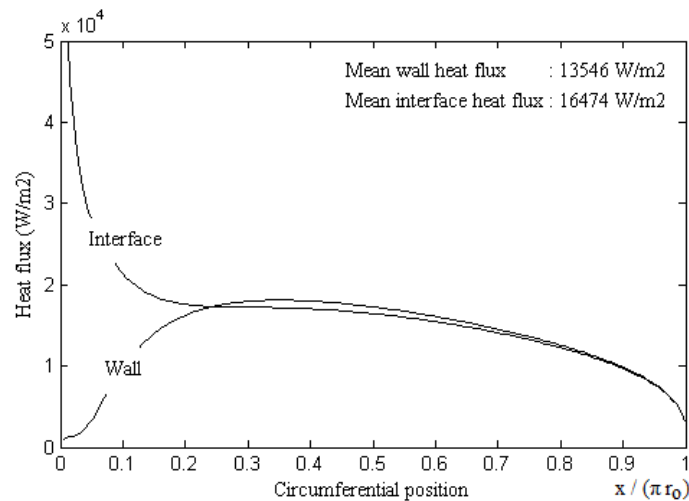


Figure 24. Variation of surface and wall heat flux with distance around the tube, low temperature inlet (see Figure 9 for the definition of the domain)

3.5. Effect of the Solution Inlet Temperature

The solution inlet temperature only effects the inlet region considerably. For the low solution inlet case, a large amount of absorption causes the bulk and surface vapour concentration to increase, hence driving potential for absorption decreases.

Figure 25 illustrates that, in scenarios where the solution enters at high temperatures, absorption rates increase as the temperature profile evolves, facilitating heat transfer from the surface to the wall. In most parts of the tube, both the bulk and surface vapor concentrations are lower compared to the scenario with a lower temperature solution inlet. Consequently, even though the low-temperature solution inlet condition initially has a considerable

advantage in the inlet region, the absorption rates in regions beyond the inlet for the high-temperature solution inlet condition are marginally higher than those in the low-temperature solution inlet condition. Nonetheless, the overall performance of the system with the low-temperature solution inlet is still about 6% higher.

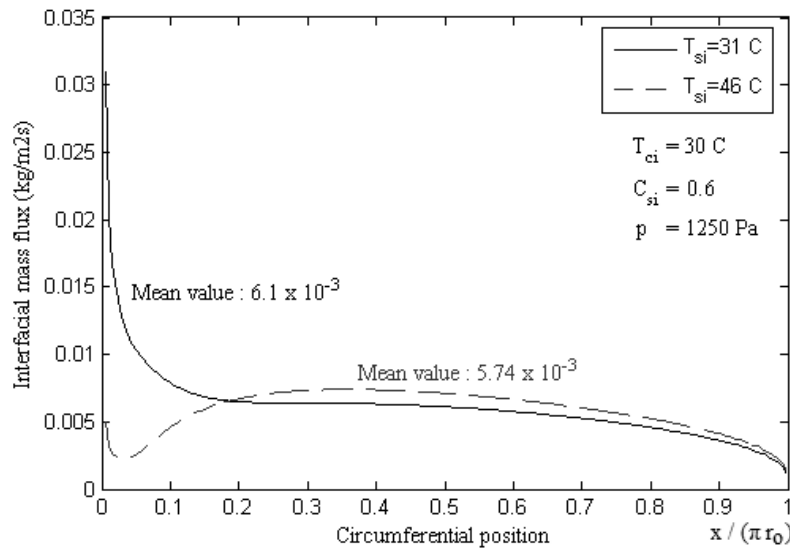


Figure 25. Surface vapour mass flux versus distance around the tube, effect of the solution inlet temperature (see Figure 9 for the definition of the domain)

3.6. Effect of the Solution Mass Flow Rate

Raising the mass flow rate of the solution leads to more resistance to heat transfer. Nevertheless, this results in a significant amount of absorption near the tube's entrance, reducing the absorption's driving potential as the solution continues through the tube. As shown in Figure 26, a higher mass flow rate correlates with diminished absorption efficiency. Specifically, increasing the Reynolds number from 5.38 to 10.77 results in a 2.5% drop in overall absorption efficiency. Further elevating the Reynolds number from 5.38 to 16.2 leads to a more pronounced decrease in absorption efficiency, totaling 5.26%.

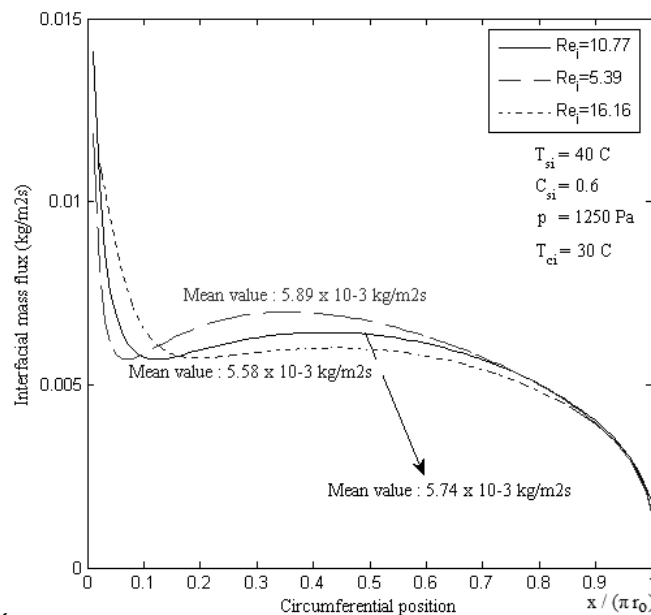


Figure 26. Surface vapour mass flux versus distance around the tube, effect of the solution mass flow rate (see Figure 9 for the definition of the domain)

3.7. Effect of the Cooling Water Inlet Temperature

The temperature of the cooling water significantly impacts absorption efficiency since vapor can only be absorbed if the heat generated during absorption is effectively transferred to the cooling water. Reducing the inlet temperature of the cooling water from 30°C to 25°C leads to a notable 26% enhancement in overall absorption performance, given the current parameters (as indicated in Figure 27). However, lowering the cooling water temperature in a cost-effective manner is often challenging, especially since it must remain above the ambient temperature when systems like cooling towers are used. In warmer regions, where the ambient temperature frequently exceeds 30°C, the cooling water's inlet temperature might reach as high as 35°C, which can significantly impair the performance of absorption systems.

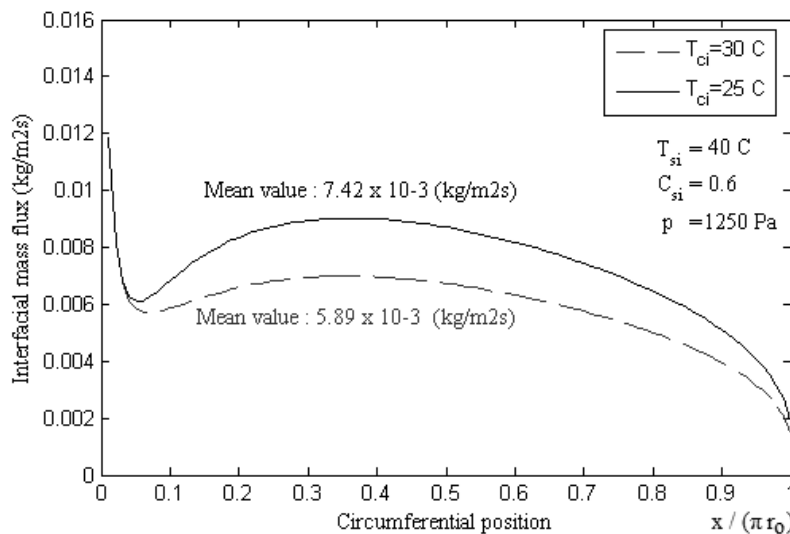


Figure 27. Surface vapour mass flux versus distance around the tube, effect of the cooling water inlet temperature (see Figure 9 for the definition of the domain)

4. Conclusions

This study provides an in-depth analysis of the performance of horizontal tubular absorbers in LiBr/H₂O absorption refrigeration systems. Utilizing a computationally efficient two-dimensional model, validated against experimental data, we explored the impacts of key operational parameters, such as solution inlet temperature, mass flow rate, and cooling water inlet temperature, on absorption efficiency. Our findings emphasize the significant role of cooling water temperature, where a decrease in inlet temperature from 30°C to 25°C resulted in a notable 26% enhancement in absorption performance, underscoring the critical importance of thermal management. Additionally, while an increase in mass flow rate boosts initial absorption rates, it also raises heat transfer resistance, leading to a complex interplay that affects overall efficiency. Specifically, increasing the Reynolds number from 5.38 to 10.77 resulted in a 2.5% drop in overall absorption efficiency, and further elevating the Reynolds number to 16.2 led to a more pronounced decrease of 5.26%. Thus, optimal mass flow rates must balance these effects to maximize performance.

Moreover, lower solution inlet temperatures improve initial absorption due to higher driving forces for mass transfer, but this advantage diminishes downstream as the solution warms, suggesting the need for fine-tuning inlet conditions based on specific system requirements. Our findings emphasize the necessity of a multidimensional approach to the design and operation of absorption systems. By meticulously adjusting the cooling water temperature and solution mass flow rates, substantial improvements in system efficiency can be achieved.

Understanding the dynamic interplay between various parameters enables the development of more robust and adaptable absorption refrigeration solutions.

Future research should consider integrating advanced numerical models and real-time optimization techniques, such as artificial intelligence and machine learning, to enhance predictive capabilities and operational efficiency. Expanding the scope to include more complex hydrodynamic conditions and three-dimensional modeling will provide deeper insights into the absorber's performance under varied operational scenarios. This study offers valuable insights and practical guidelines for optimizing horizontal tubular absorbers, contributing to the advancement of efficient and sustainable absorption refrigeration technologies.

Acknowledgments

This publication is derived from a section of a Master's thesis entitled "Numerical analysis of absorbers used in LiBr/H₂O absorption refrigeration." The thesis was presented to Dokuz Eylül University and examines absorbers in both vertical and horizontal flow configurations.

Author Statement

The authors confirm contribution to the paper as follows: study conception and design: Sercan Acarer; analysis and interpretation of results: Sercan Acarer, Nuri Kayansayan. All authors reviewed the results and approved the final version of the manuscript.

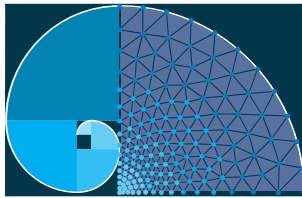
Conflict of Interest

The authors declare no conflict of interest.

References

- Alcântara, S.C.S., Ochoa, A.A.V., Peixoto da Costa, J.Â., Duarte de Menezes, F. Leite, G.N.P., Michima, P.S.A., & Marques, A.S. (2023). Development of a Method for Predicting the Transient Behavior of an Absorption Chiller Using Artificial Intelligence Methods. *Applied Thermal Engineering*, 231, 120978.
- Andberg, J. W., & Vliet, G. C. (1983). Nonisothermal Absorption of Gases into Liquid Films. *ASME-JSME Thermal Engineering Joint Conference Proceedings*, 2, 423-431.
- Andberg, J. W. (1986). Absorption of Vapors into Liquid Films Falling Over Cooled Horizontal Tubes. *PhD Dissertation*, University of Texas, Austin.
- Arroiabe, P.F., Martinez-Agirre, M. & Bou-Ali, M.M. (2022). Numerical Analysis of Different Mass Transfer Models for Falling Film Absorbers, *International Journal of Heat and Mass Transfer*, 182, 121892.
- Asfand, F., Stiriba, Y. & Bourouis, M. (2016). Performance Evaluation of Membrane-Based Absorbers Employing H₂O / (LiBr + LiI + LiNO₃ + LiCl) and H₂O / (LiNO₃ + KNO₃ + NaNO₃) as Working Pairs in Absorption Cooling Systems, *Energy*, 115, 781-790.
- Asfand, F., Stiriba, Y. & Bourouis, M. (2015). CFD Simulation to Investigate Heat and Mass Transfer Processes in a Membrane-Based Absorber for Water-LiBr Absorption Cooling Systems, *Energy*, 91, 517-530.

- Castro, J., Farnós, J. Papakokkinos, G., Zheng, J. & Oliet, C. (2020). Transient Model for the Development of an Air-Cooled LiBr-H₂O Absorption Chiller Based on Heat and Mass Transfer Empirical Correlations. *International Journal of Refrigeration*, 120, 406-419.
- Florides, G. A., Kalogirou, S. A., Tassou, S. A., & Wrobel, L. C. (2003). Design and Construction of a LiBr–Water Absorption Machine. *Energy Conversion and Management*, 44, 2483–2508
- Grigor'eva, N. I., & Nakoryakov, V. E. (1977). Exact Solution of Combined Heat and Mass Transfer Problems During Film Absorption. *Journal of Engineering Physics*, 33 (5), 1349-1353.
- Hosseinnia, S.M., Naghashzadegan, M. & Kouhikamali, R. (2016). CFD Simulation of Adiabatic Water Vapor Absorption in Large Drops of Water–LiBr Solution, *Applied Thermal Engineering*, 102, 17-29.
- Kakaç, S., & Liu, H. (1998). *Heat Exchangers: Selection, Rating and Thermal Design*. Boca Raton: CRC Press LLC.
- Kwang, J. K. (1992). Heat and Mass Transfer Enhancement in Absorption Cooling. *PhD Dissertation*, Arizona State University.
- Mortazavi, M., Isfahani, R.N., Bigham, S. & Moghaddam, S. (2015). Absorption Characteristics of Falling Film LiBr (Lithium Bromide) Solution Over a Finned Structure. *Energy*, 87, 270-278.
- Papaefthimiou, V. D., Karampinos, D. C., & Rogdakis, E. D. (2006). A Detailed Analysis of Water-Vapour Absorption in LiBr–H₂O Solution on a Cooled Horizontal Tube. *Applied Thermal Engineering*, 26, 2095-2102.
- Patankar, S. V. (1980). *Numerical Heat Transfer and Fluid Flow*. U.S.A.: Hemisphere Publishing Corporation.
- Qu, M. (2008). Model Based Design and Performance Anaysis of Solar Absorption Cooling and Heating System. *PhD Dissertation*, Carnegie Mellon University.
- Raisul Islam, M., Wijesundera, N. E., & Ho, J. C. (2006). Heat and Mass Transfer Effectiveness and Correlations for Counter-Flow Absorbers. *International Journal of Heat and Mass Transfer*, 49, 4171-4182.
- Seol, S. S., & Lee, S. Y. (2005). Experimental Study of Film Flow and Heat/Mass Transfer in LiBr–H₂O Solution Flowing Over a Cooled Horizontal Tube. *International Communications in Heat and Mass Transfer*, 32, 445-453.
- Sui, Z., Sui, Y. & Wu, W. (2022b). Multi-Objective Optimization of a Microchannel Membrane-Based Absorber with Inclined Grooves Based on CFD and Machine Learning, *Energy*, 240, 122809.
- Sui, Z., Zhai, C. & Wu, W. (2022a). Parametric and Comparative Study on Enhanced Microchannel Membrane-Based Absorber Structures for Compact Absorption Refrigeration. *Renewable Energy*, 187, 109-122.
- Tsai, B., & Perez-Blanco, H. (1998). Limits of Mass Transfer Enhancement in Lithium Bromide–Water Absorbers by Active Techniques. *International Journal of Heat and Mass Transfer*, 41 (15), 2409-2416.
- Wen, T., Lu, L. & Luo, Y. (2021). Review on the Fundamentals and Investigations of Falling Film Dehumidification/Absorption Refrigeration Based on CFD Technology. *International Journal of Heat and Mass Transfer*, 171, 121042.



Finite Element Analysis of Delamination Initiation in Wind Turbine Blade Spar Caps: Role of Compression, Strain Energy, and Principal Stresses

Ferhat Özmen^{1,*}  Ramazan Karakuzu¹ 

¹ Dokuz Eylül University, Faculty of Engineering, Department of Mechanical Engineering, İzmir

* Corresponding author: ferhatozmen35@gmail.com

Received: 07.07.2024

Accepted: 05.08.2024

Abstract

In wind turbine blades, utilizing the finite element method (FEM) to identify potential failure modes before production provides considerable value and cost savings in contrast to conventional structural tests. This paper focuses on examining the factors leading to delamination in spar caps and exploring the initiation of this delamination using the finite element method. Compression, total strain energy density, and principal stresses are significant among the variables examined to determine the effects on model deformation and crack formation. Examining these variables may contribute to understanding the mechanisms involved in initiating and progressing delamination. This study examined the effects of compression, total strain energy density, and principal stresses on model deformation and crack formation. This study focuses on the effects of principal stresses on displacement, the effects of compression on delamination and crack formation, and the effects of total strain energy density on fracture tendency and failure modes due to delamination.

Keywords: Spar cap, finite element method, compression, strain energy density, principal stress, crack formation, delamination, buckling

1. Introduction

The utilization of the finite element method (FEM) in the evaluation of potential failure modes in wind turbine blades presents a paradigm shift in the industry, offering substantial cost savings and enhanced predictive capabilities compared to conventional structural tests. Investigating failure initiation and progression through numerical simulations prior to advancing to blade production and structural testing represents a highly critical and advantageous approach. This methodology, developed through studies that have made significant contributions to the literature, is essential to ensure that the design of wind turbine blades maintains structural integrity and provides a partial validation of these designs.

Overgaard and Lund (2010) investigated the structural collapse of a wind turbine blade and determined that the collapse was caused by multiple local buckling-induced delamination processes. They identified that delamination between the spar layers led to buckling damage, resulting in the structural failure of the blade. To observe composite delamination, they defined a cohesive zone between the layers. They emphasized the need for guidelines and

recommendations to accurately assess delamination in wind turbine blades. Branner and Berring (2011) investigated the behavior of delamination in rectangular composite panels with initial delamination under compressive loading. By comparing experimental findings with a numerical parameter study, they created a buckling mode map for panels similar to the load-bearing flange in the main spar of a wind turbine blade. The study showed that the shape of the buckling mode depends on the thickness, size, and location of the delamination. Yang et al. (2012) studied the failure of a 40-meter wind turbine blade and, based on full-scale test results, demonstrated that the primary cause of the blade's failure was the separation of adhesive surfaces. Chen et al. (2014) conducted a full-scale failure test on a 52.3-meter wind turbine blade and identified that delamination in the spar caps and damage in the spar webs at the root transition zone were the primary mechanisms leading to the blade's failure. Local buckling facilitates out-of-plane deformation, contributing to this damage mechanism. Additionally, it was concluded that the thickness-direction stresses causing adhesive separation and delamination in the root transition zone of large blades should be considered in finite element analysis. Subsequently, Chen et al. (2015) investigated the local buckling strength of a 10.3-meter wind turbine blade and found, through finite element analysis, that sharp-edged blade configurations exhibited less resistance to local buckling. During testing, local buckling was observed in the spar webs and shell surfaces; however, no composite laminate failure was noted in these areas. These findings suggest the potential for different failure mechanisms across varying blade sizes. Haselbach and Branner (2016) examined the buckling behavior at the trailing edge during static tests of a 34-meter-long blade and its impact on the blade's strength. As a result of this investigation, an innovative technique incorporating a cohesive zone to model the adhesive surface at the trailing edge was proposed. Muyan and Çöker (2020), compared the static and fatigue strengths of an adhesive-separated RÜZGEM blade and an undamaged blade under flap-wise loading using numerical analyses. The results showed that the strength of the RÜZGEM blade with adhesive failure significantly decreased compared to the undamaged blade under both static and fatigue loadings.

This study revisits two significant contributions to the literature by applying advanced methods from finite element simulation programs within a specific scope and presents new findings. Batmaz et al. (2021) examined the finite element model of the RÜZGEM 5-meter glass fiber reinforced polymer wind turbine blade, whose spar cap is made of different composite layers, under the minimum flapwise load, the adhesive separation failure based on the cohesive zone model at the high pressure shell side-spar interface. The adhesive separation failure occurring at the specified load level was found not to adversely affect the structural integrity of the blade in a catastrophic manner. Haselbach (2015) investigated an 8.65-meter-long blade section with different initial delamination in the main spar by applying a cantilever bending moment. In this blade model, where the spar cap is entirely unidirectional (UD), local buckling caused high stresses and strains around the delamination, potentially exceeding the material's design properties and making failure initiation and progression more likely.

This paper meticulously examines the variables influencing model deformation and crack initiation, emphasizing the critical roles of compression, total strain energy density, and principal stresses. By elucidating these dynamics, the research aims to provide a deeper understanding of delamination initiation and progression, offering valuable insights for optimizing blade design and enhancing structural integrity. The investigation focuses on the consequences of principal stresses on displacement, the impact of compression on delamination and crack formation, and the influence of total strain energy density on fracture propensity and delamination-induced failure modes. In general, tensile stress is prevalent at the intersection of the spar cap and blade root in spar caps and blades, while compressive stress is predominant in the remaining parts. This is attributed to the bending force applied by

the spar cap to support the blade and the pressure differentials on the blade surface caused by wind. Compressive stresses help mitigate crack formation and propagation. It is crucial for the blade areas experiencing significantly higher tensile stress than compressive stress to possess more excellent resistance. Otherwise, the blade may be susceptible to breaking or cracking at this location. Total strain energy density (TSED) values indicate the area where a crack will occur. In the case of adhesive separation of a material, TSED values often reach maximum values. In this way, the regions where TSED values are maximum indicate the places where adhesive separation will begin. TSED is essential in material failure analysis, identifying critical crack formation or growth regions, and estimating structural strength. Wind-induced pressure produces material stresses as principal stresses, which are the main factors that cause the buckling of spar caps. Local buckling in the delamination region under the influence of principal stresses may cause the central area of the delamination to be subjected to different stresses in different directions, resulting in stress concentration. As a result, stress concentration occurs at the delamination boundary due to principal stresses along the bending direction of the laminate. The concentration of principal stresses is a potential failure zone for the adhesive element. If the principal stresses exceed the strength of the cohesive member, the cohesive member will rupture, and the two connected parts will separate.

This study used two wind turbine blade models to examine delamination initiation criteria: the RÜZGEM 5-meter wind turbine blade as the first blade model (Batmaz et al., 2021) and the DTU 10 MW wind turbine blade as the second model (Haselbach, 2015).

2. Finite Element Analysis Details

2.1. Materials of RÜZGEM 5-m Wind Turbine Blade Model

In assembling the finite element model of the RÜZGEM 5-meter blade, the design of the composite laminates and the blade structure for the root and trailing edge/spar web panels considered four different materials. Specifically, two types of glass fabric (Triax and UD), steel, and polymeric foam (Divinycell H45) were used as core materials for the sandwich structures (Table 1).

Table 1. Material properties of RÜZGEM 5-m Wind Turbine Blade Model

Materials/Engineering Constants	Density (kg/m ³)	Modulus (GPa)	Strength (MPa)	Poisson Ratio
Lamina (Triax)	1896	E ₁ = 24.84 E ₂ = 9.14 G ₁₂ =2.83	S _{XT} = 191.73 S _{XC} = 101.16 S _{YT} = 16.86 S _{YC} = 50.41 S _{SH} = 11.29	0.29
Steel	7850	E= 210	S=581.80	0.30
Gelcoat	1200	E= 3.98	S=35.29	0.34
CSM 300 (UD)	1896	E= 9.14	S=16.86	0.29
Divinycell H45 (Foam)	48	E ₁ = 55E-03 E ₂ = 55E-03 G ₁₂ = 15E-03	S _T =1.40 S _C =0.60 S _{SH} =0.56	0.40
Adhesive	1400	E= 3.00 G ₁₂ = 1.59	S= 7.8	0.30

2.2. Contact Status of RUZGEM 5-m Wind Turbine Blade Model

In the predicted adhesive separation failure area, the cohesive zone was defined with adhesive models (Figure 1). Glue contact was preferred so that the connection between the adhesive and composite parts is suitable for the multi-point constraint method (Batmaz et al., 2021). In this study, a new investigation was conducted using the Glue Breaking effect instead of the MPC algorithm in MSC Marc/Mentat.

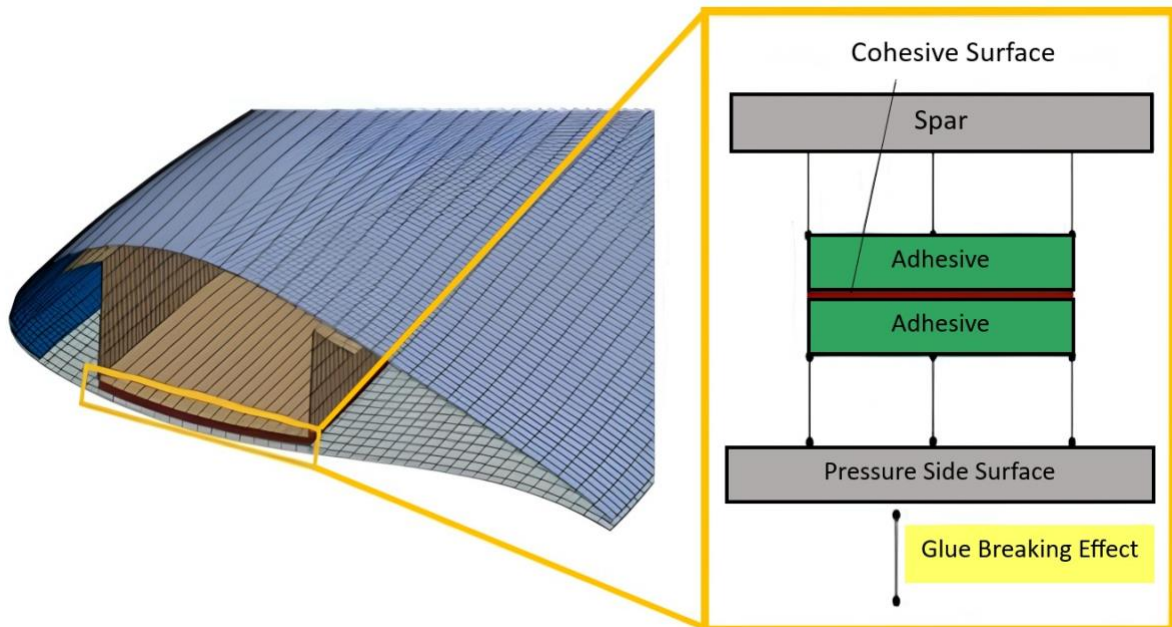


Figure 1. Schematic of the adhesive model (Batmaz et al., 2021)

2.3. Boundary Conditions of RUZGEM 5-m Wind Turbine Blade Model

In the first blade analysis study, as RUZGEM 5-m wind turbine blade and its spar cap, the adhesive region with 3D solid elements was created to connect the pressure side and two shell structures, such as a spar cap. The RUZGEM 5-m wind turbine blade is fixed at the blade root, and the spar cap supports the blade with adhesive bonding. The wind load on the blade exposed to 10 m/s wind speed was simulated and the blade root section is fixed as the boundary condition. The pressure distribution on the blade was first calculated using the MSC Cradle due to the wind flow. The material safety coefficient is accepted as 2.5. The number of shell elements and nodes is approximately 60 thousand, and the element sizes are generally around 15 mm. The material model in the finite element model created using the blade was verified through modal analysis in MSC Apex finite element software. Nonlinear static and buckling analyses were performed in MSC Marc/Mentat (Figure 2, Figure 3) (Batmaz et al., 2021).

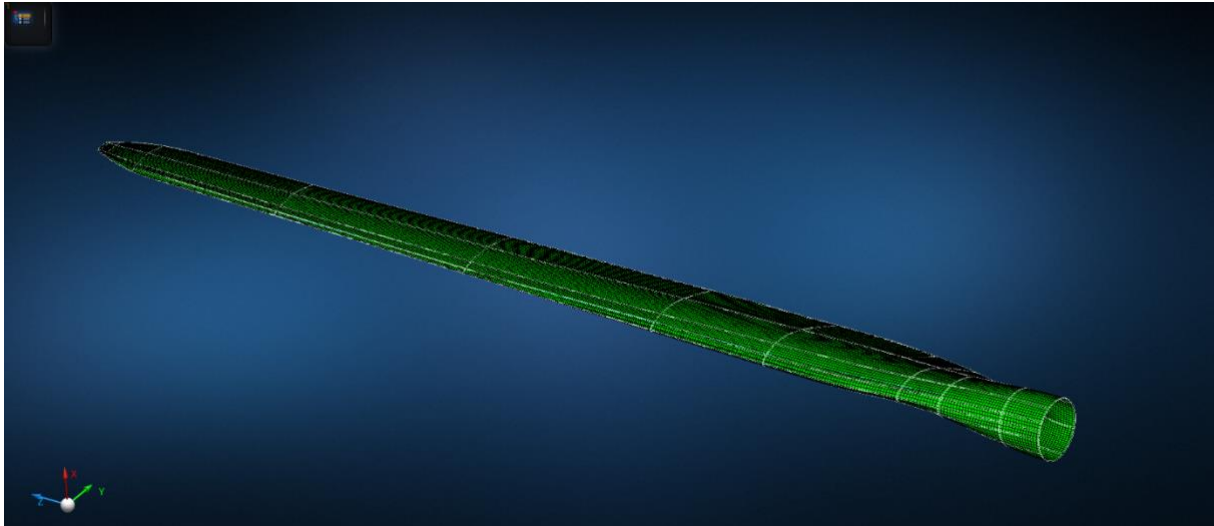


Figure 2. Ruzgem 5-m wind turbine blade

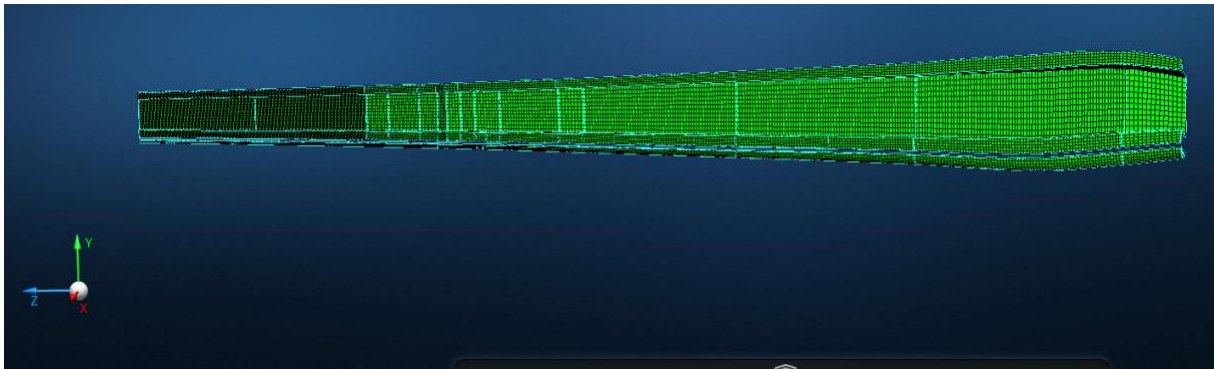


Figure 3. Spar cap of Ruzgem 5-m wind turbine blade

2.4. Materials of DTU 10 MW Wind Turbine Blade Model

The required materials and configurations were obtained from tables and graphs for the DTU 10 MW wind turbine blade section (Table 2). The outer surface of the blade was utilized as the reference surface containing the finite element nodes. The complete arrangement and material properties of the blade are available online (Bak et al., 2013). The spar cap of the DTU 10 MW wind turbine blade is composed of layers made entirely of UD material, arranged in a uniform configuration (Figure 4).

Table 2. Material properties of DTU 10MW Wind Turbine Blade

Engineering Constants	E_{11} (GPa)	E_{22} (GPa)	ν_{12}	X^T (MPa)	X^C (MPa)	Y^T (MPa)	Y^C (MPa)	S^L	S^T	ρ (kg/m ³)
U/D Glass	41.26	11.39	0.33	903.6	660.16	42.14	42.14	58.65	58.65	1931

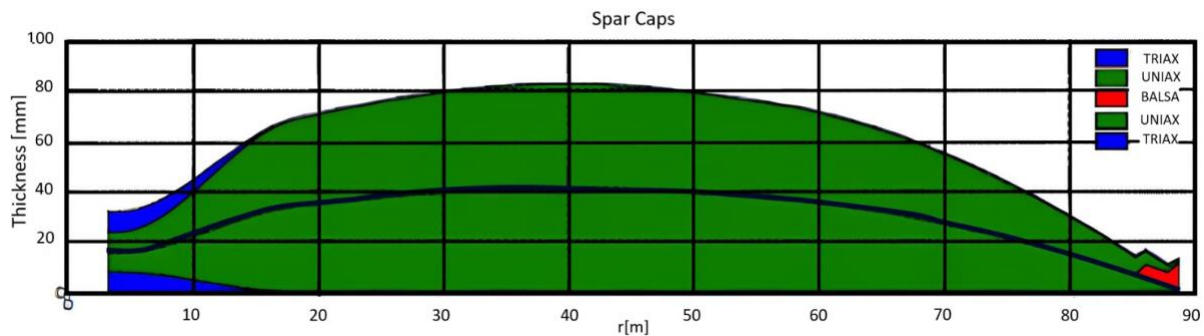


Figure 4. Composite layout of the DTU 10 MW wind turbine blade regions: Spar cap thickness in the 40-50m range of from blade root to blade tip (Castro and Branner, 2021)

2.5. Contact Status of DTU 10 MW Wind Turbine Blade Model

A contact definition was not established for the spar cap and other structures of the DTU 10 MW wind turbine blade. Consequently, the blade was designed as a rigid structure, and simulation studies commenced accordingly.

2.6. Boundary Conditions of DTU 10 MW Wind Turbine Blade Model

In the second blade analysis study, the DTU 10 MW wind turbine blade and its spar cap, the shell model contains approximately 40,000 four-node shell elements. The typical element length in the model was 0.05m (Figure 5). All nodes representing the posterior section (closest to the root) were fully constrained. The front section nodes were connected to a reference node using a constraint known as a rigid link (RBE2), allowing the front section to function as a rigid body. The blade section near the root on the opposite side of where the moment was applied was fixed as a boundary condition (Figure 6). The connections at the trailing edge and cap/body were generally modeled without specifying specific geometric details at the connection points. Three moments were applied to the reference node at the front: $M_x = -16.4e9$ Nmm, $M_y = 2.4e9$ Nmm, and $M_z = 0.32e9$ Nmm. The moments correspond to approximately 100% of the design loads evaluated for the airfoil section at $r = 48.775$ m (middle of the simulated airfoil section). Experimental studies on the compressive strength of thick composite panels have shown that the loading must be high before delamination propagation near the panels' center. The moment was applied to ensure delamination growth was included in all simulated cases, including a safety factor of 1.35 (Haselbach, 2015).

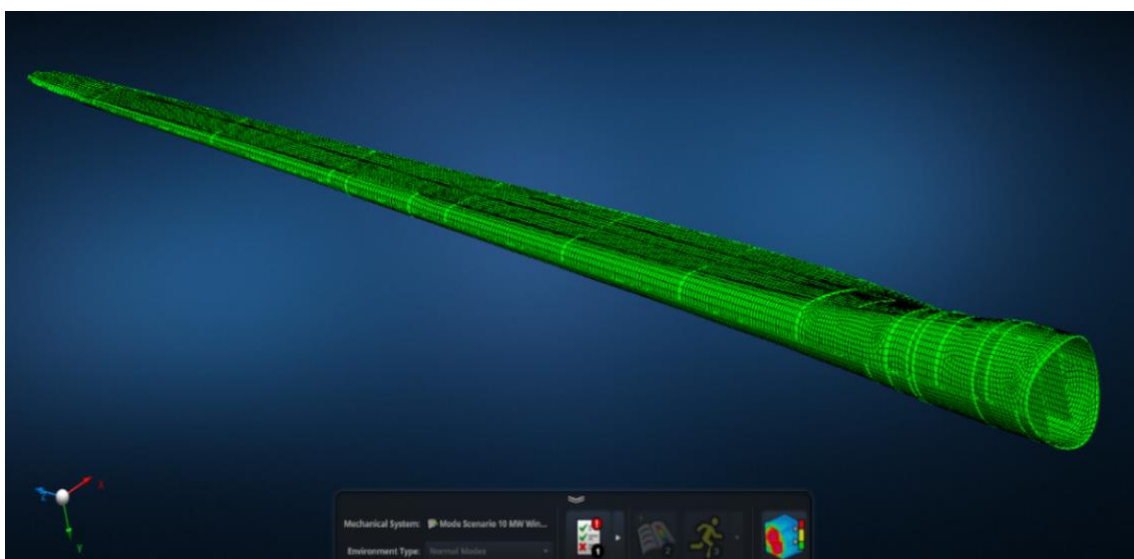


Figure 5. DTU 10 MW wind turbine blade (86-m)

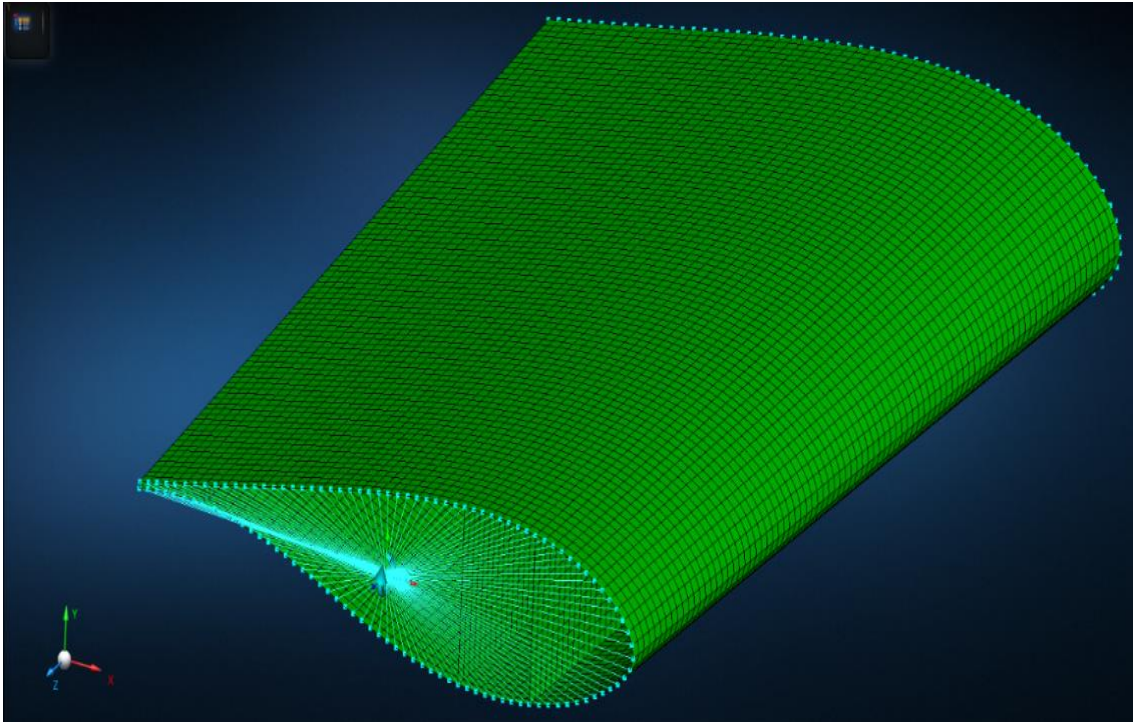


Figure 6. The blade section near the blade tip with applied moment (RBE2)

Mesh refinement was applied to the shell elements around the area of interest, where the initial delamination was modeled to reduce the characteristic element length to 0.01 m. The region surrounding the delamination was discretized using a fine mesh. The simulation applied the submodel method to simulate buckling-induced delamination growth in the spar cap (Mankins, 2023). The lower model was 1.7 m long and placed in the cap's center (Figure 7).

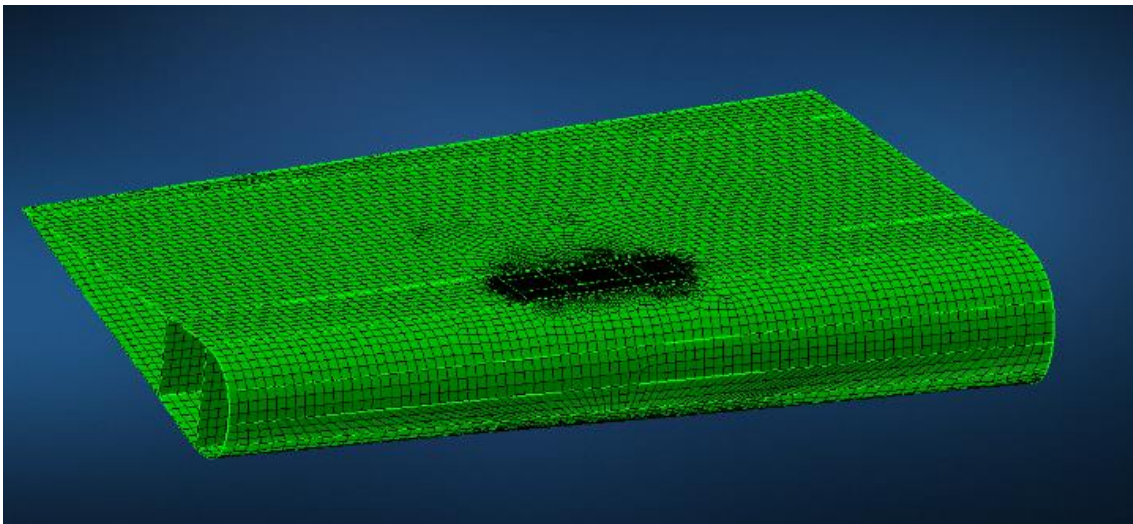


Figure 7. Blade section shell model of DTU 10MW wind turbine with mesh improvement

3. Results and Discussions

3.1. Role of Compression on RUZGEM 5-m Wind Turbine Blade Model

The tensile stress at the intersection of the spar cap and the blade root is much higher than the compressive stresses in the remaining part (Figure 8, Figure 9). There is a spar cap along the

remaining part of the blade, but tensile stress is dominant only in the first part of the spar cap, where it intersects with the pressure side. This is because the bending force exerted by the spar cap to support the blade load is greater at the intersection of the blade root and the spar cap. The blade root is the thickest part; therefore, the most significant portion of the blade load is applied at this point. This causes a more significant bending moment where the spar cap intersects the blade root. This bending moment causes the spar cap to be pulled towards the blade root, resulting in tensile stresses. As a result, where the tensile stress in a spar cap of the blade is dominant, the bending force exerted by the spar cap to support the blade load is most significant. This is usually where the spar cap intersects the blade root.

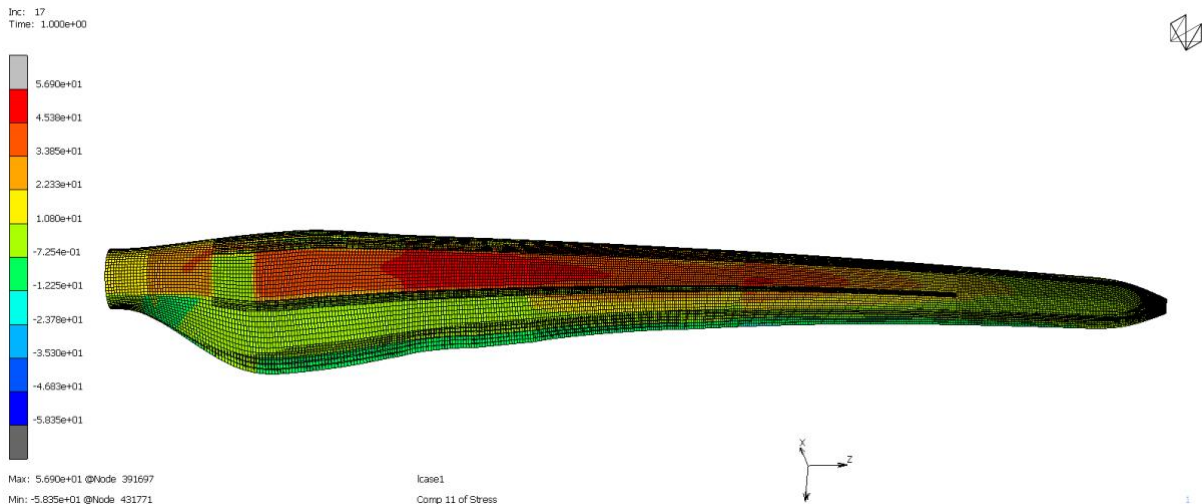


Figure 8. Compressive stress effect in the region where the material is expected to be subjected to a higher tension along 1 direction and the onset of adhesive failure is expected

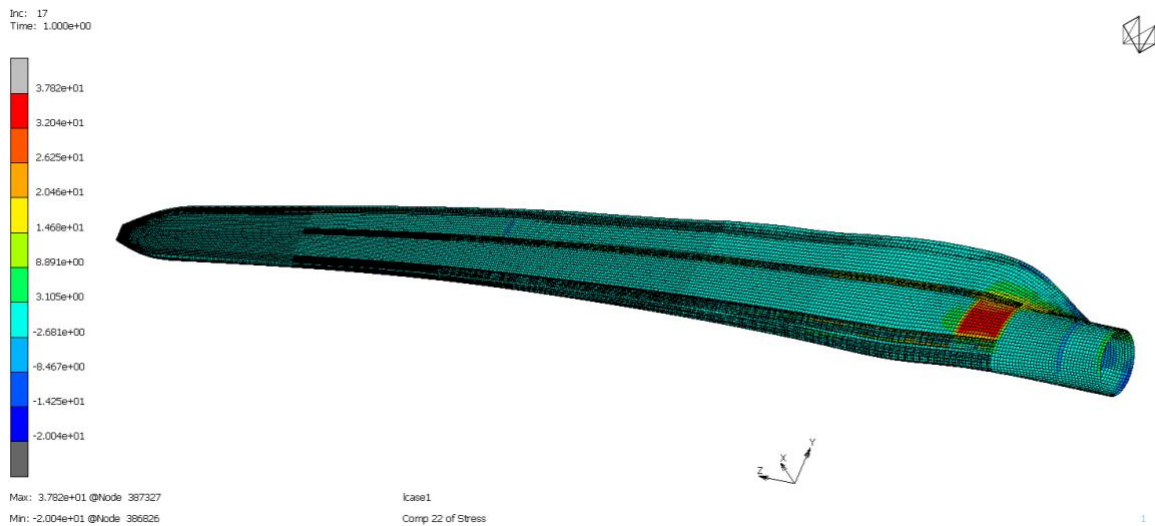


Figure 9. Tensile effect in the region where the material is expected to be exposed to a higher compression along 2 directions and the onset of adhesive failure

In general, tensile stress dominates at the intersection of the spar cap and blade root in spar caps and blades, while compressive stress dominates in the remaining part. This is due to the bending force exerted by the spar cap to support the blade and the pressure differences on the blade surface due to wind. There are several reasons why compressive stresses characterize this area:

1. In this intersection region, the spar cap separates from the pressure side, forming a bulge towards the suction side. This bulge creates a force center that causes compressive stresses on the suction side.

2. This region is subjected to blade bending at the blade root. When the blade is subjected to bending, compressive stresses occur on the suction side. This means that the blade root exerts a force towards the suction side.
3. This region is exposed to blade vibrations at the blade root. When the blade vibrates, compressive stresses occur on the suction side. This means that the blade root exerts a force towards the suction side.

Combining these three factors causes compressive stresses to dominate in this region. These compressive stresses can cause crack formation and material failure on the suction side. The intersection between the spar cap and the pressure side can be made smoother to reduce the stresses in this area. Additionally, measures can be taken to minimize blade bending and vibrations. This tensile force is much greater than the compressive stresses. As a result of this situation, the strength of the material at the intersection of the spar cap and the blade root must be higher than the strength of the material in the remaining part. Otherwise, the material may break or crack at this point. Where the spar cap intersects the blade root:

- Tensile stresses predominate.
- Tensile stresses are caused by the bending force exerted by the spar cap to support the blade load.
- Tensile stresses are much higher than compressive stresses.
- Compressive stresses are lower than tensile stresses at the intersection of the spar cap and the blade root.

Von Mises stress is defined as the square root of the mean of the squares of the three principal stress components of the material; therefore, von Mises stress indicates how close the material is to plastic deformation by combining the effects of the three principal stress components of the material (Figure 10).

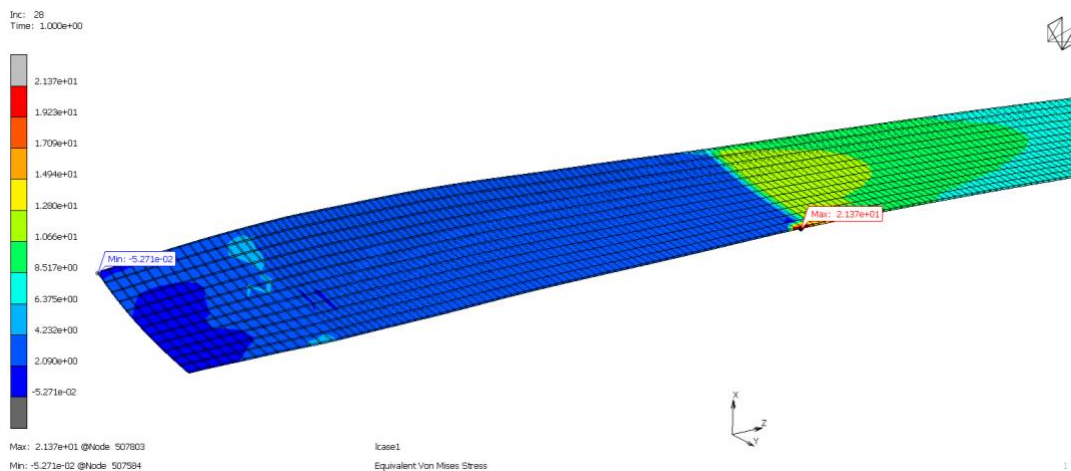


Figure 10. Equivalent of von Mises stresses

3.2. Role of Total Strain Energy Density on RUZGEM 5-m Wind Turbine Blade Model

Total strain energy density (TSED) is the strain energy stored in the unit volume of the material. Therefore, total strain energy indicates how much energy the material consumes during plastic deformation. The fact that the von Mises stress maximum point is slightly further away from the total strain energy density maximum point may suggest that the material is softer and more ductile at the other end of the region. In this case, even though the material in the area has a high von Mises stress, the total strain energy density will be low. To

determine this situation more precisely, measurements of the material's properties, the applied load, and the form factor of the region are required.

The Crack Initiator method is a tool used to identify the initiation of a crack within a structure. No delamination or Turon method was used. The critical zone for cracks and structural failure is more likely to be in the area 1 meter further from the tip of the spar cap. The reason why no crack formation is observed in the section chosen as the crack initiation may be the compressive stresses and the total strain energy density. As a result, the difference in the regions where von Mises stress and total strain energy density are concentrated may be due to the difference in material properties, applied load, or form factor of the region. The bonding force between the layers and the adhesive bonding can be subjected to stresses that reduce the strength (Figure 11).

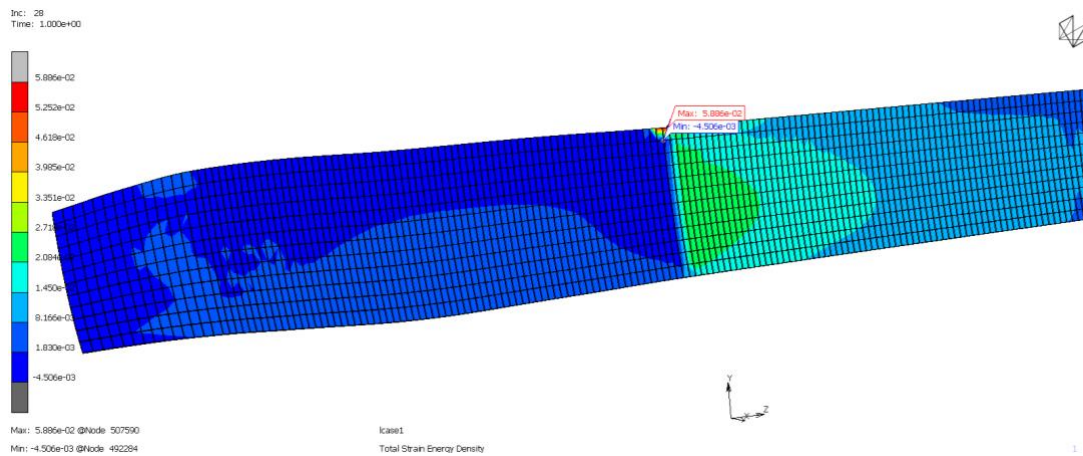


Figure 11. Total strain energy density and crack initiation

Total Strain Energy Density (TSED) values indicate the area where a crack will occur. These maximum values indicate the crack that will start when the adhesive separates. In the case of adhesive separation of a material, TSED values often reach maximum values. These maximum values represent the crack's location, which will initiate adhesive separation and the energy required for the crack to grow. In this way, the regions where TSED values are maximum indicate the places where adhesive separation will begin (Figure 12) (Branner and Berring, 2011).

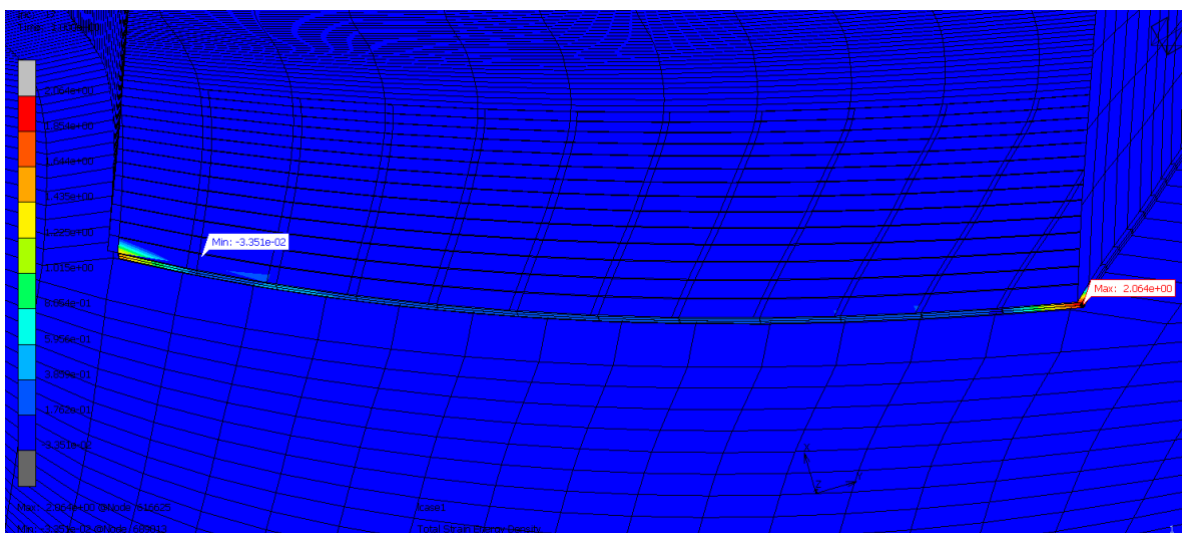


Figure 12. Total strain energy density in the adhesive region where failure is expected

TSED is essential in material failure analysis, identifying critical crack formation or growth regions, and estimating structural strength. These values can be determined through various material tests and simulations and used to understand the material's structural behavior (Figure 13).

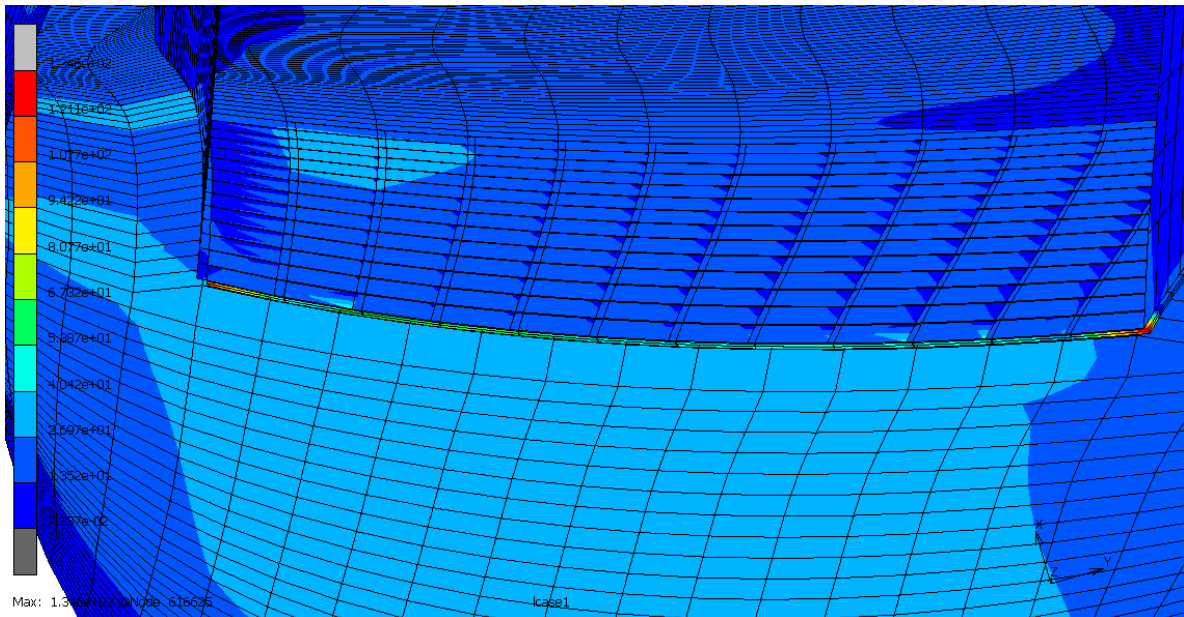


Figure 13. Stress distribution in the adhesive region where failure is expected

Crack formation is expected to occur more in the region where the total strain energy density is concentrated, and the Crack Initiator is generally assigned to these concentrated regions. It was observed that the contact status was eliminated both in the area where adhesive separation was expected and, in the part, where laminate breakage was expected (Figure 14).

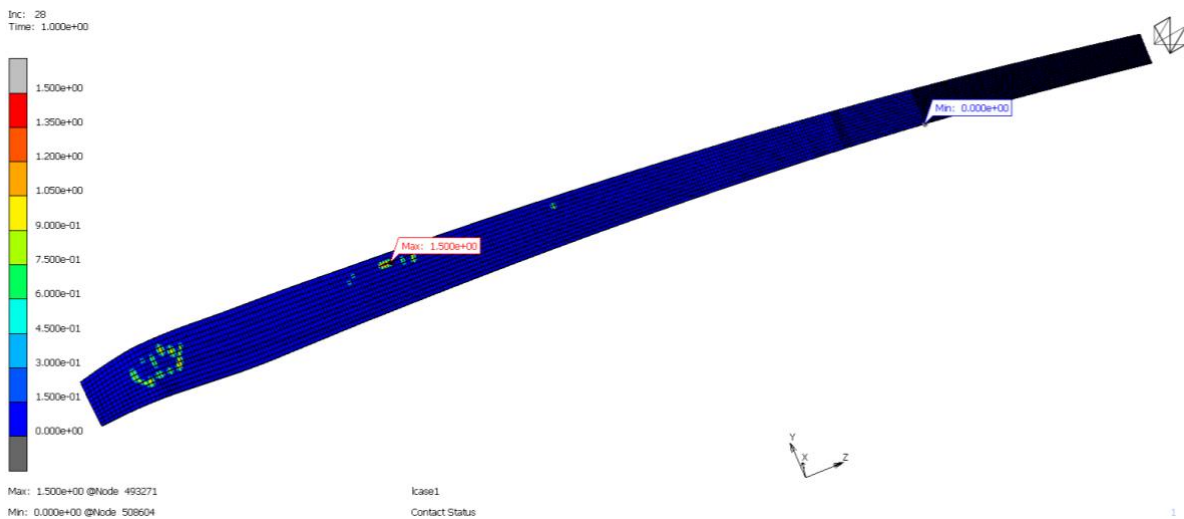


Figure 14. Contact status was eliminated both in the area as an adhesive separation and laminate breakage was expected

The spar cap region, which marks the beginning of delamination, was selected as the crack initiation site to examine the formation of cracks, fractures, and structural failure. No cracks were observed, possibly due to compression. Tensile stresses generally open cracks, while compressive stresses tend to close them. This suggests that delamination does not directly result in "fracture." Instead, it is just one of the factors that can lead to structural failure (Figure 15).

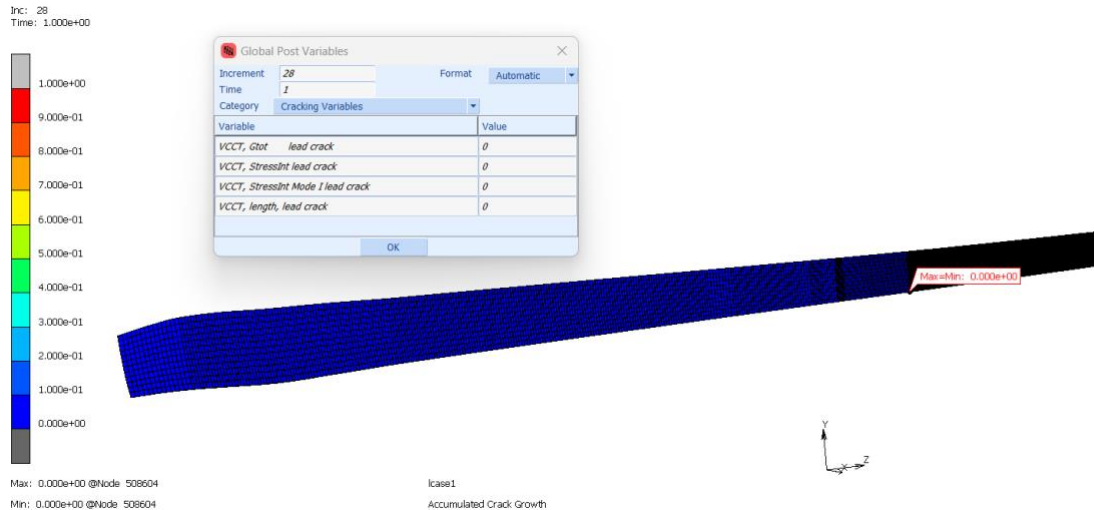


Figure 15. No crack growth

3.3. Role of Principal Stress on RUZGEM 5-m Wind Turbine Blade Model

Cohesive zone modeling (CZM) is a numerical technique to simulate fracture and delamination in materials and structures. It is a method employed to model the behavior that arises when two composite layers separate. This method is invaluable in analyzing structures subjected to loading conditions that may induce crack propagation. In cohesive zone model analysis, Element 149 is used as an 8-node solid composite element, 75 as a 4-node shell element, and 188 as the 8-node interface element. Various experiments were conducted, and VCCT and CZM methods were assessed to determine the potential for Glue Breaking effect (Figures 16, Figure 17). The Glue Breaking feature relies on regular Touch contact, which may involve friction and other properties when the criterion for breakage in the glue contact is reached (Table 3).

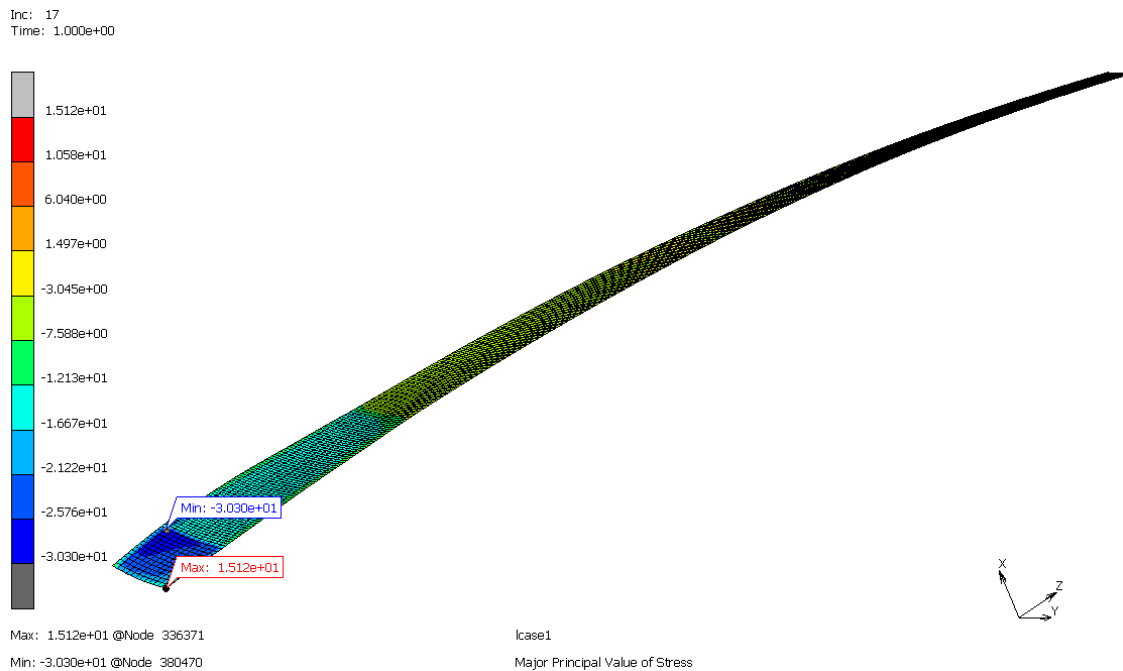


Figure 16. Minimum and maximum principal stresses - CZM (non-Glue Breaking)

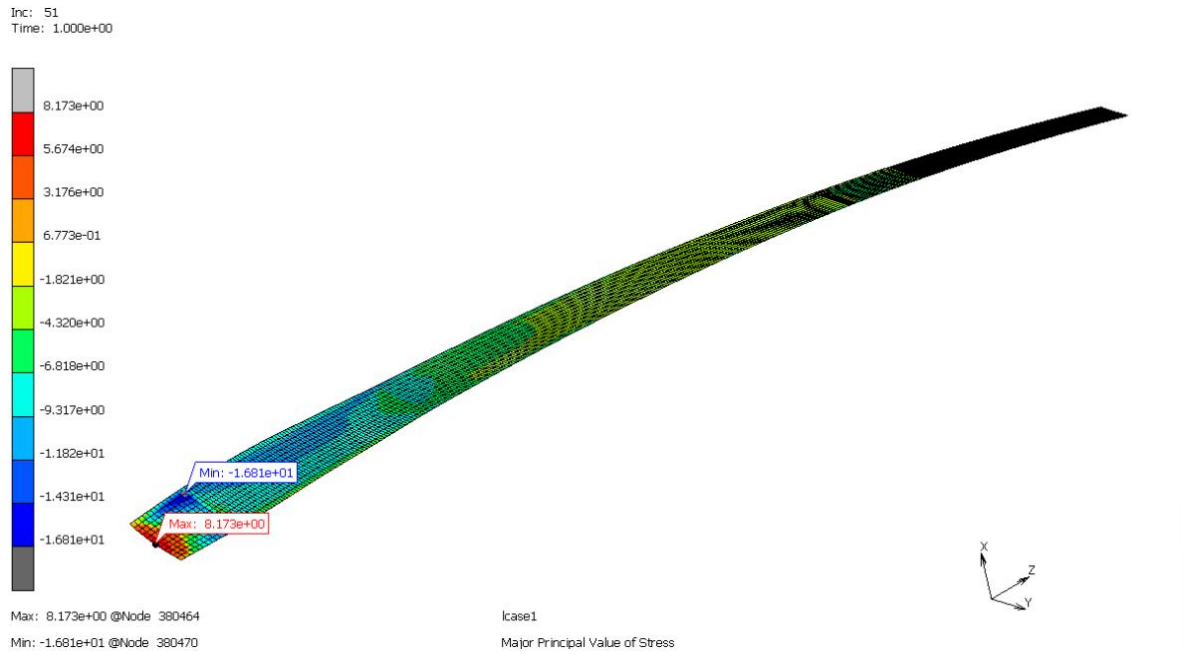


Figure 17. Minimum and maximum principal stresses - CZM (with Glue Breaking)

Table 3. Cohesive zone status

CZM (non-Glue Breaking)		CZM (with Glue Breaking)	
Type	Stress Values (MPa)	Type	Stress Values (MPa)
Max. Principal Stress	-30.30	Max. Principal Stress	8.2
Min. Principal Stress	15.1	Min. Principal Stress	-16.8

Virtual Crack Closure Technique (VCCT) is a powerful fracture mechanics tool that predicts the crack tip's strain energy release rate (SERR). It can be used with various material models, including linear elastic, elastic-plastic, and cohesive zone models. It is used for crack growth prediction, fracture toughness evaluation, or design optimization of cracked structures. Accuracy is reduced in CZM studies without Glue Breaking (Table 4), and CZM gives almost the same results as VCCT (Figure 18, Figure 19).

Table 4. VCCT failure status

VCCT (non-Glue Breaking)		VCCT (with Glue Breaking)	
Type	Stress Values (MPa)	Type	Stress Values (MPa)
Max. Principal Stress	-30.32	Max. Principal Stress	8.2
Min. Principal Stress	15.13	Min. Principal Stress	-16.8

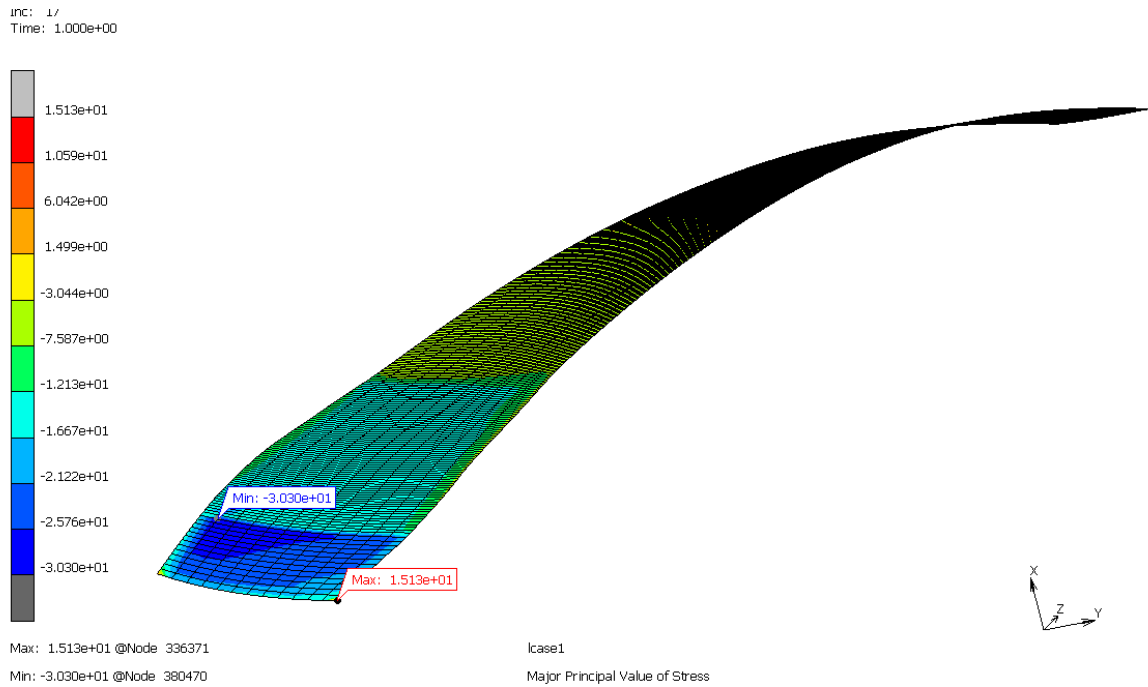


Figure 18. Minimum and maximum principal stresses - VCCT (non-Glue Breaking)

In the analyses performed on the RUZGEM 5-meter wind turbine blade, no difference was observed between VCCT and CZM. From this analysis, we understood no crack formation in VCCT. Although there was failure in this area, it was observed that there was no structural destruction. When the interface properties were entered into adhesive contact in the cohesive region with Glue Breaking, the stress values obtained more accurate results than the reference values.

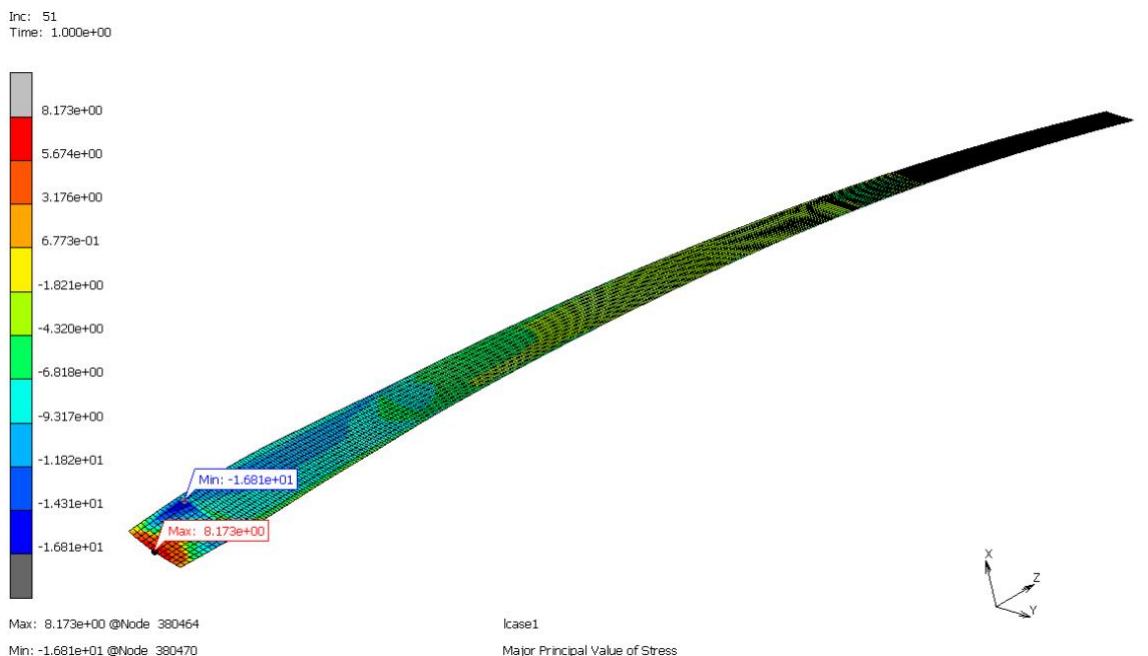


Figure 19. Minimum and maximum principal stresses - VCCT (with Glue Breaking)

3.4. Role of Compression and Principal Stress on DTU 10 MW Wind Turbine Blade

Spar cap failure may result from out-of-plane deformation caused by wind loads. This failure can manifest as transverse tensile failure in unidirectional layers closest to the neutral axis or

as interlayer shear failure between layers. The typical blade arrangement, with fibers primarily aligned in the longitudinal direction, renders the spar cap relatively flexible in the lateral direction, thereby increasing the risk of transverse stress failure. Furthermore, manufacturing defects within the laminate further reduce its fatigue and ultimate strength. The +y axis is critical for this region. σ_{22} , which is significantly high at the boundary of the delamination zone, plays a crucial role in buckling failure (Figures 20, Figure 21).

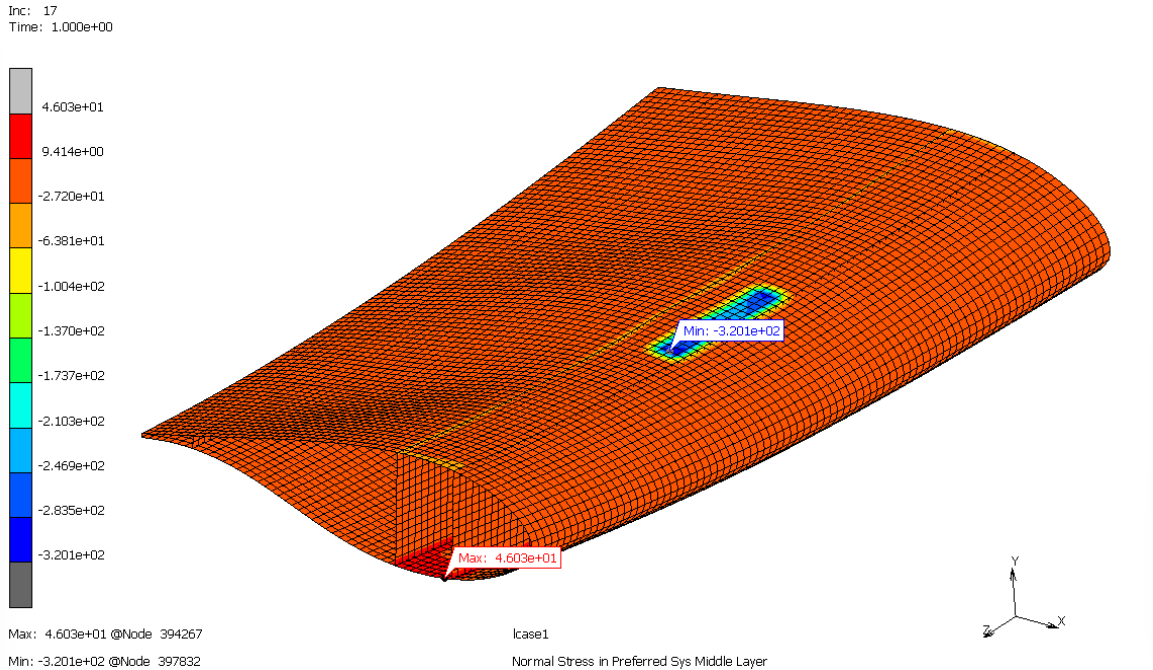


Figure 20. Normal stress in the critical region

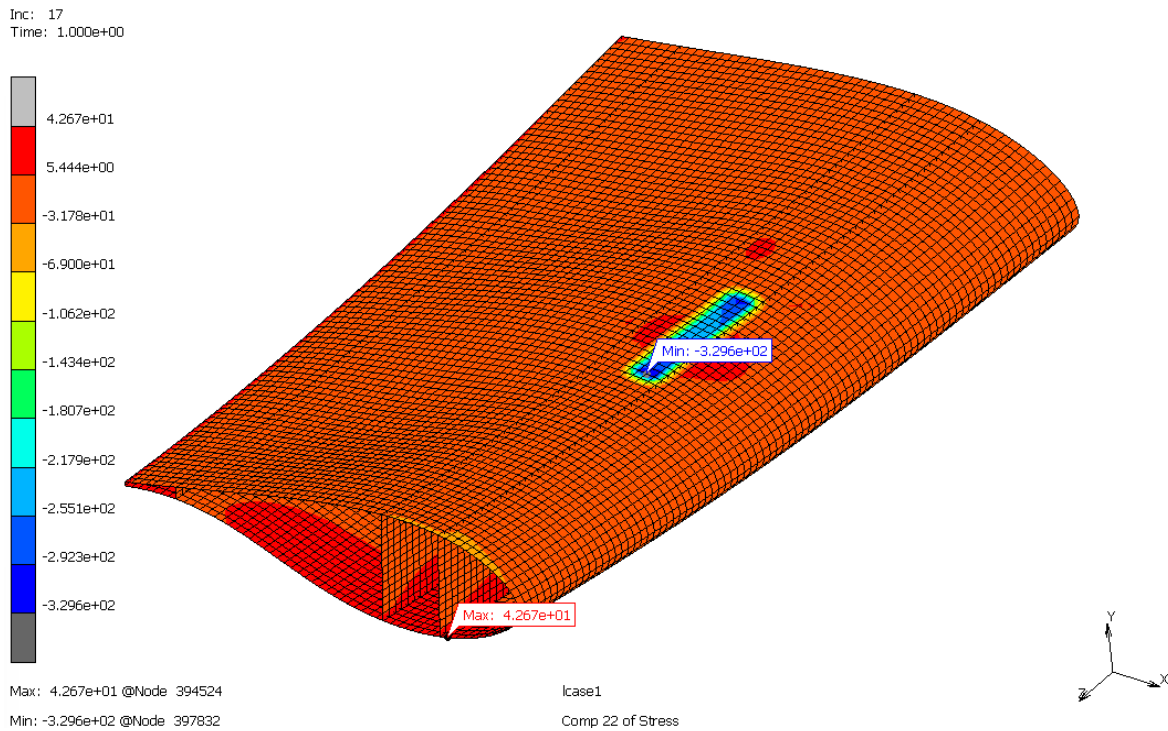


Figure 21. σ_{22} values in the critical region

In the context of the influence of principal stresses on blade failure, it is observed that tensile stresses predominantly affect the low-pressure surface (suction shell) of the blades, except in a specific area. This area corresponds to the blade root projection on the blade's pressure side,

intersecting with the spar cap and extending to the suction side. In this specific green-colored region, compressive stresses are more prominent. Multiple factors contribute to the prevalence of compressive stresses in this area. Local buckling-induced delamination occurs in the spar cap's middle section, where the blade root compressive stresses are most pronounced (Figure 22, Figure 23).

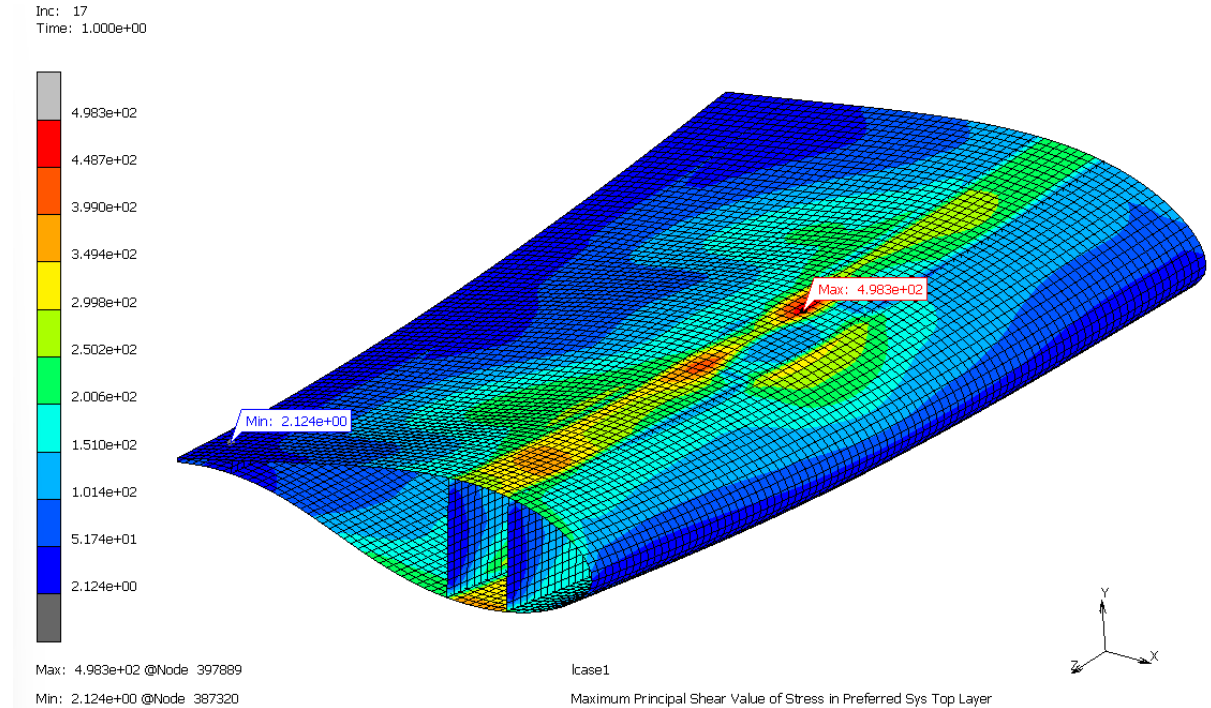


Figure 22. Maximum principal shear stresses in the critical region

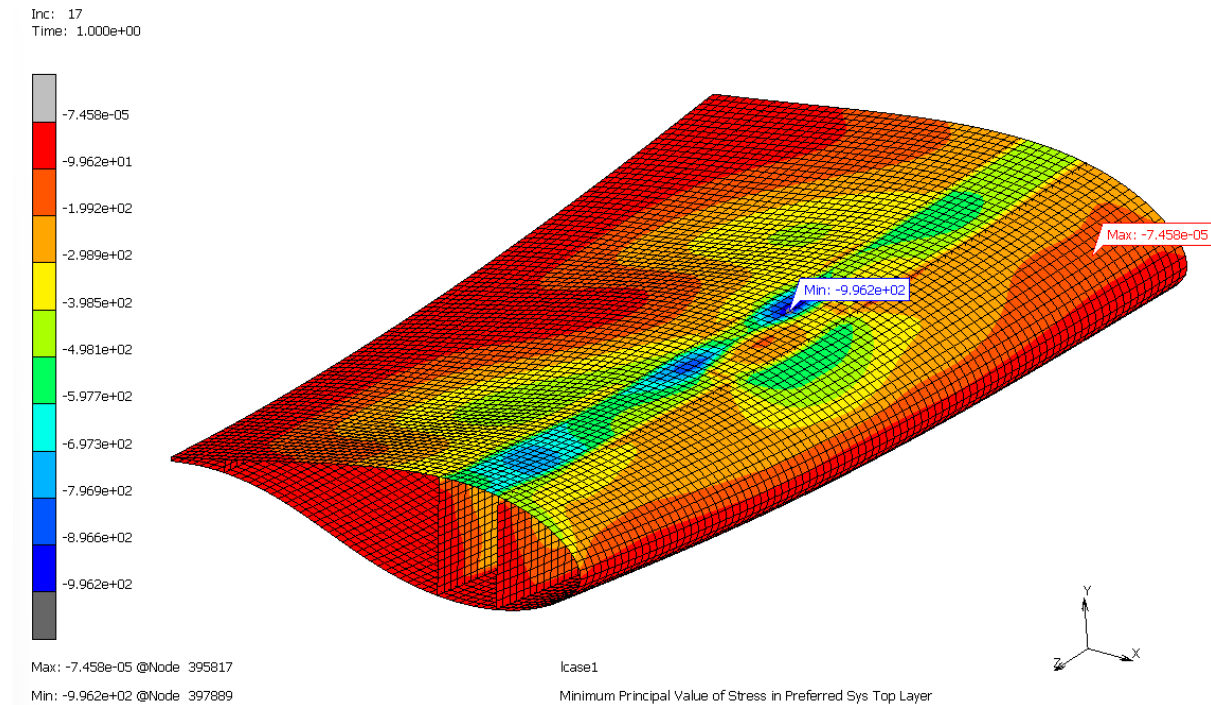


Figure 23. Minimum principal stresses in the critical region

This delamination further intensifies the stresses, subjecting the fibers to compression in two directions, potentially exceeding their tensile strength and leading to crack formation. The σ_{11} value, exceptionally high at the delamination boundary, significantly influences buckling

fracture. The σ_{11} value surpasses the σ_{22} and σ_{33} values at the delimiting boundary of the material in shell models, experiencing elevated stress in the direction 1 (Figure 24).

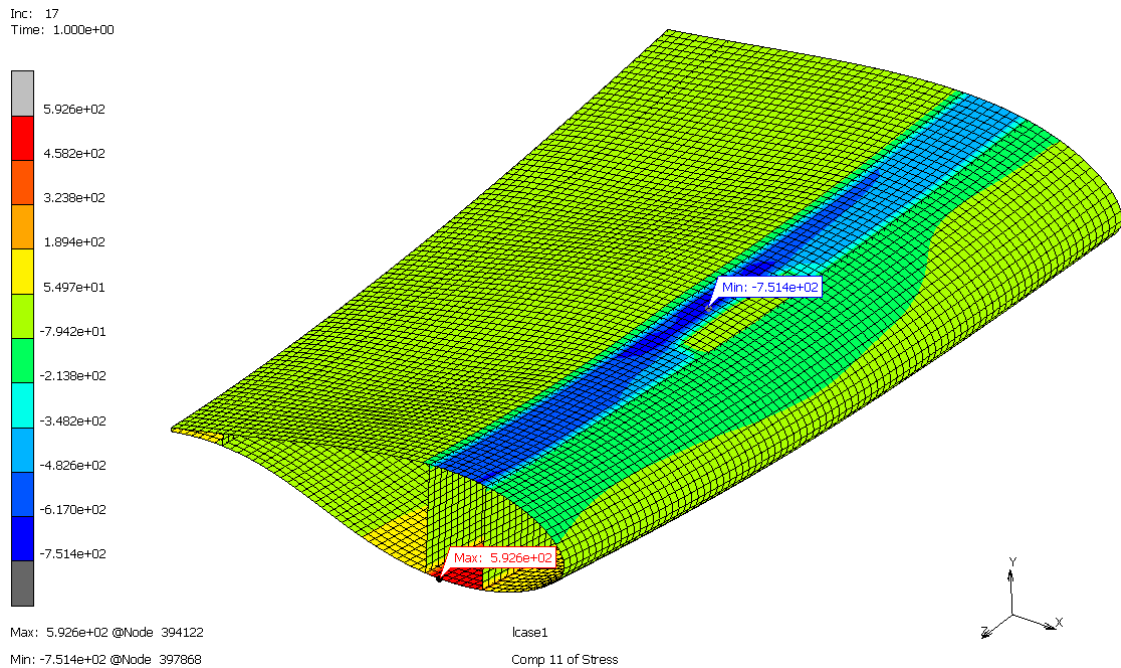


Figure 24. Effect of σ_{11} , which has a high value at the delamination boundary on local buckling

In the central region of the delamination, the magnitudes of σ_{11} and σ_{22} surpass those of σ_{33} , indicating that the material is subjected to more significant tensile stress along direction 1 and compressive stress along direction 2. The σ_{33} stress is oriented perpendicular to the fiber direction, and the layer surface exhibits a lower value (Figure 25)

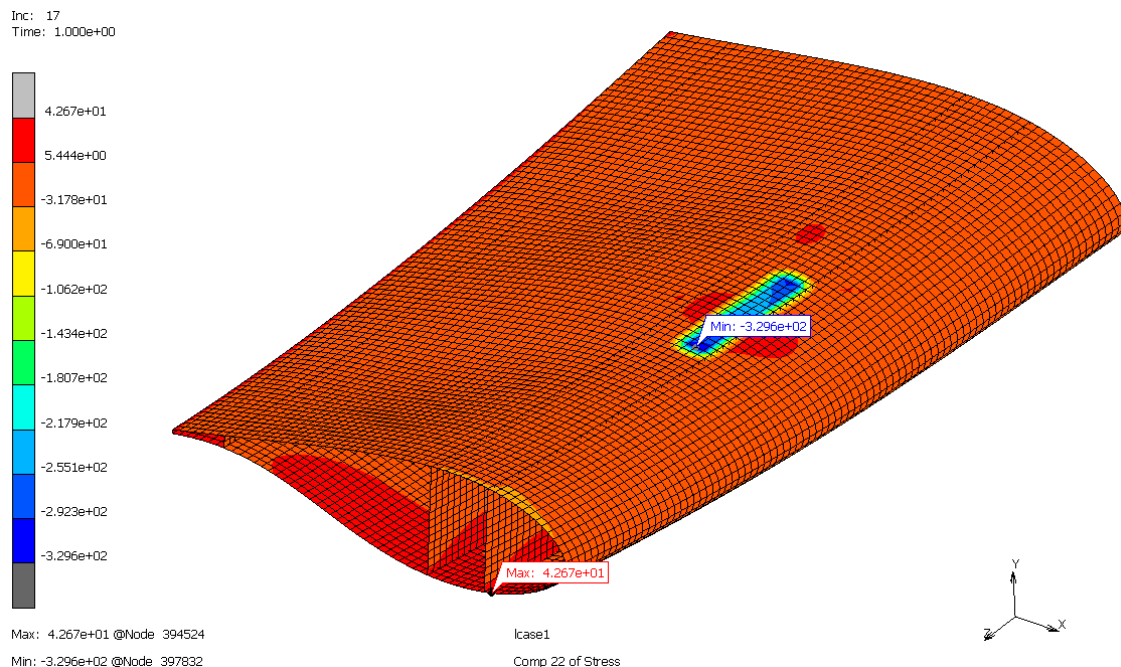


Figure 25. Compression and stress concentration along 2 directions of the fiber in the middle region of local buckling-induced delamination

The stress concentration at σ_{22} poses a potential risk for failure in the adhesive element. If the stress in σ_{22} surpasses the strength of the cohesion element, the cohesion element will fail,

separating the connected parts. Here are several methods to mitigate stress concentration in σ_{22} :

- Increase the thickness of the adhesive bonding
- Use a more resilient adhesive material
- Modify the adhesive bonding geometry to reduce stress concentration
- Add a fillet or chamfer to the edge of the adhesive joint to minimize stress concentration

3.5. Role of Total Strain Energy Density on DTU 10 MW Wind Turbine Blade

The node with the highest total strain energy density in the DTU 10MW wind turbine blade is identified as the crack initiation point, and crack formation is observed at this location (Figure 26).

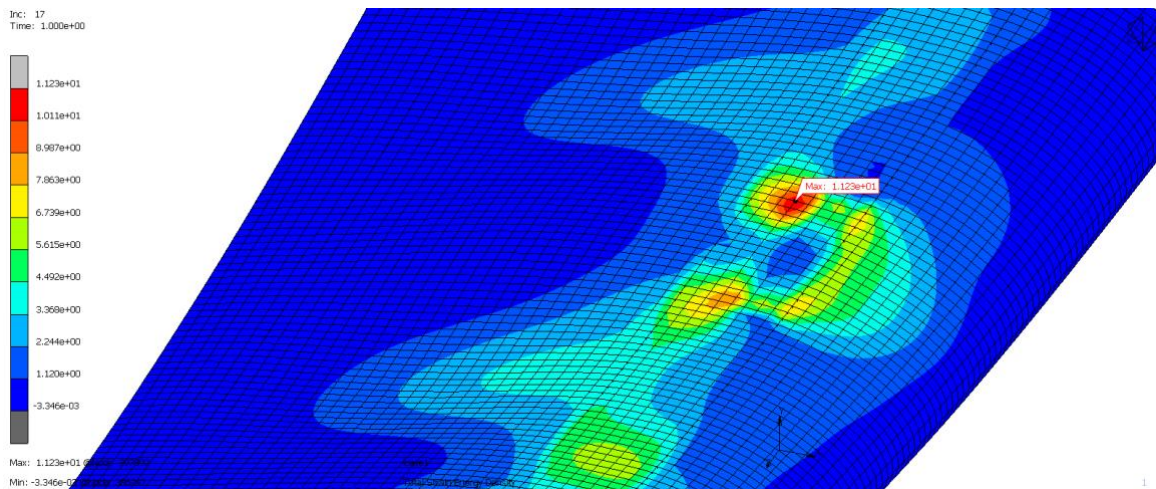


Figure 26. The node where the total strain energy density is maximum

The process of material failure involves crack initiation, growth, and coalescence, with stress concentrations occurring at the crack tip (Figure 27). The equivalent of von Mises stress at a crack is used to assess the impact of the crack on the material's durability. Fracture of the material may occur when the equivalent von Mises stress at the crack edges reaches a critical level. Once this critical value is reached, the crack significantly compromises the material's durability and poses a severe safety hazard.

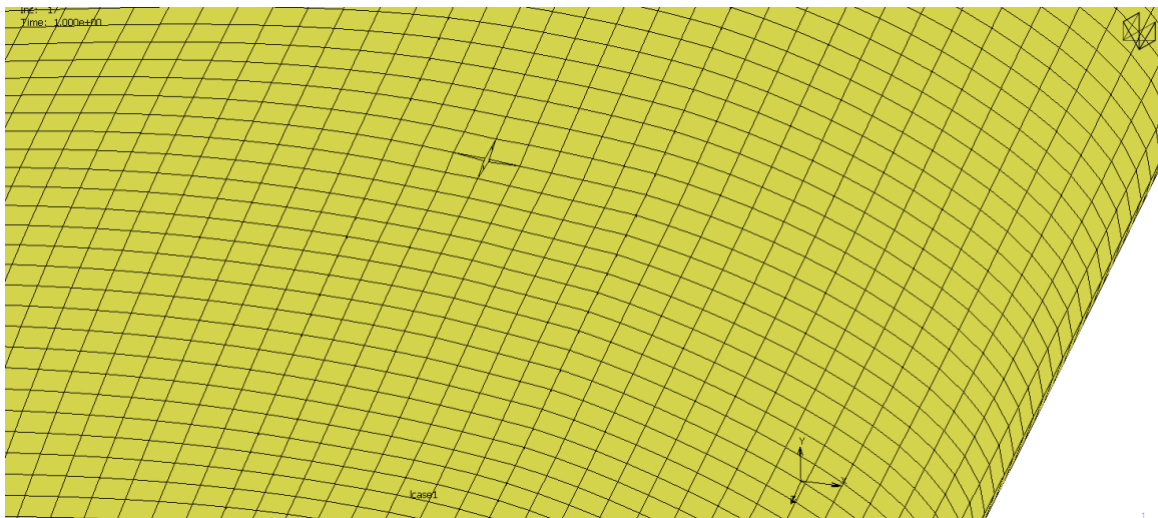


Figure 27. Crack formation at the selected node

The crack is located in the central part of the spar cap. The length and shape of the crack are crucial in determining the equivalent von Mises stress. A longer, sharper crack produces more concentrated stress at the edges, leading to a higher equivalent von Mises stress. Additionally, the stress at the crack edges diminishes significantly with distance from the crack, indicating that stress is concentrated at the edges but becomes more uniformly distributed further away from the edges (Figure 28).

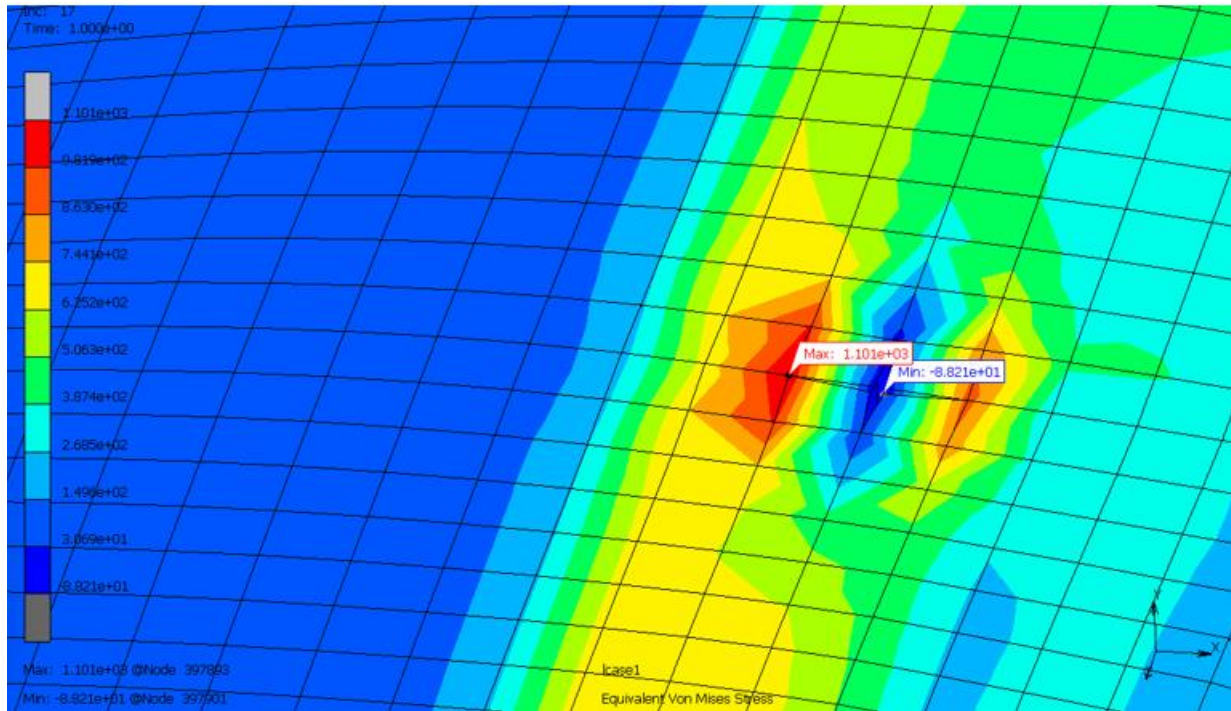


Figure 28. Equivalent von Mises stress in the crack

4. Conclusions

In this study, advanced methods from FEM simulation programs are applied within a specific scope to revisit and provide new insights into the study of Batmaz et al. (2021) and Haselbach (2015), which have made significant contributions to the literature. Extensive research has shown that turbine blades often experience failure, resulting in a significant loss of load-carrying capacity, especially when bending in the flapwise direction. The primary failure occurs in the transition zone near the root and is characterized by various failure modes caused by both in-plane and through-thickness stresses. A comprehensive analysis of the intricate failure features in the transition zone was conducted using finite element simulation with a global-local modeling approach. It was discovered that these failure features accumulate over the blade's loading history. Commonly observed failure modes included delamination of the spar cap on the suction side, separation of the sandwich surface-core bond, laminate fracture, and spar web rupture. Among these, spar cap delamination and spar web failure were identified as the primary causes of blade failure.

Wind-induced pressure generates material stresses σ_{11} and σ_{22} , which are the main contributors to the buckling of spar caps. Comparing these two stresses, it is evident that σ_{11} , with its high value at the delamination limit, is the primary cause of failure. Laminates with delamination defects exhibit local buckling and a combination of local and global buckling under heavy load. Local buckling in the delamination region, influenced by σ_{11} , subjects the fibers in the central area of the delamination to pressure along two directions, resulting in stress concentration. Consequently, stress concentration occurs at the delamination boundary,

dependent on σ_{11} , in the direction in which the laminate bends. The adhesive bonding region, being less stiff than the surrounding material, experiences stress concentration at its edge due to the difference in stiffness. Stress concentration at σ_{22} represents a potential failure zone for the adhesive element. If the stress at σ_{22} exceeds the strength of the cohesion element, the cohesion element will rupture, separating the connected parts. In this study, the following results were observed:

1. σ_{11} leads to buckling, particularly in defective laminates. Increasing compressive strength along the fiber slows down buckling-induced failure in laminates.
2. There is stress concentration in the middle of the delamination area due to σ_{11} and σ_{22} along the direction.
3. σ_{33} has minimal impact on the buckling failure of the structure.
4. Glue Breaking continues as a Touch contact when the adhesive contact effect is removed. Incorporating this feature obtained more accurate results.
5. Total strain energy density indicates how much energy the material consumes during plastic deformation. The fact that the von Mises stress maximum is slightly further away from the total strain energy density maximum may indicate that the material is softer and more ductile at the other end of the region. In this case, even though the material in the area has high von Mises stress, the total strain energy density will be low. As a result, the difference in the regions where von Mises stress and total strain energy density are concentrated may result from the difference in the material properties of the area, the applied load, or the form factor.
6. Crack formation is anticipated to occur predominantly in the region where the overall strain energy density is concentrated. Additionally, observations indicated the disappearance of the contact condition in both the area where adhesive separation was anticipated and the portion where laminate breakage was expected.
7. No visible cracks were detected, likely due to compressive forces. Tensile stresses typically lead to crack formation, whereas compressive stresses tend to prevent cracks from widening. The drop in ply along the material layout, attributed to the addition of the spar in this area, is the primary factor contributing to the separation failure observed here. Furthermore, it should be noted that delamination does not necessarily equate to "fracture." Instead, it is just one of the potential factors that can contribute to structural failure.

The rapid advancement of FEM programs clearly indicates that future studies building on this study will be highly beneficial for gaining a deeper understanding of failure mechanisms. Future studies could include the following: creating 3D models to analyze delamination more comprehensively or dividing the examined blade structure into sub-models for more specific analyses using newly developed FEM tools such as shell-to-shell, shell-to-solid, and solid-to-solid connection tools.

Author Statement

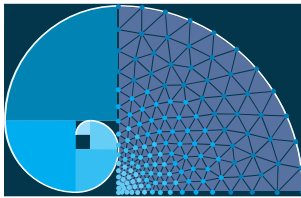
The authors confirm equal contribution to the paper.

Conflict of Interest

The authors declare no conflict of interest.

References

- Bak, C., Zahle, F., Bitsche, R., Kim, T., Yde, A., Henriksen, L. C., Hansen, M. H., Blasques, J. P. A. A., Gaunaa, M., & Natarajan, A. (2013). The DTU 10-MW Reference Wind Turbine. *In Danish Wind Power Research 2013 - Trinity, Fredericia, Denmark.*
- Batmaz, O. A., Muyan, C., & Çöker, D. (2019). Rüzgar Türbin Kanatlarında Yapıştırıcı Ayrılma Hasarının Kanat Yapısal Bütünlüğüne Etkisi. In 6. İzmir Rüzgâr Sempozyumu, 23-24 Eylül, 2021.
- Branner, K., & Berring, P. (2011). Compressive Strength of Thick Composite Panels. *In Risø National International Symposium on Material Science.*
- Castro, O., & Branner, K. (2021). Effect Of Tunneling Cracks on Structural Property Degradation of Wind Turbine Blades.
- Chen, X., Qi, Z., Yang, K., Zhao, X., & Xu, J. (2015). Numerical Analysis and Experimental Investigation of Wind Turbine Blades with Innovative Features: Structural Response and Characteristics. *Science China Technological Sciences.*
- Chen, X., Zhao, W., Zhao, X. L., & Xu, J. Z. (2014). Failure Test and Finite Element Simulation of a Large Wind Turbine Composite Blade Under Static Loading. *Energies.*
- Haselbach, P. U. (2015). The Ultimate Strength of Wind Turbine Blades Under Multiaxial Loading. *Technical University of Denmark.*
- Haselbach, P. U., & Branner, K. (2016). Initiation of Trailing Edge Failure in Full-Scale Wind Turbine Blade Test. *Engineering Fracture Mechanics.*
- Mankins, J. C. (2023). Technology Readiness Levels. In Marc, MSC. User's Guide, Volume A: *Theory and User Information* (MSC Software Corporation).
- Muyan, C., & Çöker, D. (2020). Strength Analysis of a 5-M Composite Wind Turbine Blade Under Static and Fatigue Loading Conditions. *In IOP Conference Series: Materials Science and Engineering.*
- Overgaard, L. C. T., & Lund, E. (2010). Structural Collapse of a Wind Turbine Blade. Part A: Static Test and Equivalent Single Layered Models. *Composites Part A*, 41.
- Yang, J., Peng, C., Xiao, J., Zeng, J., Xing, S., Jin, J., & Deng, H. (2012). Structural Investigation of Composite Wind Turbine Blade Considering Structural Collapse in Full-Scale Static Tests.



Isolation and Characterization of a (Surfactin-Like Molecule) Produced by *Bacillus subtilis*: Antagonistic Impact on Root-Knot Nematodes

Parwiz Niazi^{1*} 

Department of Biology, Faculty of Education, Kandahar University, Kandahar, Afghanistan

Department of Plant Protection, Faculty of Agriculture, Ege University, İzmir, Türkiye

*Corresponding author: parwiz60@gmail.com

Received: 05.04.2024

Accepted: 13.08.2024

Abstract

Plant-parasitic nematodes are severe soil-borne pathogens that cause significant damage to agricultural products each year, resulting in substantial financial losses globally. Thus, there is an urgent need to identify novel biological control agents or nematicides. The nematicidal potential of *Bacillus subtilis*-derived lipopeptides against *Meloidogyne incognita* was investigated at various concentrations (35 ppm, 25 ppm, 15 ppm, 5 ppm) under in vitro conditions. Egg hatching inhibition and mortality of second-stage juveniles (J2s) of *M. incognita* were analyzed after exposure for 6, 12, 24, 48, and 96 hours. Data showed that with the increase in concentration and exposure period, egg hatching inhibition and percent mortality increases. Maximum percent mortality of J2s was reported at 35ppm i.e., 45%, 55%, 67.75%, 77% and 85% at 6, 12, 24, 48 and 96 hrs, respectively. The maximum ovicidal activity was reported at 35ppm concentration, with 84.61% of eggs hatching inhibition on 96 hrs of the exposure period. The bacterial culture suspension of *Bacillus subtilis* and *Pseudomonas putida* at 1.2×10^8 cfu/ml, and the crude lipopeptide (35ppm) was also investigated as a biological control agent against *M. incognita* on tomato in a pot experiment under glasshouse condition. Combinational treatment of *P. putida* and *B. subtilis* culture, prior to inoculation of *M. incognita* on tomato plant caused a significant increase in plant growth attributes and in biochemical parameters over the inoculated control. In the same treatment, the maximum reduction in nematode population and root galling was recorded. However, in the crude lipopeptide experiment study, root dip and inoculation of crude lipopeptide in tomato after the introduction of *M. incognita* caused a major augment in all the parameters over the inoculated control. MALDI-TOF MS analysis of crude lipopeptide shows surfactin like molecules at m/z 1058 $[M+Na]^+$. It is concluded that crude lipopeptide or combinational treatment of *B. subtilis* and *P. putida* culture suspension can be employed as a biocontrol agent against *M. incognita* and may act as a source of a novel nematicidal agent of bacterial origin.

Keywords: Surfactin-like molecule, *Bacillus subtilis*, isolation, characterization, antagonistic impact

1. Introduction

The tomato (*Solanum lycopersicum* L.) holds a significant economic value and is widely cultivated. A rich source of micronutrients, such as minerals, vitamins, and antioxidants essential for human health, tomatoes are particularly abundant in lycopene – an antioxidant known for reducing the risk of cancer, cardiovascular disease, and cellular aging (Gerszberg et al., 2015). India, ranking third globally in tomato production after China and the USA, harvested 0.8 million hectares, with a yield of 26 thousand per hectare, resulting in a total production of 20.7 million tons in 2018 (Niemi and Väre, 2019). In many economically challenged nations, the impact of *Meloidogyne* spp. infection poses a severe challenge to maintaining an adequate tomato supply. Root-knot nematodes (RKN) are responsible for an estimated annual global loss of \$78 billion, affecting the vascular structure of plants and impeding water uptake, nutrient transport, and photosynthesis. Nematode secretions disrupt biochemical and molecular processes in plant roots, weakening their ability to absorb water and nutrients from the soil. Numerous experiments have explored methods to reduce nematode infection, including non-host crop rotation and the application of chemical nematicides like halogenated aliphatic hydrocarbons (e.g., 1,3-dichloropropene), a mixture of methyl isothiocyanate, oxamyl, thionazin, and carbofuran. However, the widespread use of these chemical nematicides poses ecological risks (Gowda et al., 2019). Khan et al. (2024) demonstrated that *Oxalis corniculata* effectively serves as an eco-friendly phyto-nematicide against the root-knot nematode (*Meloidogyne incognita*), significantly reducing nematode mortality, egg hatching, and improving cabbage growth and yield compared to other botanicals and untreated plants.

Given the current emphasis on eco-friendly disease control, recent research has focused on microbial-derived products (Naamala & Smith, 2021). Plant growth-promoting rhizobacteria (PGPR) offer an environmentally friendly approach to controlling plant diseases, when cultivated with PGPR, plants receive more precise protection from soil-borne illnesses, ensuring sufficient nutrient uptake and the release of phytohormones (Prasad et al., 2019). *Bacillus* spp. and *Pseudomonas* spp. have been studied as bio-nematicides due to their production of nematocidal secondary metabolites, antibacterial substances, enzymes, and exotoxins (Shaikh et al., 2016). *Bacillus subtilis*, in particular, has gained attention for its environmental safety. Fengycin, surfactin, and iturin, lipopeptides produced by this bacterium, have demonstrated potential in combating plant diseases. These lipopeptides, containing a lipophilic fatty acid chain and a hydrophilic peptide ring, act by creating pores in membranes, leading to an imbalance in transmembrane ion fluxes and eventual cell death (Earl et al., 2008). Dutta et al. (2019) reviewed the use of brassica and non-brassica biofumigant crops for plant-parasitic nematode suppression, highlighting their mechanisms and integrating this technique into broader nematode management practices. Recently, Walia and Khan (2023) provided a comprehensive overview of *Meloidogyne* species systematics, including their morphology, host and cytological races, impact on crops in India, and detailed management strategies for nematodes in vegetable cropping systems, emphasizing biological control, host resistance, chemical nematicides, and management in protected cultivation.

Nematodes also pose significant challenges to agriculture in numerous other countries, affecting a wide range of crops and contributing to substantial economic losses. Their impact extends globally, leading to reduced yields and increased management costs for

farmers. In response to these challenges, scientific research is actively being conducted across various nations to develop effective strategies for nematode control.

El-Nuby et al. (2019) conducted a survey of plant parasitic nematodes in the Sinai Peninsula, Egypt, finding 13 genera across 9 families and 3 orders, with *Meloidogyne* being the most abundant and dominant genus. They noted greater nematode diversity in North Sinai compared to South Sinai, where some genera were recorded for the first time. Elawady et al. (2022) surveyed nematodes in solanaceous plants in Dakahlia governorate, identifying 10 genera with *Meloidogyne* spp. as the predominant pest, especially in clayey soils, and highlighting variations in nematode incidence among different crops. Yahaya et al. (2024) identified ten genera of plant-parasitic nematodes in citrus rhizospheres in Ado and Gboko, Benue State, Nigeria, with *Tylenchulus* spp. being the most abundant and frequent, suggesting that local environmental conditions favor their growth. A survey (Ami et al., 2018) in Semel District revealed that root-knot disease incidence on cucumber plants peaked in autumn, with the highest infection rates in Sartenk and the lowest in Sharia, and identified *Meloidogyne javanica* as the prevalent nematode species, showing significant fluctuations in population density throughout the year. Kumar et al. (2014) surveyed nine Local Government Areas in Niger State, Nigeria, from April to September 2012, finding a 64.59% overall infection rate of root-gall disease across five vegetable crops, with the highest frequency in Lapai and the lowest in Mariga, and noted varying disease severity among the crops. Engelbrecht et al. (2020) reviewed the current nematode threats to soybean production and explored potential biological control options, emphasizing the need for comprehensive research to address global food demands, particularly in developing countries like those in sub-Saharan Africa. Lu et al. (2022) reported the first natural infection of *Brassica juncea* with *Meloidogyne graminicola* in southern China, identifying symptoms and confirming the nematode's pathogenicity, highlighting a new threat to mustard production in the region. Gürkan and Çetintaş (2024) identified root-knot nematode populations from vegetable fields in Kahramanmaraş, Türkiye, detecting *Meloidogyne incognita* and *Meloidogyne javanica* with specific races, including the first report of *M. javanica* in the region.

Although *Pseudomonas* spp. and *Bacillus* spp. are now utilized by bacterial lipopeptide manufacturers, their widespread adoption is hindered by expensive processing and recovery costs (Shafi et al., 2017). Scientists are actively developing new manufacturing techniques, such as novel media formulations, low-cost substrates, and production procedures. The increased isolation of active natural bio-products from bacterial interactions emphasizes the importance of finding natural antibiotics to combat phytopathogens. Consequently, bacterial-based surfactin has been employed to address root-knot disease caused by *Meloidogyne incognita* in tomatoes, aligning with the need for environmentally safe and agriculturally appropriate bio-products derived from bacterial interactions.

2. Methods and Material

2.1. Preparation and Sterilization of Soil

The dirt was cleaned before putting it in 8-inch clay pots. Each pot was filled with 4 kg of cleaned soil. The soil, a type commonly found, was collected from a fallow field at Farm. It was then sifted through a 16 mesh sieve to remove stones and debris. The soil

was mixed with Farmyard Manure in a 3:1 ratio, and the mixture was used to fill 25 cm diameter clay pots at 4 kg per pot. A small amount of water was added to slightly moisten the soil before sterilizing the pots in an autoclave at 20 lbs. pressure for 20 minutes. After sterilization, the pots were left to cool at room temperature before being used for experiments.

2.2. Collection of Root-knot Nematode

Surveys were conducted in the agricultural fields, roots of heavily infected vegetable crops, affected by root-knot nematodes, were collected by gently uprooting the plants. Soil particles clinging to the roots were removed. The infected roots were then placed in polythene bags and transported to the laboratory for further examination.

Upon reaching the laboratory, the infected root samples were washed with running tap water to check for the presence of egg masses on the root system. To remove attached soil, highly contaminated roots were gently shaken and soaked vigorously in water. Sterilized forceps were used to pick egg masses, and they were sprayed with clean distilled water after surface sterilization with 0.5% sodium hypochlorite (NaOCl). These treated egg masses were transferred to a Petri plate with sterilized water and incubated at 28 ± 2 °C.

Every 24 hours, newly hatched second-stage juveniles (J2) were collected, washed in fresh water, and the process was repeated daily. To determine the concentration of freshly hatched J2, an average of five counts were made, resulting in a suspension volume containing 200 J2 *M. incognita* per milliliter. For inoculation, 10 ml of this suspension (equivalent to 2000 freshly hatched *M. incognita* J2) was used.

2.3. Scanning Electron Microscopy (SEM) Analysis for Identification of RKN Species

Utilizing the female perineal pattern served as the methodology for RKN species identification. Extraction of females from root-knot galls was delicately executed, followed by their placement on a pristine glass slide immersed in lacto phenol. The posterior section of the female was intentionally sliced with precision using a thin razor blade, and subsequent washing of the body content ensued. Further perineal trimming was undertaken, and the prepared specimens were mounted for meticulous observation. To create a controlled observation environment, a circular coverslip (13 mm) was meticulously coated with a thick ring of glycerol. This formed a chamber containing approximately ten female patterns, positioned facing upwards in a droplet of 45% lactic acid. The coverslip, now housing the specimens, was affixed to a microscopic slide. To facilitate the removal of lactic acid, one drop of 2% formalin was systematically applied to the chamber every 2–3 minutes. After a 10-minute interval, the solution was absorbed onto filter paper, and the perineal pattern underwent desiccation in desiccators at room temperature (Al Banna et al., 2020).

Following this preparation, the coverslip was detached from the glass slide and affixed to the adhesive side of a scanning electron microscopy (SEM) stub. A gold coating (14-nm thick) was applied before subjecting the specimen to analysis in the SEM apparatus (JSM 6510LV; Jeol, Tokyo, Japan). The SEM image obtained from this process was subsequently employed to scrutinize the surface morphology of the perineal pattern, aiding in the differentiation of Meloidogyne species, as detailed in a referenced source.

2.4. Preparation of Bacterial Inoculum

Procurement of bacterial strains (*Bacillus subtilis* MTCC-441 and *Pseudomonas putida* MTCC-102) involved their acquisition from IMTECH (Chandigarh, India). Following this, the strains were inoculated onto a nutrient agar plate and subjected to incubation for either 24 or 48 hours at a temperature of 28 ± 2 °C. In the subsequent phase of inoculum preparation, both *B. subtilis* and *P. putida* were separately introduced into NB medium, comprising 3 g of beef extract, 5 g of peptone, and 10 g of glucose, dissolved in 1 liter of double-distilled water at a pH of 7.4 ± 0.2 . These bacterial cultures underwent incubation at 28°C for a duration of 48 hours. The calculation and adjustment of cell density were executed to reach a concentration of 1.2×10^8 colony-forming units per millilitre (CFU ml⁻¹).

2.5. Extraction of Crude Lipopeptide

Initiating the process, a bacterial colony of *Bacillus subtilis* found its place in Luria broth (50 mL) within a (250 mL) Erlenmeyer flask. Incubation unfolded at 28°C and 180 rpm, extending over 24 hours. The resultant 24-hour-old inoculum served as the foundation for seeding yeast extract peptone dextrose medium (YPD medium; composition in g/L: 1% yeast extract, 2% peptone, 2% glucose) in a 1000-mL flask. This seeding aimed for an initial OD-600 (Optical Density measured at a wavelength of 600 nm) of approximately 0.05. Subsequent incubation transpired at 28°C and 180 rpm, encompassing a duration of 72 hours.

The culmination of this incubation period marked the extraction of the 72-hour-old fermentation broth from both *B. subtilis* and *P. putida*. Centrifugation, executed at approximately 10,000 rpm and 4°C for 10 minutes, led to the separation of the supernatant. Adjustments were made to the pH, reducing it to 4 using concentrated HCL, followed by overnight incubation at 4°C to precipitate the lipopeptides. The acid precipitates underwent recovery through another round of centrifugation at approximately 10,000 rpm and 4°C for 10 minutes. Subsequently, the freeze-drying process commenced, resulting in a pellet that was solubilized in anhydrous methanol and subjected to two extraction cycles. The collected samples underwent detailed analysis through MALDI-TOF MS/MS and were subsequently employed in the experimental procedures.

2.6. Identification of Crude Lipopeptides by Matrix-assisted Laser Desorption Ionization Time-of-Flight Mass Spectroscopy (MALDI-TOF MS)

To unveil the characteristics of crude lipopeptides, a MALDI-TOF MS Workstation (Applied Biosystems, Foster City, CA, USA) was harnessed, featuring a 337 nm pulsed nitrogen laser. The testing process involved combining the sample with an equivalent quantity of a saturated solution of 2,5-dihydroxybenzoic acid (DHB: 5 mg in 1 ml 70% acetonitrile, 0.1% trifluoroacetic acid). Vortexing the suspensions ensured a homogeneous mixture. Subsequently, an aliquot of 1–2 µl was carefully dotted onto the MALDI plate and left to air-dry. For this meticulous analysis, positive ion detection and reflector mode operation were engaged. The experiment maintained a constant potential acceleration at 20 kV. The mass spectrum, spanning the 900–1,500 m/z range, was meticulously observed. Each sample underwent 400 laser shots per spectrum, with the uninoculated LB medium serving as the control. The comparative analysis involved

assessing the mass of the detected molecules against the previously measured monoisotopic mass, aligning with insights gleaned from published literature.

2.7. Characterization of Crude Lipopeptides with Fourier Transform Infrared Spectroscopy (FTIR)

Employing the FTIR method delved into unraveling the overarching chemical nature of the extracted crude lipopeptides. This sophisticated technique served to scrutinize the functional groups and chemical bonds inherent in the crude extract. The investigative tool of choice was the Shimadzu FTIR spectrophotometer (Model 8400S, Tokyo, Japan). Execution of the analysis involved subjecting a sub-sample weighing 1 mg to a meticulous process with 100 mg of KBr. To achieve translucent pellets, the amalgam underwent exposure to a physical pressure of 7500 kg for a brief 30-second duration. The ensuing IR spectra were computed utilizing a PerkinElmer Spectrum version 10.4, encompassing a range of 500–4000 cm^{-1} wave number. This comprehensive spectrum was meticulously examined to unravel the intricate chemical nature of the bio surfactant embedded in the extracted crude lipopeptides (Varadavenkatesan and Murty, 2013).

2.8. Mortality Test

To study the nematicidal activity of lipopeptide extracted from *B. subtilis* and *P. putida*, the larval suspension containing 100 freshly hatched out J2 of *M. incognita* were taken in 5 cm diameter Petri dishes. A standard solution of 35ppm of lipopeptide was made; 3.5mg of lyophilized lipopeptide of *B. subtilis* was mixed with 100 ml of DDW separately. Then filtered through Whatman,s No-1 filter paper and the obtained filtrate was termed as 35ppm solution and diluted to 25ppm, 15ppm and 5ppm by adding required amount of DDW. For mortality test, 2mL of water suspension containing 100 J2s of *M. incognita* and poured in Petri plates containing 2mL of different aqueous concentrations (35ppm, 25ppm, 25ppm and 5ppm) of lipopeptide extracted from the bacterial strain. Four replicates of each treatment were taken. The Petri plates were kept at 28°C, the cripple (dead) J2s were counted under the stereoscopic binocular microscope, after every 6, 16 and 26 hours of exposure period. The mean percentage of mortality was calculated. However in control, the Petri plates containing only DW and nematode suspension (J2).

2.9. Hatching Test

In vitro experiments were conducted using Petri plates with a diameter of 5 cm, each containing 2 ml of crude lipopeptides at concentrations of 35, 25, 15, and 5 ppm. A micro-sieve, featuring a 40 μm pore nylon mesh, was carefully inserted into every plate. To initiate the process, healthy egg masses of *M. incognita* were sourced from infected eggplant roots. These masses were then placed in an Eppendorf tube and subjected to maceration in 1 ml of 0.5% NaOCl to release the eggs.

A total of six hundred eggs were meticulously transferred onto each micro-sieve and submerged in the respective dilutions of the crude lipopeptides. To prevent the evaporation of the product, the plates were securely covered. Randomly positioned on a tray, the experiment was conducted at a constant temperature of 28 ± 1 °C for varying exposure periods. Distilled water-filled Petri plates served as the control group. The quantification of J2 emergence from the eggs was performed at specific intervals: 6, 12, 24, 48, and 96 hours. Each treatment was replicated four times and the entire experiment

was repeated thrice. The calculation of the percentage inhibition of egg hatching was determined as in Eq. (1):

$$\text{Hatching inhibition \%} = \frac{C_o - T_a}{C_o} \times 100 \quad (1)$$

where C_o is the number of juveniles hatched in control, T_a is the number of J2 hatched in each concentration of lipopeptide after 6, 12, 24, 48 and 96 h of exposure.

2.10. Pot Experiment Design

Conducting a dual set of pot experiments concurrently aimed to scrutinize the nematocidal efficacy of both bacterial suspension cultures and the extracted crude lipopeptides derived from *B. subtilis* (MTCC-441) and *P. putida* (MTCC-102) against *M. incognita*. These experiments unfolded within the controlled environment of a glasshouse. The experimental setup involved the transplantation of two-week-old tomato cv. 22 seedlings into clay pots with a diameter of 15 cm, each containing 1 kg of autoclaved soil blended with organic manure in a 3:1 ratio. A single tomato transplant was sown in each pot. To ensure robust experimental design, four replicates were established for each treatment and control. The pots in both experiments were meticulously arranged following a fully randomized design and subjected to routine irrigation procedures.

SET-1:

The inoculation process involved one-week-old seedlings, and it was executed by adding the necessary amount of inoculum through four small perforations strategically placed around each plant. Sequentially, each plant underwent inoculation with *M. incognita* (2000 J2) and bacterial culture, with a volume of 10 mL per treatment. The intervals between these inoculations were systematically set at 7-day intervals:

T1 = *M. incognita* (2000J2) $\xrightarrow{\text{after 1week}}$ *Bacillus subtilis* (10 mL)

T2 = *M. incognita* (2000J2) $\xrightarrow{\text{after 1week}}$ *Pseudomonas putida* (10 mL)

T 3 = *M. incognita* (2000J2) $\xrightarrow{\text{after 1week}}$ *Bacillus subtilis* + *Pseudomonas putida* (10 mL)

T 4 = *Bacillus subtilis* (10 mL) $\xrightarrow{\text{after 1week}}$ *M. incognita* (2000J2)

T 5 = *Pseudomonas putida* (10 mL) $\xrightarrow{\text{after 1week}}$ *M. incognita* (2000J2)

T 6 = *Bacillus subtilis* + *Pseudomonas putida* (10 mL) $\xrightarrow{\text{after 1week}}$ *M. incognita* (2000J2)

T 7 = Untreated Un-inoculated (control)

T 8 = Untreated Inoculated (nematode only)

UUC: untreated uninoculated control (control), UIC: untreated inoculated control (nematodes only).

SET-2:

One week old seedlings root dip into extracted lipopeptide of 35ppm concentration of *B. subtilis* and *P. putida* respectively for 5mins before transplanting. Afterwards each plant was inoculated with *M. incognita* (2000 J2) after an interval of 1 week.

F 1 = Root dip (*Bacillus subtilis* lipopeptide) $\xrightarrow{\text{after 1 week}}$ *M. incognita* (2000J2)

F 2 = Root dip (*Bacillus subtilis* lipopeptide) $\xrightarrow{\text{after 1 week}}$ *M. incognita* (2000J2) $\xrightarrow{\text{after 1 week}}$ 500 μ L *Bacillus subtilis* lipopeptide

F 3 = Untreated Un-inoculated (control)

F 4 = Untreated Inoculated (nematode only)

UUC: untreated uninoculated control (control), UIC: untreated inoculated control (nematodes only).

2.11. Data Collection and Observations

The experiments were concluded two months post-inoculation, prompting the evaluation of data encompassing growth, biochemical, and pathological parameters. The parameters scrutinized included total length, total fresh and dry weight, chlorophyll and carotenoid content, nitrate reductase activity (NRA), egg masses per root system, root gall index (RGI), and nematode population per 250 g of soil.

Roots underwent a 15-minute staining process in an aqueous solution of Phloxine *B stain* (0.15 g/L in water), followed by thorough washing under running tap water to eliminate residual stain. The determination of egg masses ensued. To assess the population of root-knot nematodes (RKN), Cobb's sieving and decanting technique were applied, followed by the modified Baermann's funnel technique (Chaudhary et al., 2011). Nematode suspension was obtained after 72 hours, and five aliquots of 1 ml from each sample were counted using a stereomicroscope to ascertain the nematode count. The mean of four counts was employed to calculate the nematode population per 250 g of soil.

For root gall evaluation, roots were meticulously washed under flowing tap water. Root galling was quantified using the root gall index (RGI), where 0 indicated no galling, 1 denoted 1–2 galls, 2 represented 3–10 galls, 3 encompassed 11–30 galls, 4 covered 30–100 galls, and 5 signified more than 100 galls (Monfort et al., 2007).

2.12. Biochemical Parameters

2.12.1. Chlorophyll estimation

The quantification of chlorophyll content in fresh leaves followed Mackinney's method (Ali et al., 2021). To begin, one gram of finely cut fresh leaves underwent a meticulous grinding process in a mortar and pestle, immersed in 20 ml of 80% acetone. Following this, the mixture underwent centrifugation at 5000 rpm for 5 minutes, leading to the collection of the supernatant in a 100 ml volumetric flask. The residue underwent three washes with 80% acetone, with each wash contributing to the same volumetric flask. The total volume was adjusted to the mark using 80% acetone. Subsequent to these steps, absorbance readings were taken at wavelengths of 645 nm and 663 nm against a blank (80% acetone) using a spectrophotometer (U 1700, Shimadzu, Japan). The calculation of chlorophyll content within the extract (mg per gram of tissue) was executed using the Eq. (2):

$$\text{Mg total chlorophyll g}^{-1} \text{ tissue} = \frac{20.2 (A_{645}) + 8.02 (A_{663})}{1000 \times W} \times V \quad (2)$$

2.12.2. Nitrate reductase activity (NRA)

To assess the nitrate reductase activity in fresh leaves, the method outlined was employed (Martinez & Cerda, 1989). The leaves were meticulously cut into small pieces measuring 1-2 cm. A precise weight of 200 mg of these chopped leaves was then transferred to plastic vials. Each vial received 2.5 ml of phosphate buffer (pH 7.5), along with 0.5 ml of potassium nitrate solution, followed by the addition of 2.5 ml of 5% isopropanol.

These vials were subjected to a 2-hour incubation in a BOD incubator at $30 \pm 2^\circ\text{C}$ in the absence of light. Post-incubation, a 0.4 ml aliquot from the mixture was withdrawn into a test tube, to which 0.3 ml each of sulfanilamide solution and NED-HCL were added. The test tubes were left undisturbed for 20 minutes to allow for optimal color development. The mixture was then diluted to 5 ml using Double Distilled Water (DDW). Subsequent absorbance readings (O.D.) were taken at 540 nm using a spectrophotometer. Simultaneously, a blank was run with each sample. For calibration purposes, a standard curve was generated utilizing known graded concentrations of NaNO_2 (Sodium nitrite) solution. The absorbance (O.D) of each sample was then compared with the calibration curve, and nitrate reductase activity was expressed in nm (umol per hour per gram).

2.12.3. Statistical analysis

The analysis of data was performed through the Duncan Multiple Range Test (DMRT) within the framework of a fully randomized block design, utilizing R (version 2.14.1; R Foundation for Statistical Computing, Vienna, Austria), (Duncan, 1955). To provide a measure of precision, the standard error of the mean ($\pm\text{SE}$) was computed, and the least significant difference (LSD) at a 5% significance level was also determined using R.

3. Results and Discussions

3.1. MALDI-TOF MS Analysis of the Lipopeptide Extracts of *Bacillus Subtilis*

Lipopeptide-producing *Bacillus subtilis* strain (MTCC 411) was grown under pre-established conditions in NA medium for 48 hours and their extracts obtained by ethyl acetate extraction followed by methanol extraction. The extracts were then subjected to MALDI-TOF MS analysis. The isolated dried residues were dissolved in methanol (BS100) and used for MALDI-TOF MS analysis separately. By observing spectrum, it can be seen that the detected peaks has mass in sample BS100, which is very similar to lipopeptide compound- surfactin C (m/z 1058 $[\text{M}+\text{Na}]^+$ and m/z 1074 $[\text{M}+\text{K}]^+$ in positive mode. The MALDI analysis showed that the sample also contained a small amount of other lipopeptides at m/z 966 and 3422.

3.2. Root-Knot Symptoms and Morphological Assessment

Manifestations of *M. incognita* above the ground were characterized by noticeable patches in the field and compromised plant growth, presenting a stunted appearance and chlorotic leaves (Tian et al., 2018). Meanwhile, belowground symptoms were evident through the emergence of swollen and hooked root tips in affected root systems. Upon dissecting the galled roots, it was discerned that both females and males were present.

The females, exhibiting a pear-shaped form, were embedded within the cortical layer of the root. Their bodies appeared translucent white, pyriform-shaped, and varied in size. The neck was prominent and short, bent at various angles, with smaller body annuli in the anterior neck region. The perineal pattern of the females took on an oval shape, featuring dorsal round arches, smooth striate, and distinct lateral lines. Notably, egg sacs were commonly found outside the root. Detailed observations of the perineal pattern of the female were captured through scanning electron micrographs.

3.3. Effect of Aqueous Concentration of Lipopeptide-surfactin Extracted from *Bacillus Subtilis* on The Juvenile Mortality of *Meloidogyne Incognita* in Vitro

The present experiment was conducted under in vitro conditions to evaluate the nematotoxic potential of the different concentration 35ppm, 25ppm, 15ppm and 5ppm of isolated lipopeptide-surfactin from *Bacillus subtilis*. The nematode juveniles were exposed for 6, 16 and 26 hours in different concentrations (Table 1). In aqueous concentration of 35ppm lipopeptide-surfactin, 63% nematode mortality was observed after 26 hours of exposure period, which is maximum amongst all the treatment. However, only 53%, 42.75% and 36.75% mortality were observed after 26 hours of exposure period in 25ppm, 15ppm and 5ppm of aqueous dilution respectively. After 16 hours of exposure period 35ppm of aqueous concentration results in mortality i.e. 56.25%, while only 43.50%, 33% and 22.50% nematode mortality was observed in 25ppm, 15ppm and 5ppm respectively. Similar pattern was observed in 6 hours of exposure period where 35ppm causes 48.79% mortality while 25ppm causes 34.75%, 15ppm 23.25% and 5ppm 13%. The distilled water control group exhibited no observed nematode mortality. Consequently, the results highlight the distinct toxicity of the isolated lipopeptide-surfactin at 35 ppm compared to other concentrations. As the aqueous concentration of lipopeptide-surfactin decreased, along with the exposure period, a corresponding decrease in nematode mortality was noted. Additionally, the mortality demonstrated a direct proportionality to the concentration of the lipopeptide-surfactin extracts. Notably, a linear relationship was discerned between the aqueous dilution strength of the concentration and the percentage mortality of the nematodes, reinforcing the significance of concentration in influencing the observed outcomes.

Table 1. Effect of aqueous lipopeptide (surfactin) extract of *Bacillus subtilis* on the juvenile mortality of *Meloidogyne incognita* in vitro

Treatment	Exposure Period (Hours)	Percent mortality (Mean \pm SE) in different aqueous concentrations (ppm)					Regression Equation
		DW	5	15	25	35	
Surfactin (<i>B. subtilis</i> LP)	6	0 (0.11)	13.00 \pm 1.29 ^d (12.03)	23.25 \pm 2.49 ^c (24.50)	34.75 \pm 2.62 ^b (35.87)	48.75 \pm 2.62 ^a (47.79)	y=23.95+11.92(X-2)
	16	0 (4.75)	22.50 \pm 2.10 ^d (17.70)	33.00 \pm 2.08 ^c (30.65)	43.50 \pm 2.50 ^b (43.60)	54.25 \pm 1.75 ^a (56.55)	y=30.65+12.95(X-2)
	26	0 (10.58)	36.75 \pm 1.37 ^d (24.84)	42.75 \pm 1.31 ^c (39.35)	53.00 \pm 1.58 ^b (53.36)	63.00 \pm 1.77 ^a (67.62)	y=39.35+14.26(X-2)

Each value is an average of four replicates, DW=Distilled water (control), SE= Standard error, ppm= Parts per million.

Values calculated from the regression Equation are given in parentheses.

Values are mean \pm standard error of four measurements with different superscript letters within groups are significantly different (p<0.05).

Lipopeptide (LP) surfactin significantly killed the infective juveniles (J2) of *Meloidogyne incognita* during treatment with different aqueous concentration (ppm) at 6 hours, 16 hours and 26 hours exposure period. Obtained data indicated that among the all treatments, more J2 of *M. incognita* were killed when treated with 35ppm of surfactin and was followed by 25ppm, 15ppm and 5ppm respectively.

3.4. Effect of Aqueous Concentration of Lipopeptide-surfactin Extracted from *Bacillus Subtilis* on The Juveniles Hatching at 7th Day on *Meloidogyne Incognita* in Vitro

The study was carried out under in vitro condition to test the nematostatic potential of lipopeptide-surfactin extracted from *Bacillus subtilis* with different aqueous concentration viz. 35ppm, 25ppm, 15ppm and 5ppm against the hatching of second stage juveniles (J2) of *M. incognita* after 7 days.

Result presented in Table 2, clearly showed that extracted lipopeptide-surfactin depicts gradual decrease in egg hatching from their lower concentration to higher concentration. This revealed that the high concentration (35ppm) of extract shows toxic effect on juvenile hatching. The results obtained from the experiment clearly reported that the maximum inhibition in hatching i.e., 86.93% was observed in 35ppm followed by 75.08% inhibition in 25ppm, 54.78% in 15ppm and minimum inhibition in 5ppm, only 27.56%. Maximum egg hatching was observed in control. Although among all the different aqueous concentrations maximum hatching was found in 5ppm of lipopeptide-surfactin extracts at 7 days exposure. The juvenile (J2) hatching was inversely proportional to the concentration of extracts (35ppm, 25ppm, 15ppm and 5ppm).

Table 2. Effect of aqueous lipopeptide (surfactin) extract of *Bacillus subtilis* on egg hatching of *Meloidogyne incognita* in vitro

Treatment	Exposure Period (days)	Number of juvenile hatched (Mean \pm SE) in different concentration (ppm)				
		DW	5	15	25	35
Surfactin (<i>B. subtilis</i> LP)	7	595a \pm 0.00 (0.00)	431.75b \pm 8.12 (27.56)	269.00c \pm 10.09 (54.78)	148.25d \pm 3.49 (75.08)	77.75e \pm 4.21 (86.93)

Each value is an average of four replicates, DW=Distilled water (control), SE= Standard error, ppm= Parts per million.

Value of percent inhibition in juvenile hatching over control are given in parenthesis.

Values are mean \pm standard error of four measurements with different superscript letters within groups are significantly different ($p < 0.05$).

Lipopeptide (LP) surfactin significantly affect the hatching of eggs of females of *Meloidogyne incognita* during treatment with different aqueous concentration (ppm) at 3 days, 5 days and 7 days of exposure period. Obtained data indicated that among the all treatments, least eggs of *M. Incognita* were hatched when treated with 35ppm of surfactin and was followed by 25ppm, 15ppm and 5ppm respectively.

3.5. Effect Of Bacterial Culture of *Bacillus Subtilis* and *Psuedomonas Putida* on Root-Knot Development Caused by *M. Incognita* and Plant Growth of *Lycopersicon Lycopersicum* L:

The experiment was conducted in pots to assess the effectiveness of bio-pesticides in autoclaved soil supplemented with manure, focusing on mitigating root-knot incidence

caused by *Meloidogyne incognita* and promoting the growth of tomato plants. In untreated, inoculated control pots, the root-knot nematode *M. incognita* exhibited high pathogenicity, reflected in a root-knot index (RKI) of 4.8 on a 0-5 scale.

Significant reduction in root-galling caused by *M. incognita* was observed in the T6 treatment, where a combination of 10 mL each of *Bacillus subtilis* and *Pseudomonas putida* bacterial culture was applied one week before the inoculation of J2 of *M. incognita*. In comparison to untreated, inoculated control plants, the root-knot index was notably lower at 1.2 in plants treated with T6 (refer to Table 3).

The plant length was observed highest in treatment T6 (*Bacillus subtilis* + *Pseudomonas putida* (10 mL) $\xrightarrow{\text{after 1 week}}$ *M. incognita* (2000J2) (85.2cm), followed by T4 (*Bacillus subtilis* (10 mL) $\xrightarrow{\text{after 1 week}}$ *M. incognita* (2000J2) with 77.1cm length, T5 (*Pseudomonas putida* (10 mL) $\xrightarrow{\text{after 1 week}}$ *M. incognita* (2000J2) with 67.2cm, T3 (*M. incognita* (2000J2) $\xrightarrow{\text{after 1 week}}$ *Bacillus subtilis* + *Pseudomonas putida* (10 mL) with 54.6cm, T1 (*M. incognita* (2000J2) $\xrightarrow{\text{after 1 week}}$ *Bacillus subtilis*(10 mL) with 49.0cm and lowest amongst the treatment in T2 *M. incognita* (2000J2) $\xrightarrow{\text{after 1 week}}$ *Pseudomonas putida* (10 mL) with 44.7cm total length only. The untreated inoculated control plants has total height of only 36.4cm compared to the untreated un-inoculated control plant with maximum height of 98.3 cm.

The total fresh weight was observed highest in treatment T6 (87.37g), followed by T4 (80.17g), T5 (73.75g), T3 (62.05g), T1 (55.32g) and lowest amongst the treatment in T2 with 44.22g total fresh weight only. The untreated inoculated control plants has total fresh weight of only 35.02g compared to the untreated un-inoculated control plant with total fresh weight of 100.22g.

Total dry weight was observed highest in treatment T6 (24.95g), followed by T4 (21.67g), T5 (18.15g), T3 (13.97g), T1 (12.10g) and lowest amongst the treatment in T2 (10.17g) total dry weight only, untreated inoculated control plants has total dry weight of only 6.35g compared to the untreated un-inoculated control plant with total fresh weight of 29.02g. The chlorophyll content was observed highest in treatment T6 (2.16mg/g), followed by T4 (1.89mg/g), T5 (1.76mg/g), T3 (1.54mg/g), T1 (1.39mg/g) and least amongst the treatment in T2 with 1.15mg/g total chlorophyll content. The untreated inoculated control plants has total chlorophyll content of only 1.04mg/g compared to the untreated un-inoculated control plant with total chlorophyll content of 2.53mg/g.

The carotenoid content was observed highest in treatment T6 (0.81mg/g), followed by T4 (0.65mg/g), T5 (0.50mg/g), T3 (0.36mg/g), T1 (0.33mg/g) and least amongst the treatment in T2 with 0.28mg/g carotenoids content. The untreated inoculated control plants has carotenoids content of only 0.20mg/g compared to the untreated un-inoculated control plant with carotenoids content of 0.96 mg/g. The nitrate reductase activity (NRA) was also observed highest in treatment T6 (0.415 $\mu\text{mh-1g-1}$), followed by T4 (0.362 $\mu\text{mh-1g-1}$), T5 (0.281 $\mu\text{mh-1g-1}$), T3 (0.242 $\mu\text{mh-1g-1}$), T1 (0.216 $\mu\text{mh-1g-1}$) and least amongst the treatment in T2 with 0.186 $\mu\text{mh-1g-1}$ nitrate reductase activity. The untreated inoculated control plants have NRA content of only 0.152 $\mu\text{mh-1g-1}$ compared to the untreated un-inoculated control plant with NRA content of 0.489 $\mu\text{mh-1g-1}$ (Table 4).

Table 3. (SET-1) Effect of bacterial culture (10mL) of *Bacillus subtilis* and *Psuedomonas putida* on the root-knot development caused by *Meloidogyne incognita* in relation to plant growth of tomato plants in pots

Parameters	Length(cm)		Total length (cm)	Fresh weight (g)		Total fresh weight (g)	Dry weight (gm)		Total dry weight (g)
	Shoot	Root		Shoot	Root		Shoot	Root	
T1	32.6ef ±1.4	16.3de ±0.8	49.9f±1.2	41.90f ±1.60	13.42de ±0.71	55.32f±1.44	9.37f ±0.26	2.72de ±0.21	12.10f±0.17
T2	30.0f ±0.9	14.7e ±0.6	44.7f±0.4	33.17g ±1.06	11.05ef ±0.66	44.22g±1.06	8.10g ±0.15	2.07ef ±0.22	10.17g±0.35
T3	35.7e ±1.1	18.9d ±1.4	54.6e±1.2	47.85e ±1.08	14.20cd ±0.64	62.05e±0.81	11.05e ±0.45	2.92d ±0.25	13.97e±0.35
T4	53.6c ±1.2	23.5bc ±1.1	77.1c±2.3	63.45c ±1.33	16.72c ±0.51	80.17c±1.73	17.62c ±0.65	4.05c ±0.22	21.67c±0.75
T5	47.4d ±1.3	19.7cd ±1.2	67.2d±1.2	58.47d ±0.81	15.27cd ±1.17	73.75d±0.91	14.65d ±0.55	3.50cd ±0.42	18.15d±0.54
T6	58.0b ±0.8	27.2b ±1.3	85.2b±0.5	67.35b ±0.58	20.02b ±1.19	87.37b±1.13	19.80b ±0.46	5.15b ±0.30	24.95b±0.47
UUC	63.8a ±1.4	34.4a ±2.5	98.3a±3.8	75.00a ±0.79	25.22a ±1.13	100.22a±1.11	22.52a ±0.28	6.50a ±0.25	29.02a±0.24
UIC	23.9g ±1.2	12.5e ±0.6	36.4g±1.6	25.22h ±1.82	9.80f ±0.88	35.025h±2.22	4.80h ±0.30	1.55f ±0.17	6.35h±0.29

Table 4. (SET-1) Effect of bacterial culture (10mL) of *Bacillus subtilis* and *Psuedomonas putida* on the root-knot development caused by *Meloidogyne incognita* in relation to biochemical and pathological parameters in pots

Parameters	Chlorophyll content (mg g-1)	Carotenoid content (mg g-1)	NRA (µmh-1g-1)	Nematode Population/ 250 g soil	Root-knot index (RKI)
T1	1.39f±0.00	0.33e±0.01	0.216e±0.005	1006bc±96.0	2.8b±0.15
T2	1.15g±0.02	0.28ef±0.00	0.186f±0.003	1123b±42.73	3.2b±0.17
T3	1.54e±0.01	0.36e±0.02	0.242e±0.007	976bc±53.48	2.2c±0.15
T4	1.89c±0.03	0.65c±0.06	0.362c±0.005	789d±42.09	1.7d±0.17
T5	1.76d±0.04	0.50d±0.03	0.281d±0.014	880cd±46.50	2.0cd±0.20
T6	2.16b±0.02	0.81b±0.03	0.415b±0.009	566e±46.86	1.2e±0.15
UUC	2.53a±0.04	0.96a±0.00	0.489a±0.003	0f±0	0f±0
UIC	1.04h±0.05	0.20f±0.00	0.152g±0.017	2865a±0	4.8a±0

3.6. Effect of Lipopeptide-surfactin (35ppm) from *Bacillus Subtilis* on Root-knot Development Caused by *Meloidogyne Incognita* and Plant Growth of *Lycopersicon Lycopersicum L*

The experiment, conducted in pots, aimed to assess the effectiveness of extracted lipopeptide-surfactin in autoclaved soil supplemented with manure. The focus was on mitigating the root-knot incidence caused by *Meloidogyne incognita* and promoting the growth of tomato plants. In untreated, inoculated control pots, the root-knot nematode *M. incognita* exhibited high pathogenicity, resulting in a root-knot index (RKI) of 4.8 on a 0-5 scale. There was a significant reduction in root-galling caused by *M. incognita* in treatments of F2, where at the time of transplantation, 1 week old seedling was root dip in 35ppm aqueous extract of *Bacillus subtilis* lipopeptide-surfactin for 5min, then after 1 week 2000J2 were inoculated and then again after 1 week of inoculation 500µL of 35ppm aqueous extract of *Bacillus subtilis* lipopeptide-surfactin were inoculated in the

rhizospheric region of roots. Compared to untreated inoculated control plants, the root-knot index was only 1.2 in plants treated with T6 (Table 5).

The plant length was observed highest in treatment F2 (Root dip *Bacillus subtilis* lipopeptide) $\xrightarrow{\text{after 1week}}$ *M. incognita* (2000J2) $\xrightarrow{\text{after 1week}}$ 500 μ L *Bacillus subtilis* lipopeptide) having 71.2cm of total length, followed by F1 (Root dip *Bacillus subtilis* lipopeptide) $\xrightarrow{\text{after 1week}}$ *M. incognita* (2000J2) with 55.6cm. The untreated inoculated control plants has total height of only 36.4cm compared to the untreated un-inoculated control plant with maximum height of 98.3 cm.

The total fresh weight was observed highest in treatment F2 (79.80g), followed by F1 (62.95g). The untreated inoculated control plants has total fresh weight of only 35.02g compared to the untreated un-inoculated control plant with total fresh weight of 100.22g (Table 5).

The total dry weight was observed highest in treatment F2 (23.02g), followed by F1 (14.80g). The untreated inoculated control plants has total dry weight of only 6.35g compared to the untreated un-inoculated control plant with total fresh weight of 29.02g (Table 5).

The chlorophyll content was observed highest in treatment F2 (2.02mg/g), followed by F1 (1.65mg/g). The untreated inoculated control plants has total chlorophyll content of only 1.04mg/g compared to the untreated un-inoculated control plant with total chlorophyll content of 2.53mg/g. The carotenoid content was observed highest in treatment F2 (0.79mg/g), followed by F1 (0.36 mg/g). The untreated inoculated control plants has carotenoids content of only 0.20mg/g compared to the untreated un-inoculated control plant with carotenoids content of 0.96 mg/g (Table 6). The nitrate reductase activity (NRA) was also observed highest in treatment F2 (0.391 μ mh-1g-1), followed by F1 (0.270 μ mh-1g-1. The untreated inoculated control plants has NRA content of only 0.152 μ mh-1g-1 compared to the untreated un-inoculated control plant with NRA content of 0.489 μ mh-1g-1 (Table 6).

Table 5. (SET 2) Effect of extracted lipopeptide (35ppm) from *Bacillus subtilis* on the root-knot development caused by *M. incognita* in relation to plant growth of tomato plants in pots

Parameters	Length(cm)		Total length (cm)	Fresh weight (g)		Total fresh weight (g)	Dry weight (gm)		Total dry weight (g)
	Shoot	Root		Shoot	Root		Shoot	Root	
F1	37.9c ± 1.1	17.7b ± 0.5	55.6c ± 1.5	48.10c ± 0.99	11.85c ± 0.61	62.95c ± 0.71	11.52c ± 0.63	3.27c ± 0.26	14.80c ± 0.53
F2	52.7b \pm 0.8	18.5b ± 0.8	71.2b ± 1.5	61.85b ± 1.32	17.95b ± 0.83	79.80b ± 0.75	18.55b ± 0.75	4.47b ± 0.29	23.02b ± 0.53
UUC	63.8a ± 1.4	34.4a ± 2.5	98.3a ± 3.8	75.00a ± 0.79	25.22a ± 1.13	100.22a ± 1.11	22.52a ± 0.28	6.50a ± 0.25	29.02a ± 0.24
UIC	23.9d \pm 1.2	12.5c ± 0.6	36.4d ± 1.6	25.22d ± 1.82	9.80d ± 0.88	35.025d ± 2.22	4.80d ± 0.30	1.55d ± 0.17	6.35d ± 0.29

Table 6. (SET-2) Effect of extracted lipopeptide (35ppm) from *Bacillus subtilis* on the root-knot development caused by *M. Incognita* in relation to biochemical and pathological parameters in pots

Parameter Treatment	Chlorophyll Content (mg g ⁻¹)	Carotenoid Content (mg g ⁻¹)	NRA ($\mu\text{mh-1g-1}$)	Nematode Population/250 g soil	Root Gall Index (RGI)
F1	1.65e±0.02	0.36d±0.02	0.270e±0.006	811b±40.25	2.0b±0.15
F2	2.02c±0.03	0.79b±0.00	0.391c±0.006	564c±35.13	1.4c±0.20
UUC	2.53a±0.04	0.96a±0.00	0.489a±0.003	0d±0	0d±0
UIC	1.04g±0.05	0.20e±0.00	0.152h±0.017	2865a±77.25	5a±0

3.7. Discussion of Results

Our MALDI-TOF MS analysis seems consistent with other studies (Earl et al., 2008) on lipopeptides from *Bacillus subtilis*. The detection of surfactin is well-documented and aligns with its known mass/charge ratios. The presence of other lipopeptides also suggests a complex mixture, which is expected given the diversity of lipopeptides produced by *Bacillus subtilis*.

The symptoms and nematode morphology that we described are typical for root-knot nematode infestations and are consistent with those documented in the literature, such as in Tian et al. (2018). Our detailed description supports standard diagnostic criteria for root-knot nematodes.

The results indicate a dose-dependent response to surfactin, consistent with known properties of lipopeptides where higher concentrations generally lead to greater nematode mortality. This finding supports the use of surfactin as an effective nematicide, aligning with other research (Khan et al., 2024) on lipopeptide efficacy against nematodes.

The pattern of inhibition with increasing concentration is consistent with expected outcomes for nematicidal compounds. High concentrations leading to more significant effects is a common trend observed in similar studies (Walia and Khan, 2023).

The effectiveness of *Bacillus subtilis* and *Pseudomonas putida* treatments in reducing nematode impact and promoting plant growth is well-supported by the literature (Varadavenkatesan and Murty, 2013; Shafi et al., 2017; Khan and Siddiqui, 2019). The observed improvements in plant growth and reduction in nematode damage with combined bacterial treatments reflect similar findings in other studies, underscoring the potential of biocontrol agents in managing nematode infestations.

The results confirm that surfactin can mitigate root-knot damage and enhance plant growth, aligning with its known biological activity. The improvement in plant health and reduction in nematode damage with surfactin treatment is consistent with its role as a nematicide and plant growth enhancer (Tian et al., 2018).

The results from our experiments align with established findings on the effects of lipopeptides and biocontrol agents against nematodes. The MALDI-TOF MS data confirm the presence of surfactin and other lipopeptides, while the biological assays demonstrate effective nematode control and plant growth promotion. These findings support the potential application of surfactin and bacterial cultures as part of integrated pest management strategies.

4. Conclusion

The present research was carried out to envisage the results of experiments performed under in vitro and glasshouse conditions to evaluate the effect of bacterial culture of *Bacillus subtilis* and *Psuedomonas putida* and lipopeptide-surfactin of *B. subtilis* against root-knot nematode, *M. incognita* in Tomato cv. 'S-22'. During in vitro studies, the aqueous extracts of different concentrations of lipopeptide-surfactin of *B. subtilis* were found to be toxic to root-knot nematode egg and juveniles. Aqueous dilution of 35ppm was found to be highly deleterious to the root-knot nematode, *M. incognita*. It was followed by 25ppm, 15ppm and 5ppm. These aqueous dilutions also inhibited the larval hatching of *M. incognita* and the inhibition in hatching was increased with an increase in concentration of the lipopeptide surfactin. Maximum inhibition in egg hatching was observed in 35ppm while 5ppm shows least toxicity. There was a direct relationship between mortality of root-knot nematode and the exposure period. The mortality increased with an increase in the concentration of the lipopeptide-surfactin and exposure period. Highest concentration (35ppm) resulted in to significantly highest mortality rate of *M. incognita* at 26 hours compare to distilled water control (DW). In green-house experiment most of the treatments were highly effective in reducing the population densities and reproduction potential of root-knot nematode and root disease caused by *M. incognita*. Treatment of combination of bacterial culture of *Bacillus subtilis* and *Psuedomonas putida* was found highly effective in reducing root-knot development caused by *M. incognita* on Tomato. Maximum inhibition in root-knot development was observed in the plants treated with combination of bacterial culture of *Bacillus subtilis* and *Psuedomonas putida* and lowest in the plants treated with *Psuedomonas putida* after nematode inoculation. As a result of declined in root-knot development the plant growth in terms of length (cm), fresh weight (g), dry weight (g), and chlorophyll content, carotenoid content, Nitrate reductase activity were increased. Our results indicated that *Bacillus subtilis* and *Psuedomonas putida* and lipopeptide-surfactin of *B. subtilis* might be a promising biocontrol option for an effective and environmentally friendly control of plant pathogenic agents. Thus, surfactin based lipopeptides could be defined as a novel potential products to explore for use as biocontrol agents against plant disease.

Conflict of Interest

The authors declare no conflict of interest.

References

- Al Banna, L. S., Salem, N. M., Jaleel, G. A., & Awwad, A. M. (2020). Green Synthesis of Sulfur Nanoparticles Using Rosmarinus Officinalis Leaves Extract and Nematicidal Activity Against Meloidogyne Javanica. *Chemistry International*, 6(3), 137-143.
- Ali, K. A., Noraldeen, S. S., & Yaseen, A. A. (2021). An Evaluation Study for Chlorophyll Estimation Techniques. *Sarhad Journal of Agriculture*, 37(4), 1458-1465.
- Ami, S. N., Ghaeib, S., & Shingaly, A. (2018). Disease Incidence, Identification, and Monthly Fluctuations in The Population Density of Root-knot Nematodes *Meloidogyne Javanica* on Cucumber Plants in Semel District, Duhok, Kurdistan Region, Iraq. *Acta Universitatis Sapientiae Agriculture and Environment*, 10, 52-65.

- Chaudhary, K. K., Brhane, D., Okube, H., Zaid, T., & Dagne, E. (2011). Distribution, Frequency of Occurrence and Population Density of Root Knot Nematode in Hamelmalo-Eritrea. *African Journal of Microbiology Research*, 5(31), 5656-5661.
- Duncan, D. B. (1955). Multiple Range and Multiple F Tests. *Biometrics*, 11(1), 1-42.
- Dutta, T. K., Khan, M. R., & Phani, V. (2019). Plant-parasitic Nematode Management via Biofumigation Using Brassica and Non-Brassica Plants: Current Status and Future Prospects. *Current Plant Biology*, 17, 17-32.
- Earl, A. M., Losick, R., & Kolter, R. (2008). Ecology and Genomics of *Bacillus Subtilis*. *Trends in microbiology*, 16(6), 269-275.
- Elawady, H. M., Gad, S. B., Elsherbiny, E. A., & El-Sherif, A. G. (2022). Frequency Occurrence and Population Density of Plant-Parasitic Nematodes Associated with Solanaceous Plantations Grown in Dakahlia Governorate. *Journal of Plant Protection and Pathology*, 13(6), 117-121.
- El-Nuby, A. S. M., Montasser, S. A., & El Khadrawy, I. A. (2019). Diversity of Plant Parasitic Nematodes Associated with Some Vegetables in Sinai Peninsula, Egypt. *Egyptian Journal of Desert Research*, 69(Special Issue), 77-100.
- Engelbrecht, G., Claassens, S., Mienie, C. M. S., & Fourie, H. (2020). South Africa: An Important Soybean Producer in Sub-Saharan Africa and The Quest for Managing Nematode Pests of The Crop. *Agriculture*, 10(6), 242.
- Gerszberg, A., Hnatuszko-Konka, K., Kowalczyk, T., & Kononowicz, A. K. (2015). Tomato (*Solanum lycopersicum* L.) in The Service of Biotechnology. *Plant Cell, Tissue and Organ Culture (PCTOC)*, 120, 881-902.
- Gowda, M. T., Rai, A. B., & Singh, B. (2019). Root Knot Nematodes Menace in Vegetable Crops and Their Management in India: A Review. *Vegetable Science*, 46(1-2), 1-16.
- Gürkan, T., & Çetintaş, R. (2024). Identification of Root-Knot Nematode Species and Races in Kahramanmaraş and Its Districts. *KSU Journal of Agriculture and Nature*, 27(1), 174-182.
- Khan, A., Haris, M., Hussain, T., Ahmad Khan, A., & Dawood, M. F. A. (2024). Botanicals as Phyto-Nematicides Against Root-Knot Disease Caused by The Root-Knot Nematode (*Meloidogyne Incognita*) via Promoting Growth, Yield, and Biochemical Performance of Cabbage Crop. *Journal of Soil Science and Plant Nutrition*. <https://doi.org/10.1007/s42729-024-01930-7>.
- Khan, M. R., & Siddiqui, Z. A. (2019). Potential of *Pseudomonas Putida*, *Bacillus Subtilis*, and Their Mixture on The Management of *Meloidogyne Incognita*, *Pectobacterium Betavascularum*, and *Rhizoctonia Solani* Disease Complex of Beetroot (*Beta Vulgaris* L.). *Egyptian Journal of Biological Pest Control*, 29, 73.
- Kumar, N., Adamu, M. A., Isah, K. M., & Lawal, A. F. (2014). A Survey of Vegetable Fields for Root-Gall Disease in Niger State, Nigeria. *Production Agriculture and Technology (PAT) Journal*, 10(1), 17-27.
- Lu, X. H., Solangi, G. S., Huang, J. L., Qin, L. P., & Liu, Z. M. (2022). First Report of Root-Knot Nematode, *Meloidogyne Graminicola* on *Brassica Juncea* in China. *Journal of Nematology*.

- Martinez, V., & Cerda, A. (1989). Nitrate Reductase Activity in Tomato and Cucumber Leaves as Influenced by NaCl and N Source. *Journal of plant nutrition*, 12(11), 1335-1350.
- Monfort, W. S., Csinos, A. S., Desaeger, J., Seebold, K., Webster, T. M., & Diaz-Perez, J. C. (2007). Evaluating Brassica Species as an Alternative Control Measure for Root-Knot Nematode (*M. Incognita*) in Georgia Vegetable Plasticulture. *Crop Protection*, 26(9), 1359-1368.
- Naamala, J., & Smith, D. L. (2021). Microbial Derived Compounds, a Step toward Enhancing Microbial Inoculants Technology for Sustainable Agriculture. *Frontiers in Microbiology*, 12, 634807.
- Niemi, J., & Väre, M. (2019). Agriculture and Food Sector in Finland 2019.
- Prasad, M., Srinivasan, R., Chaudhary, M., Choudhary, M., & Jat, L. K. (2019). Plant Growth Promoting Rhizobacteria (PGPR) for Sustainable Agriculture: Perspectives and Challenges. *PGPR Amelioration in Sustainable Agriculture*, 129-157.
- Shafi, J., Tian, H., & Ji, M. (2017). Bacillus Species as Versatile Weapons for Plant Pathogens: A Review. *Biotechnology & Biotechnological Equipment*, 31(3), 446-459.
- Shaikh, S. S., Sayyed, R. Z., & Reddy, M. S. (2016). Plant Growth-Promoting Rhizobacteria: An Eco-Friendly Approach for Sustainable Agroecosystem. *Plant, Soil and Microbes: Implications in Crop Science*, 1, 181-201.
- Tian, Z. L., Maria, M., Barsalote, E. M., Castillo, P., & Zheng, J. W. (2018). Morphological and Molecular Characterization of The Rice Root-Knot Nematode, *Meloidogyne Graminicola*, Golden and Birchfeild, 1965 Occurring in Zhejiang, China. *Journal of Integrative Agriculture*, 17(12), 2724-2733.
- Varadavenkatesan, T., & Murty, V. R. (2013). Production of a Lipopeptide Biosurfactant by a Novel Bacillus Sp. and Its Applicability to Enhanced Oil Recovery. *International Scholarly Research Notices*.
- Walia, R. K., & Khan, M. R. (2023). Root-knot Nematodes (*Meloidogyne* Spp.). In F. Ahmad & G. N. Blázquez (Eds.), *Root-galling Disease of Vegetable Plants* 1-60. Springer.
- Yahaya, A. M., Charles, O., Peter, P., & Oche, E. C. (2024). Identification of Plant-Parasitic Nematodes Associated with *Citrus Sinensis* L. Osebeck (Sweet Orange) in Benue State, Nigeria. *Journal of Biological Research & Biotechnology*, 22(2), 2352-2361.